

THESIS

INVESTIGATION INTO A DISPLACEMENT BIAS IN NUMERICAL WEATHER
PREDICTION MODELS' FORECASTS OF MESOSCALE CONVECTIVE SYSTEMS

Submitted by

Charles Yost

Department of Atmospheric Science

In partial fulfillment of the requirements

For the Degree of Master of Science

Colorado State University

Fort Collins, Colorado

Spring 2013

Master's Committee:

Advisor: Russ Schumacher

Sue van den Heever

Jorge Ramirez

Copyright by Charles Marc Yost 2013

All Rights Reserved

ABSTRACT

INVESTIGATION INTO A DISPLACEMENT BIAS IN NUMERICAL WEATHER PREDICTION MODELS' FORECASTS OF MESOSCALE CONVECTIVE SYSTEMS

Although often hard to correctly forecast, mesoscale convective systems (MCSs) are responsible for a majority of warm-season, localized extreme rain events. This study investigates displacement errors often observed by forecasters and researchers in the Global Forecast System (GFS) and the North American Mesoscale (NAM) models, in addition to the European Centre for Medium Range Weather Forecasts (ECMWF) and the 4-km convection allowing NSSL-WRF models. Using archived radar data and Stage IV precipitation data from April to August of 2009 to 2011, MCSs were recorded and sorted into unique six-hour intervals. The locations of these MCSs were compared to the associated predicted precipitation field in all models using the Method for Object-Based Diagnostic Evaluation (MODE) tool, produced by the Developmental Testbed Center and verified through manual analysis.

A northward bias exists in the location of the forecasts in all lead times of the GFS, NAM, and ECMWF models. The MODE tool found that 74%, 68%, and 65% of the forecasts were too far to the north of the observed rainfall in the GFS, NAM and ECMWF models respectively. The higher-resolution NSSL-WRF model produced a near neutral location forecast error with 52% of the cases too far to the south. The GFS model consistently moved the MCSs too quickly with 65% of the cases located to the east of the observed MCS. The mean forecast displacement error from the GFS and NAM were on average 266 km and 249 km, respectively, while the ECMWF and NSSL-WRF produced a much lower average of 179 km and 158 km.

A case study of the Dubuque, IA MCS on 28 July 2011 was analyzed to identify the root cause of this bias. This MCS shattered several rainfall records and required over 50 people to be rescued from mobile home parks from around the area. This devastating MCS, which was a classic Training Line/Adjoining Stratiform archetype, had numerous northward-biased forecasts from all models, which are examined here. As common with this archetype, the MCS was triggered by the low-level jet impinging on a stationary front, with the heaviest precipitation totals in this case centered along the tri-state area of Iowa, Illinois, and Wisconsin. Low-level boundaries were objectively analyzed, using the gradient of equivalent potential temperature, for all forecasts and the NAM analysis. In the six forecasts that forecasted precipitation too far to the north, the predicted stationary front was located too far to the north of the observed front, and therefore convection was predicted to initiate too far to the north. Forecasts associated with a northern bias had a stationary front that was too far to the north, and neutral forecasts' frontal locations were closer to the observed location.

ACKNOWLEDGEMENTS

This research was supported by the National Science Foundation grant AGS-1157425 and COMET grants #Z10-83387 and #Z12-93241.

GFS and NAM model data was provided by the National Climatic Data Center (NCDC), with the ECM model data supplied by The Observing System Research and Predictability Experiment (THORPEX) Interactive Grand Global Ensemble (TIGGE). The high resolution NSSL-WRF model data was kindly supplied by Jack Kain of the National Severe Storms Laboratory. The Stage IV observed precipitation data was provided by the Environmental Modeling Center (EMC). The MODE tool is developed by the Developmental Testbed Center (DTC). Archived surface analyses were obtained from the Hydrometeorological Prediction Center (HPC), with all rain gauge and rainfall records supplied by the Quad Cities Weather Forecast Office.

I would like to personally thank my advisor, Dr. Russ Schumacher, for all of the tireless work and continued support to help me reach this point in my career. His belief in me has enabled me to get to where I am today. I would also like to thank my committee for agreeing to review my work and offer valuable insights. Thank you to the members of my research group - Sammy Lynch, Vanessa Vincente, John Peters, and Kelly Keene – for their help, encouragement, and friendship that steadied me on this journey.

And finally, a special thanks to my family and friends, especially my parents. This research and all of my life endeavors would not be possible without their unwavering support and love for me. They truly are the rock this life has been built on.

TABLE OF CONTENTS

Abstract	ii
Acknowledgements	iv
1 Introduction	1
2 Background	3
2.1 Heavy Rainfall and Flash Floods.....	3
2.2 Heavy Precipitation and Storm Motion	4
2.3 Linear Mesoscale Convective Systems	6
2.4 Extreme-Rain-Producing MCSs	7
2.5 Verification Techniques.....	9
2.6 Method for Object-Based Diagnostic Evaluation Tool	10
2.7 Similar Studies.....	13
3 Data and Methods	15
3.1 Selection of Cases.....	15
3.2 Observed Data Set	15
3.3 Operational and High Resolution Models	17
3.4 Temporal Dimension	18
3.5 MODE Tool.....	19
3.6 Selection of Matching Forecasts and Calculation of Displacement Error	21
3.7 Manual Verification	23
4 Forecast Location Results	24
4.1 North American Mesoscale Model	24
4.2 Global Forecast System Model	28
4.3 European Center for Medium Range Prediction Model	33
4.4 National Severe Storms Laboratory Weather Research and Forecasting Model	37
4.5 NSSL-WRF Subset	40
4.6 Regional Forecast Locations	46
4.7 Model Upgrades	48
4.8 Manual Verification Results	51
5 Case Study of the 27-28 July 2011 Dubuque, IA Mesoscale Convective System	54
5.1 Background.....	54
5.2 Pre-Event Environmental Setup	55
5.3 Primary Rain Event	62
5.4 Evaluation of the Models' Forecasts	64
5.5 Frontal Placement	73
6 Conclusions and Future Work	80
6.1 Conclusions	80
6.2 Future Work	82
References	83

LIST OF FIGURES

2.1.1 Monthly distribution of flash flood events by Maddox et al. (1979)	4
2.2.1 Diagram showing the near cancellation of cell motion and propagation from Doswell et al. (1996)	5
2.2.2 How convective systems with different motions affect the rainfall rate (R)	5
2.3.1 Schematic reflectivity drawing of idealized life cycles of linear MCSs	6
2.4.1 Schematic diagram of the radar-observed features of the TL/AS pattern	7
2.4.2 Schematic diagram of the radar-observed features of the BB pattern	8
2.6.1 Schematic example of various forecast and observation combinations	11
2.6.2 The process for resolving objects in the MODE tool	12
2.7.1 The two-dimensional, frequency distribution of stage IV observations	14
3.1 The observed 6-hour MCS locations from 2009 to 2011	16
3.2 The process for resolving objects in the MODE tool	18
3.5 Example of MODE output of oriented objects	20
3.7 Manual analysis example	23
4.1.1 NAM MCS forecast locations for all forecast times for all years.....	24
4.1.2 NAM MCS forecast locations for forecast 1-3 for all years	25
4.1.3 NAM MCS forecast locations for forecast 4-6 for all years	26
4.2.1 GFS MCS forecast locations for all forecast times for all years.....	29
4.2.2 GFS MCS forecast locations for forecast 1-3 for all years	30
4.2.3 GFS MCS forecast locations for forecast 4-6 for all years	31
4.3.1 ECM MCS forecast locations for all forecast times for all years	34
4.3.2 ECM MCS forecast locations for forecast 1-3 for all years.....	35
4.3.3 ECM MCS forecast locations for forecast 4-6 for all years.....	36
4.4.1 NSSL-WRF model’s MCS forecast locations for forecast 1-2.....	43
4.5.1 NSSL-WRF model’s MCS forecast locations compared to the NAM model’s MCS forecast locations.....	44
4.5.2 NSSL-WRF model’s MCS forecast locations compared to the NAM model’s MCS forecast locations	45
4.5.3 NSSL-WRF model’s MCS forecast locations compared to the NAM model’s MCS forecast locations.....	44
4.6.1 GFS model’s regional bias analysis	47
4.6.2 NAM model’s regional bias analysis	47
4.6.3 ECM model’s regional bias analysis.....	48
4.7.1 ECM model’s displacement errors before and after the major model upgrade	49
4.7.2 GFS model’s displacement errors before and after the major model upgrade	50
4.8.1 GFS model’s displacement errors from the manual analysis compared to the MODE tool analysis.....	52
4.8.2 NAM model’s displacement errors from the manual analysis compared to the MODE tool analysis	53
5.1.1 Stage IV 24-hour precipitation ending on 28 July 2011 at 18 UTC	54
5.1.2 Hydrograph of the Mississippi River at Dubuque, IA	55
5.2.1 NEXRAD 1 KM Mosaic for 27 July 2011 at 1 UTC	57

5.2.2	HPC surface analysis for 9 UTC on 27 July 2011.....	57
5.2.3	NEXRRAD 1 KM Mosaic for 27 July 2011 at 11 UTC.....	58
5.2.4	NAM analysis at 1200 UTC on 27 July 2011 of winds in knots at 850 hPa.....	58
5.2.5	NAM analysis at 1200 UTC on 27 July 2011 of potential temperature (Kelvin) and winds in knots at 850 hPa.....	59
5.2.6	Upper-air sounding from Topeka, KS at 1200 UTC on 27 July 2011.....	59
5.2.7	HPC surface analysis for 00 UTC on 28 July 2011.....	60
5.2.8	HPC surface analysis for 6 UTC on 28 July 2011.....	60
5.2.9	NAM analysis at 1800 UTC on 27 July 2011 of winds in knots at 850 hPa.....	61
5.2.10	NAM analysis at 0000 UTC on 28 July 2011 of potential temperature (Kelvin) and winds (knots) at 850 hPa.....	61
5.2.11	Upper-air sounding from Davenport, IA at 0000 UTC on 28 July 2011.....	62
5.3.1	Radar from Davenport, IA at 0244 UTC on 28 July 2011.....	63
5.3.2	Radar from Davenport, IA at 0421 UTC on 28 July 2011.....	63
5.3.3	Radar from Davenport, IA at 0826 UTC on 28 July 2011.....	64
5.4.1	The NAM model's 6 forecasts and corresponding Stage IV precipitation valid for 28 July 2011 0000 to 0600 UTC	65
5.4.2	The NAM model's 6 forecasts and corresponding Stage IV precipitation valid for 28 July 2011 0600 to 1200 UTC	66
5.4.3	NAM model's MCS forecast using the MODE tool for the two 6 hour periods on 28 July 2011 from 0000 to 1200 UTC	67
5.4.4	The GFS model's 6 forecasts and corresponding Stage IV precipitation valid for 28 July 2011 0000 to 0600 UTC	68
5.4.5	The GFS model's 6 forecasts and corresponding Stage IV precipitation valid for 28 July 2011 0600 to 1200 UTC	69
5.4.6	GFS model's MCS forecast using the MODE tool for the two 6 hour periods on 28 July 2011 from 0000 to 1200 UTC	70
5.4.7	The ECM model's 6 forecasts and corresponding Stage IV precipitation valid for 28 July 2011 0000 to 0600 UTC	71
5.4.8	The ECM model's 6 forecasts and corresponding Stage IV precipitation valid for 28 July 2011 0600 to 1200 UTC	72
5.4.9	ECM model's MCS forecast using the MODE tool for the two 6 hour periods on 28 July 2011 from 0000 to 1200 UTC	73
5.5.1	The objectively analyzed NAM analysis frontal locations	75
5.5.2	The objectively analyzed NAM analysis frontal location and the NAM model's 30 hour frontal location	75
5.5.3	The objectively analyzed NAM analysis frontal location and the NAM model's 6 hour frontal location	76
5.5.4	The potential temperature (Kelvin) and wind difference (knots) between the analysis and 30 hour forecast	78
5.5.5	The potential temperature (Kelvin) and wind difference (knots) between the analysis and 6 hour forecast	78
5.5.6	The magnitude of the wind difference (knots) between the analysis and 30 hour forecast	79
5.5.7	The magnitude of the wind difference (knots) between the analysis and 6 hour forecast	79

CHAPTER 1

INTRODUCTION

The operational and research communities have known about a possible northern bias associated with the location of extreme-rain producing MCSs in numerical weather prediction (NWP) models' forecasts. In their area forecast discussion (AFD) a few days before a particularly devastating MCS in 2011, forecasters at the Quad Cities Weather Forecast Office in Davenport, IA noted (NWS 2011):

THE MODELS WILL LIKELY BE PLAYING CATCH UP AND WILL PROBABLY
BE TOO FAR NORTH WITH FEATURES.

Forecasting the location of these MCSs is extremely difficult because the precipitation maximum is commonly a “bulls-eye” that increases in intensity inward and is longer than it is wide. A lateral shift north or south in a forecast leads to not forecasting any rain in the area that the extreme rain occurs, which can prove deadly given these mostly occur at night, and forecasting a false alarm in the area with the forecast for heavy rain, which can lead to adverse reactions for future forecasted extreme-rain events by the public. With shorter lead times, the operational models generally are able to resolve that there will be an extreme-rain event with the correct area, shape and intensity, but the location is normally incorrect. Forecasters then have the challenge of trusting models for the intensity and timing of the event, yet have to trust other clues for the location of the event. The use and desire of this uncertainty guidance by forecasters to assess uncertainty is noted in Novak et al. (2008) but cites these biases as one of the barriers for using this data. This study will investigate a possible bias associated with MCS locations in numerical weather prediction models, and if present, diagnose the degree and reasons for such a bias. A case study of an extreme-rain producing MCS will be presented and diagnosed for this possible bias, looking at possible causes of this bias.

The problem with evaluating forecasts for these extreme-rain events with traditional verification metrics is the forecast is essentially penalized twice with this bias, and thus evaluated as an poor forecast. Just as in forecasting these events for the public, the NWP model's forecast is penalized for not predicting any rain in the location of the observed, and forecasting too much to the north. Although given a low verification score using traditional metrics, these forecasts could still be considered a good forecast with the caveat of the location being inaccurate, making it valuable to forecasters. To circumvent this problem, a relatively new approach to forecast verification will be used to assess this bias. The forecasted and observed precipitation maxima will be objectively analyzed into objects, and forecast locations will be evaluated using the locations of these objects.

Using this method, the NWP model's forecasts will be evaluated for all linear MCSs that produced large amounts of precipitation during the warm seasons of 2009 – 2011. This investigation will cover temporal scales, high resolution, model upgrades, and regional biases, with the results verified against a manual analysis. The following case study will be performed on one of the cases from the list of cases above.

An MCS in Dubuque, IA on 27-28 July 2011 produced an immense amount of rain over a 12 hour period that caused massive amounts of flooding. Over fifty people had to be rescued from their homes with the majority of the rain occurring over-night hours. Although well forecasted for the most part by the operational models, several forecasts showed this same northern bias. This case study will examine the pre-event environmental setup, evaluate the forecasts on the location of their MCS, and investigate the cause for the northern forecasts.

CHAPTER 2

BACKGROUND

2.1 Heavy Rainfall and Flash Floods

Doswell et al. (1996) breaks down the necessary ingredients for extreme rainfall, that in order for large precipitation accumulations to occur, high rainfall rates must be sustained over an extended period of time. The total precipitation produced, P , is simply:

$$P = \bar{R}D \quad (2.1)$$

where \bar{R} is the average rainfall rate and D is the duration of the rainfall (Eqn. 2.1). The instantaneous rainfall rate, R , depends on q the mixing ratio of rising air, w the ascent rate, and E the precipitation efficiency:

$$R = Ewq \quad (2.2)$$

while the duration of the heaviest precipitation depends on the size and speed of the system, along with “within-system variations in rainfall intensity,” meaning that the largest and slowest moving systems have the longest duration (Doswell et al. 1996).

Maddox et al. (1979) performed a 5-year climatology of flash flood events, starting in 1973, which found that 52 of the 151 events (34%) were associated with a mesohigh at the surface. These flash flood events occurred throughout the year, but 86% of the sample occurred during the warm season months of April through September (Fig. 2.1.1). Also, 25% of the events were associated with a stationary or slow moving synoptic scale frontal boundary and thunderstorms developing on the cool side of the boundary.

MCSs can account for 30-70% of the total warm season precipitation in the central part of the United States according to Fritsch et al. (1986). This statistic combined with the domination of mesohigh and frontal events in the flash flood climatology by Maddox et al.

(1979) indicate that this storm type is important for not only warm season precipitation, but also extreme precipitation as well.

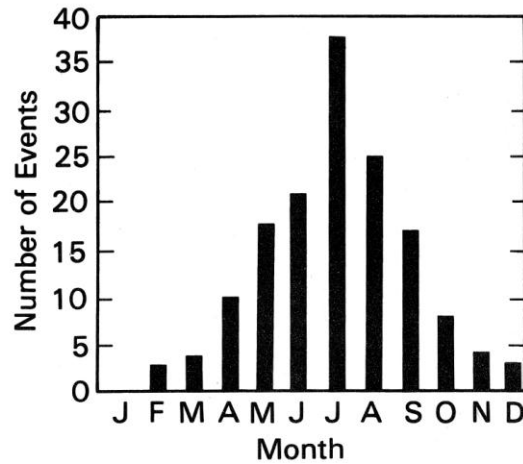


Fig. 2.1.1: Monthly distribution of flash flood events by Maddox et al. (1979)

2.2 Heavy Precipitation Producing Storm Motion

As previously noted, the heaviest rainfall from a precipitation system occurs when either the rainfall duration is long or the average rainfall rate is high, or both. The duration of the rainfall is influenced by storm motion, which Chappell (1986) describes as the addition of the two vectors: the individual velocities of the convective cells and the propagation velocity, resulting from the formation of new cells. The system motion is the slowest when these two vectors are equal and opposite, which causes the storm motion to cancel to near zero (Fig. 2.2.1). Figure 2.2.2 shows the different influences storm motion and type of convective system have on rainfall rate from Doswell et al. (1996). Fig. 2.2.2a shows a convective line with motion normal to that line, which does not produce long lasting precipitation at any point. The same line with storm motion mostly parallel to the line takes longer to pass the same point, which amounts to higher rainfall amounts. Schematics c) and d) from the same plot show the inclusion of stratiform rain's impact. MCSs with stratiform rain produce a moderate to heavy precipitation for a longer

duration following the passage of the convective band (Fig. 2.2.2c). With motion almost parallel to the line, convective cells pass in succession over any particular point, resulting in the “training effect” that produces greater rainfall (Fig. 2.2.2d).

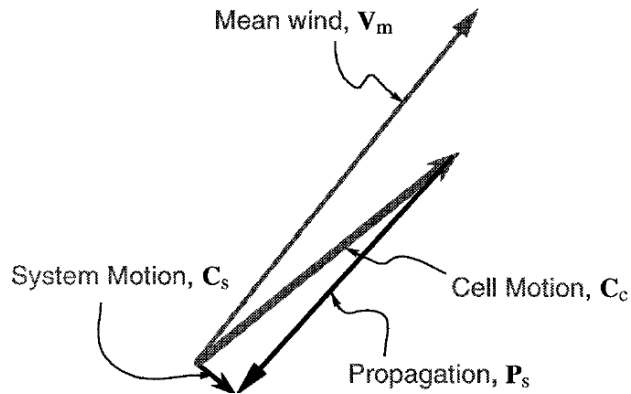


Fig. 2.2.1: Diagram showing the near cancellation of cell motion and propagation from Doswell et al. (1996)

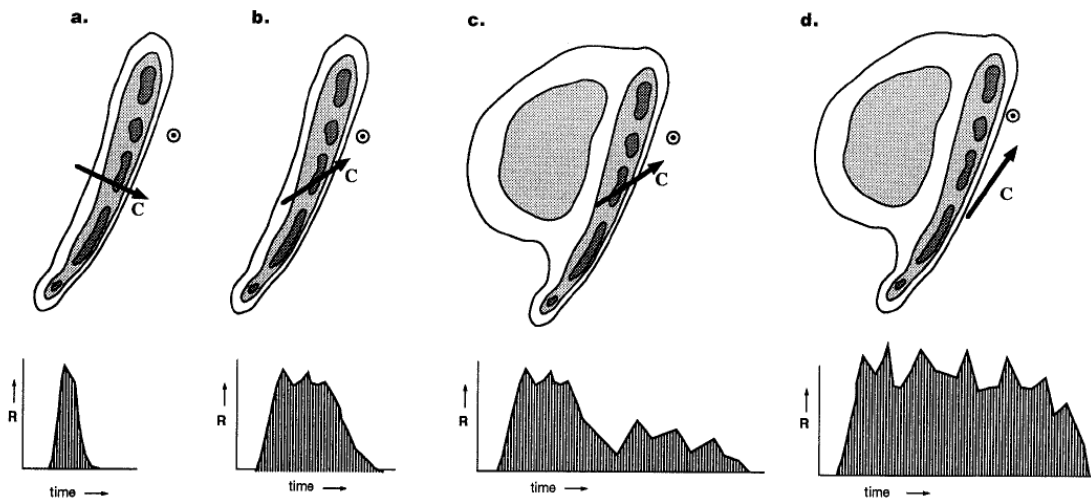


Fig. 2.2.2: Schematic showing how different types of convective systems with different motions affect the rainfall rate (R) at a point (indicated by a circled dot) as a function of time; contours and shading indicate radar reflectivity. For case (a) a convective line is passing the point with a motion nearly normal to the line, for case (b) the line is moving past the point with a large

component tangent to the line itself, for case (c) the line has a trailing region of moderate precipitation but is otherwise similar to (b), and for case (d) the motion of the line has only a small component normal to the line but is otherwise similar to (c). Total rainfall experienced at the point is the shaded area under the R vs time graphs. From Doswell et al. (1996)

2.3 Linear Mesoscale Convective Systems

Houze et al. (1990) in their study of mesoscale organization of rain events found that a linear MCSs organization is more likely to produce flash flooding than non-linear ones in Oklahoma. Parker and Johnson (2000) investigated common modes of MCSs by noting the radar structure of 88 linear MCSs from May 1996 to May 1997. They proposed three types of linear MCSs: trailing stratiform (TS), leading stratiform (LS), and parallel stratiform (PS) (Fig.

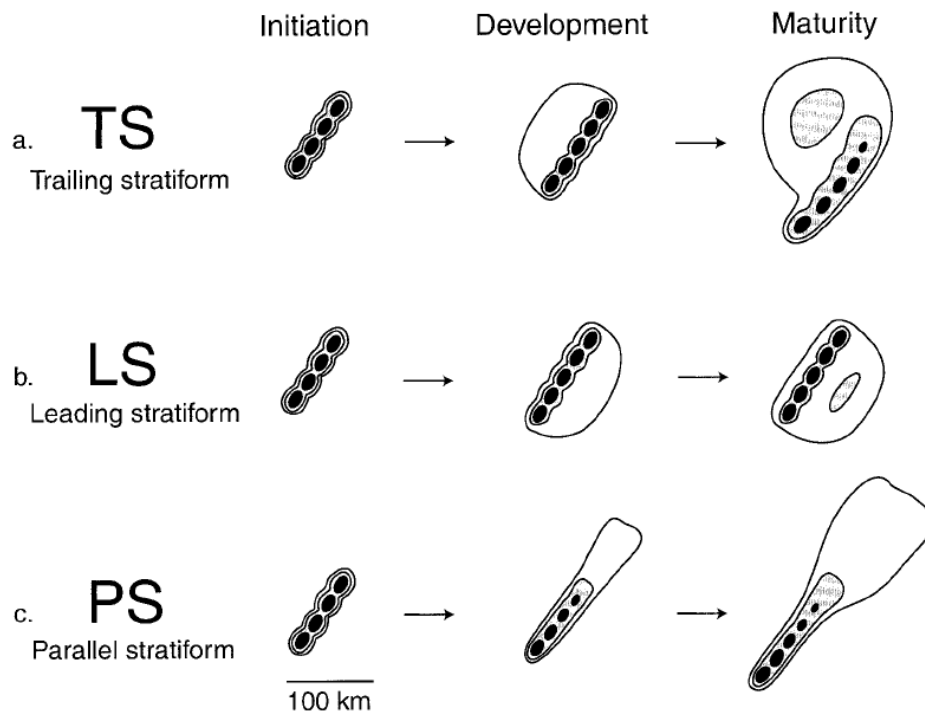


Fig. 2.3.1: Schematic reflectivity drawing of idealized life cycles for three MCS archetypes: (a) TS, (b) LS, and (c) PS with levels of shading roughly corresponding to 20, 40, and 50 dBZ. From Parker and Johnson (2000)

2.3.1). The trailing stratiform archetype is the most common with nearly 60% of the 88 cases resembling this structure. The trailing stratiform MCS type had strong front-to-rear relative winds throughout the cloud depth. The LS type was associated with weak middle and upper tropospheric rear-to-front storm-relative winds. The PS type has strong significant middle and upper tropospheric line-parallel storm-relative winds. While the LS MCS type lasted about half as long as the TS type, it moved more slowly, making it most likely of the 3 types to produce high local precipitation values.

2.4 Extreme-Rain-Producing MCSs

Schumacher and Johnson (2005) investigated the radar indicated structure of 76 extreme-rain-producing MCSs from 1999 to 2001 in the area east of the Rocky Mountains and found that 51.3% of the cases could be classified into two organizational structures. The most common of

A) TRAINING LINE -- ADJOINING STRATIFORM (TL/AS)

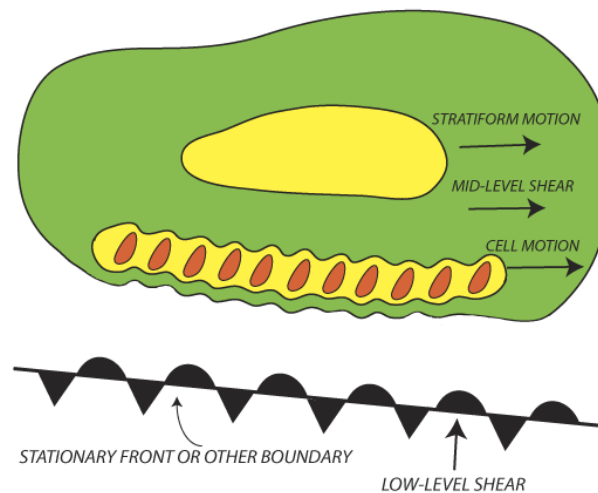


Fig. 2.4.1: Schematic diagram of the radar-observed features of the TL/AS pattern of extreme-rain-producing MCSs. Contour and shading represent approximate radar reflectivity values of 20, 40, and 50 dBZ. The low-level and mid-level shear arrows refer to the shear in the surface-to 925-hPa and 925–500-hPa layers. From Schumacher and Johnson (2005).

the two (31.6%) was the training line and adjoining stratiform type (TL/AS), which is a linear MCS with cell motion parallel to the convective line (Fig. 2.4.1). Over 70% of the TL/AS MCSs occur on the cool side of a warm front or stationary front. Air with high equivalent potential temperature is lifted over the boundary (making it elevated in nature) with the center of new convection coinciding with maximum instability and low-level convergence. Veering winds exist at low-levels with a unidirectional profile aloft, which is parallel to the convective line from 925-500 hPa. Finally, the presence of a wind speed maximum exists to the south of the rainfall center indicates a low-level jet.

The second type is the back-building or quasi-stationary type (BB), when convective cells repeatedly form upstream of older cells producing an area of unmoving high reflectivity on radar (Fig. 2.4.2). While this type is smaller in spatial extent than the TL/AS type, the potential for producing higher rainfall totals at a point is greater. While the environment for the BB types is less delineated, the overall setup is similar to the TL/AS type with weaker winds and smaller-

B) BACKBUILDING / QUASI-STATIONARY (BB)

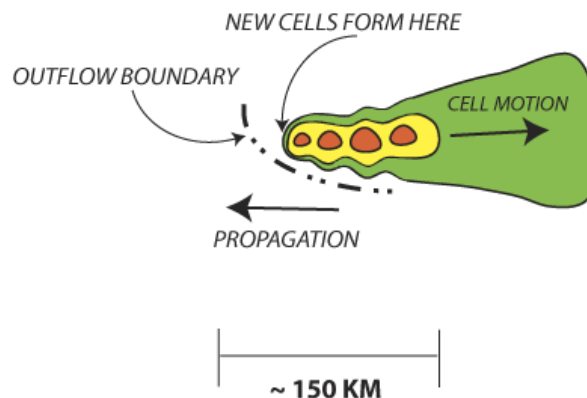


Fig. 2.4.2: Schematic diagram of the radar-observed features of the BB pattern of extreme-rain-producing MCSs. Contour and shading represent approximate radar reflectivity values of 20, 40, and 50 dBZ. The dash-dot line in (b) represents an outflow boundary; such boundaries were observed in many of the BB MCS cases.

scale surface features. No consistent correlation was found between the direction of the wind shear and the orientation of the BB type, but later work emphasized the importance of a reversal of the wind shear vector with height (e.g., Schumacher and Johnson 2008, 2009).

2.5 Verification Techniques

Traditional metrics for forecast verification include the critical success index (CSI) with its false alarm rate (FAR) and probability of detection (POD), the equitable threat score (ETS), the bias score, and the Brier skill score (BSS). The CSI has been around over a century in various forms to verify numerous weather phenomena, and was put summarized by Schaefer (1990) for the evaluation of warning skill. Schaefer states that for a set of forecasts with only yes or no alternatives, only four statements exists (which can be defined into a contingency table):

- (1) number of positive forecasts that correspond to an occurrence of an event.
- (2) number of negative forecasts that occurred with an event.
- (3) number of positive forecasts that were not accompanied by an event.
- (4) number of negative forecasts that did not have an associated event.

The number of events is simply the summation of statements 1 and 2, while the total number of cases is the summation of all statements. The probability of detection (POD) is the ratio of events that are correctly forecasted to occur to the total number of events, $POD = (1)/[(1) + (2)]$. The false alarm ratio (FAR) is the measure of the forecast or forecaster to not include non-event cases, which can be defined as the ratio of unsuccessful positive forecasts to total positive forecasts or $FAR = (3)/[(1) + (3)]$.

The ETS is a formula put forth by Gilbert (1884) and designed to objectively verify forecasts of precipitation while penalizing overforecasting events (Rogers et al. 1996). The ETS can be defined as

$$ETS = \frac{H - CH}{F + O - H - CH},$$

where F is the number of forecast points above a threshold, O is the number of observed points above a threshold, H is the number of correctly forecasted points above a threshold, and CH is the expected number of hits in a random forecast of F points for O observed points, which is equal to

$$CH = \frac{F \times O}{NUM},$$

where NUM is the number of points in the verification domain (Rogers et al. 1996). The BSS and BIAS are used to evaluate probability forecasts and wet/dry forecasts, respectively.

Since the publication of this CSI to verify forecasts and forecasters, a large number of new approaches for verification have been put forth to account for the new sources of data to verify against, more meaningful verification results, new modeling techniques, and higher spatial and temporal scales (Casati et al. 2008).

2.6 Method for Object-Based Diagnostic Evaluation Tool

Traditional metrics, such as the ETS, POD, FAR, and CSI, use an overlay of the observed to the forecasted grids in which a 2 x 2 contingency table is computed from the counts of the yes-no pairs (Doswell et al. 1990), and previously noted. These measures of verifications don't offer any specific information on where or how the forecast underperformed. Davis et al. (2006a) show in Figure 2.6.1 five scenarios where these traditional metrics fall short. Subjectively for a

forecast user, case (a) appears to be the best forecast with just a slight displacement to the right. Cases (b) and (d) have similar forecasts to the observed with just a further displacement right and an opposite shape, respectively. Case (c) has the completely wrong shape, as does case (e). Cases (a)-(d) are all objectively verified as poor forecasts ($CSI=0$, $FAR=1$, $POD=0$), while case (e) is verified as having value (POD , $CSI>0$, $FAR<1$), even though many people would consider case (a) to be the best forecast. Davis et al. (2006a) present an object based verification process that “addresses the skill of forecasts of localized episodic phenomena such as rainfall better than traditional measures-oriented approaches.” Figure 2.6.2 summarizes the steps put forth by Davis

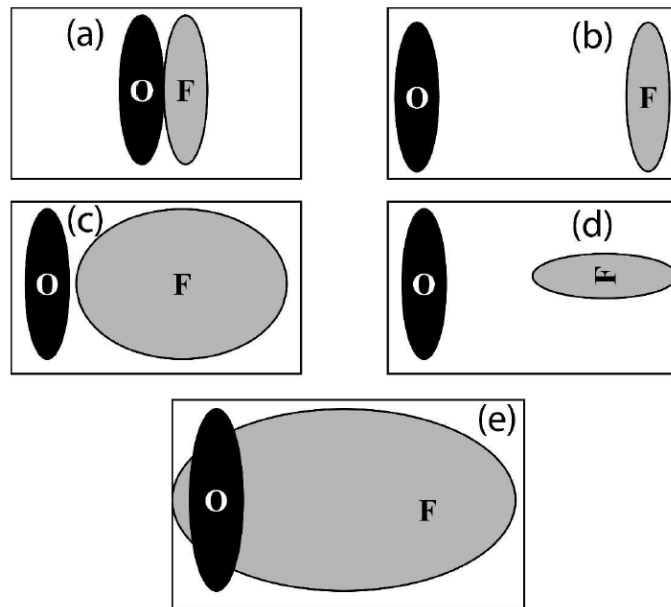


Fig. 2.6.1: A schematic example of various forecast and observation combinations. (a)–(d) These all yield $CSI = 0$, whereas (e) has positive CSI , but would probably not be evaluated as the best subjectively. From Davis et al. (2006a)

et al. (2006a), which include inputting the raw data, convolving the data, masking only certain values, and outputting the objects. The convolve step can be considered a smoothing step, which replaces the value at each point with the mean of the surrounding points inside of a user-

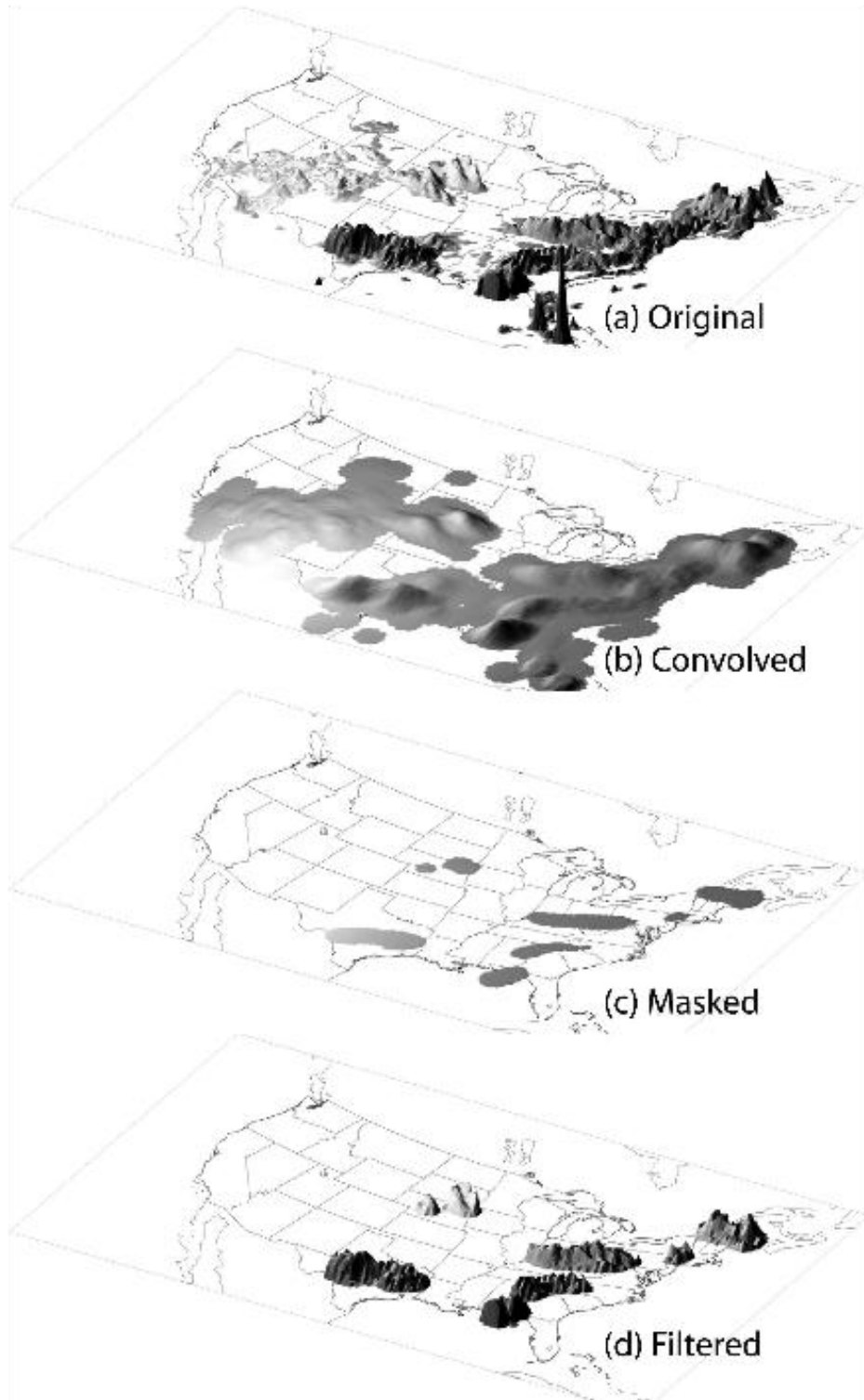


Figure 2.6.2: The process for resolving objects in the MODE tool, which includes (a) taking the original data, (b) convolving the data, (c) masking only certain values, and (d) returning the raw values. From Davis et al. (2006)

specified disk. A threshold is applied to the convolved field to provide the boundaries of the objects. The user again inputs the desired threshold depending on the application with higher thresholds used for greater size and intensity rain areas and lower thresholds for weaker and more isolated events. Finally, this mask is placed over the raw precipitation field in order to still be able to calculate statistics for each “patch.”

2.7 Similar Studies

The most recent study that compares forecasted precipitation relative to the observed is Marsh et al. (2012) that proposes a method for quantifying the uncertainty of forecasts of rare events from convection-allowing models. Their algorithm fits a “parametric kernel density function to the model’s historical spatial error characteristics.” Figure 2.7.1 shows the two-dimensional, frequency distribution of the observations relative to the NSSL-WRF forecasts, essentially showing the probability that the observation will occur in the corresponding grid point relative to the forecasted grid point. This figure shows that the observed rainfall more frequently fell to the north, or that the NSSL-WRF forecasted slightly to the south.

Wang and Clark (2010) also studied 64 quasi-stationary fronts and the NAM’s forecast for these fronts by using a composite technique. They found that while the overall synoptic features are well-represented, the NAM over predicted certain values, such as low-level wind and CAPE. Deformation and horizontal convergence, which are important for frontogenesis, are also overpredicted.

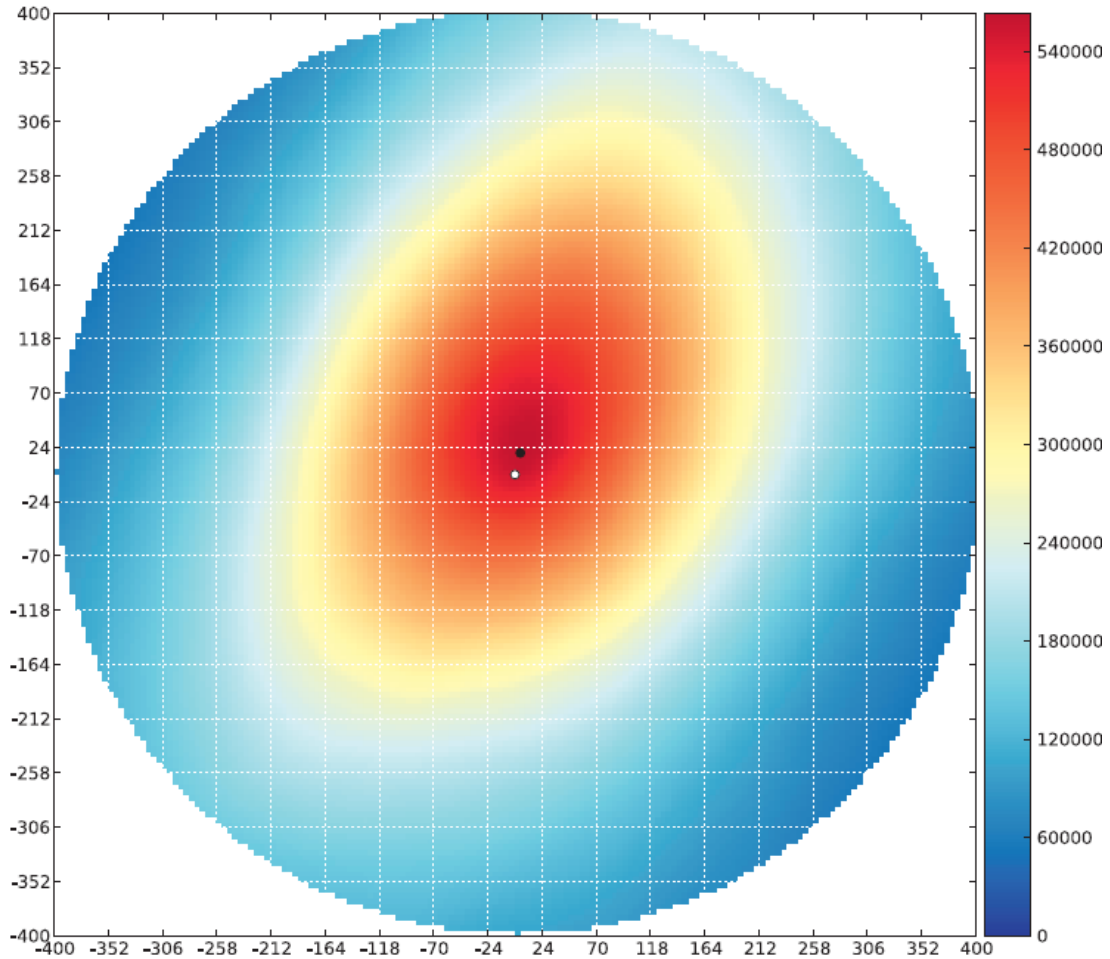


Figure 2.7.1: The two-dimensional, frequency distribution of stage IV observations . 25.4 mm relative to NSSLWRF forecasts of the same events for the training dataset (1 Apr 2007–31 Mar2010). The representative NSSLWRF forecast grid point is marked by a white dot in the middle of the domain and the stage IV observation frequency is color filled. To illustrate the displacement between forecasts and observations, the center of the fitted two-dimensional, anisotropic Gaussian is denoted by the black dot. From Marsh et al. (2012)

CHAPTER 3

DATA AND METHODS

3.1 Selection of Cases

Composite radar reflectivity mosaics from the National Center for Atmospheric Research Mesoscale and Microscale Meteorology Division's image archive was used to search through April through September of 2009 through 2011 to find every linear MCS located between the Rocky Mountains and the Appalachian Mountains and on the cool side of a surface front as analyzed by the Hydrometeorological Prediction Center (HPC). Possible cases were then further condensed using Stage IV data by selecting time intervals that produced easily discernible swaths of heavy rainfall of greater than 50 mm over a 6-hour period. Using these restrictions, forty-two unique six-hour intervals were found, ranging from April 13 to August 18 (Fig 3.1). The actual number of linear MCSs was lower because we broke up the events into 6-hour intervals, which increases the number by 11. These six hour intervals were chosen based not on the timing of the initial convection, but rather predetermined 6-hour intervals, i.e. 0000 UTC to 0600 UTC, etc.

3.2 Observed Data Set

To evaluate the forecasts, the National Stage IV Quantitative Precipitation Estimate (QPE) product (Fulton et al. 1998; Lin and Mitchell 2005) for the corresponding 6-hour intervals was obtained from the National Center for Atmospheric Research Earth Observing Laboratory. This data set is a multi-sensor (radar and rain gauge) regional precipitation analysis produced at the twelve River Forecast Centers (RFCs). This analysis includes a manual quality control performed at each of the RFCs and is then mosaicked into a national product on the 4 kilometer

NWP Hydrologic Rainfall Analysis Project grid. The data set has been used in a multitude of previous studies (over 604 citations of the Fulton et al. paper) and is widely viewed as the best available public data set for observed precipitation. Its limitations include areas with a sparse rain gauge network and unconfident radar estimates, in particular in the two mountain ranges, which are outside this study area.

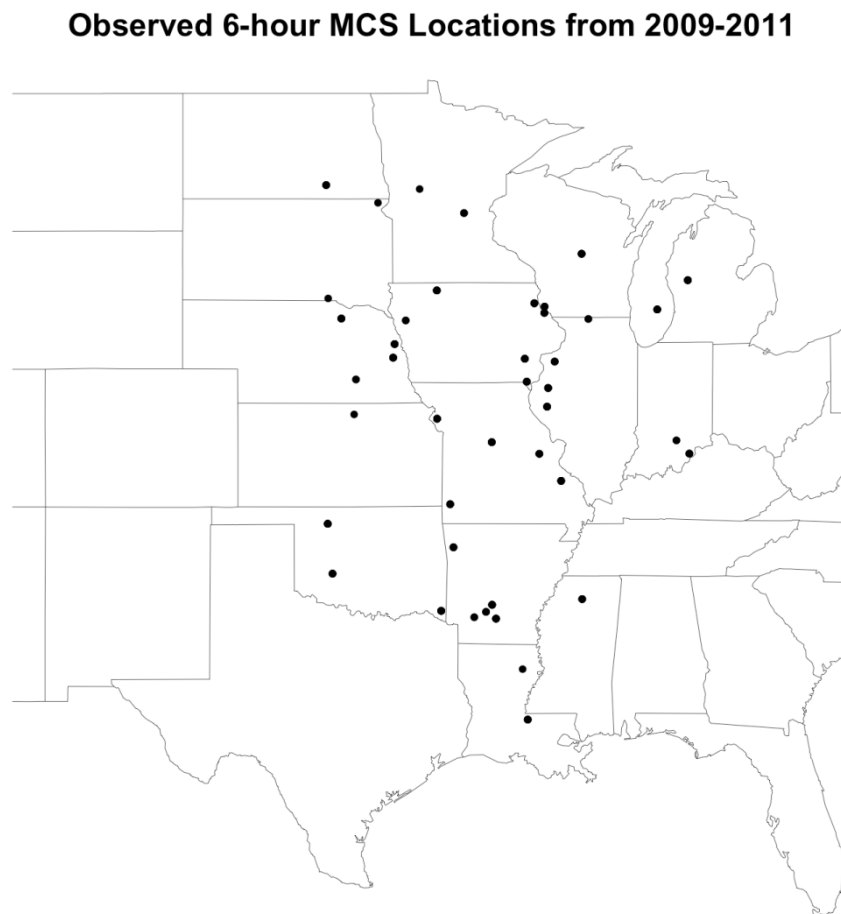


Figure 3.1: The observed 6-hour MCS locations from 2009 to 2011.

3.3 Operational and High Resolution Models

Three operational models with parameterized deep convection and one convection-allowing model were verified against the National Stage IV QPE analysis to investigate a possible northern bias in their MCS forecast locations. The North American Mesoscale (NAM), Global Forecast System (GFS), and the European Centre for Medium-Range Weather Forecasts (ECM) models were all analyzed. The National Severe Storms Laboratory (NSSL) Weather Research and Forecasting (WRF) model was also analyzed. The NAM, GFS, and ECM models are run at 0000 UTC and 1200 UTC to correspond with concurrent upper air soundings around the world to provide the “best guess” of the atmosphere. The GFS and NAM models also run at 0600 UTC and 1800 UTC, but these times, while beneficial for weather forecasters, will not be examined for this study. As with all operational models, their configurations are often upgraded, and these configurations will be listed below.

The NAM model is a regional numerical weather prediction (NWP) model run over the continental United States (CONUS) using the Weather Research and Forecast Non-hydrostatic Mesoscale Model (WRF-NMM). It currently is run with a 12 km horizontal grid spacing out to 84 hours. The Betts-Miller-Janjic (BMJ) convective parameterization is used in the NAM, and no major changes were made to the NAM during the study period. The initialization of every NAM model run will be used as the analysis of the atmospheric state in this study (NOAA 2012).

The GFS model is a global NWP model run with a spectral truncation of T574 for the first 192 hours of the forecast. A bulk mass-flux parameterization is used for both the shallow and deep convection. The GFS model went through a major and a minor upgrade during the study period. On 27 July 2010, the GFS increased resolution from T382 (32 km) to T574 (27 km), designating it as a minor upgrade from NCEP. On 9 May 2011, the GFS went through a

major upgrade to GFS 9.0.1, including upgrades to the shallow and deep convective parameterization (NOAA 2012).

The ECMWF model (hereinafter abbreviated ECM) is a global model with runs every twelve hours and a spectral truncation of T1279 out to 240 hours. The ECM model also went through a major resolution upgrade during the middle of the study period. On 26 January 2010, the ECM model upgraded its resolution from T799 to T 1279, or roughly 25 km to 16 km (ECMWF-HRI 2012).

The high resolution model used in this study is the NSSL-WRF, which is run once a day at 0000 UTC out to 36 hours. The model has a horizontal grid spacing of 4 km for the sub-CONUS with no convective parameterization, a Mellor-Yamada-Janjic planetary boundary scheme, and a time step of 24 seconds. The NSSL-WRF model uses the NAM model for initial and lateral boundary conditions, which will be of importance when comparing it to the NAM model. This data set was only available for our use for the cases in 2009 and 2010.

3.4 Temporal Dimension

In order to see how each model does over time, a temporal dimension associated with the verification of the models' forecasts was added. Named "first forecast", this is the most recent model forecast valid for the corresponding time period. The second and third forecasts are respectively the second and third most recent forecasts valid for that time period, out to 6 forecasts. For example, the naming convention for the forecasts valid 0600 UTC to 1200 UTC time period is shown in Table 3.1. Because of the use of only the 0000 UTC and 1200 UTC runs of the operational models, not all forecasts have the same lead time. For example, the 1st forecast for the 0000 UTC forecast to 0600 UTC time period is a 6-hour forecast from the 0000 UTC

model run. However, the 1st forecast for the 0600 UTC to 1200 UTC time period is a 12-hour forecast from that same model run. They are both the most recent forecast for each time period but with different lead times, representing one potential limitation of the study.

Table 3.1: Example forecasts and their forecast times valid for the 0600 UTC to 1200 UTC time period

	Model Run (UTC)	Forecast time (hours)
1st Forecast	0000	6 to 12
2nd Forecast	1200	18 to 24
3rd Forecast	0000	30 to 36
4th Forecast	1200	42 to 48
5th Forecast	0000	54 to 60
6th Forecast	1200	66 to 72

3.5 MODE Tool

The MODE tool is produced by the Developmental Testbed Center and is included in their Model Evaluation Tools (MET), which is a suite of verification tools to verify and evaluate numerical weather forecasts. The MODE tool resolves any two fields into objects and computes statistics on these objects, both individually and paired. Example statistics computed are centroid location, object area, length, and width, axis angle, aspect ratio, curvature, and intensity. Although any two fields can be resolved, the observed and forecasted precipitation fields are used in this study.

The MODE tool uses convolved, masked, and filtered steps, along with important settings to resolve the fields into objects, as shown in Fig. 3.2 and described in detail by Davis et al. (2006). The settings used were selected based on rigorous sensitivity testing (not included here) to match what a human would draw. Table 3.2 shows the settings used for all four models.

MODE: APCP_06 at A6 vs APCP_06 at A06
Forecast

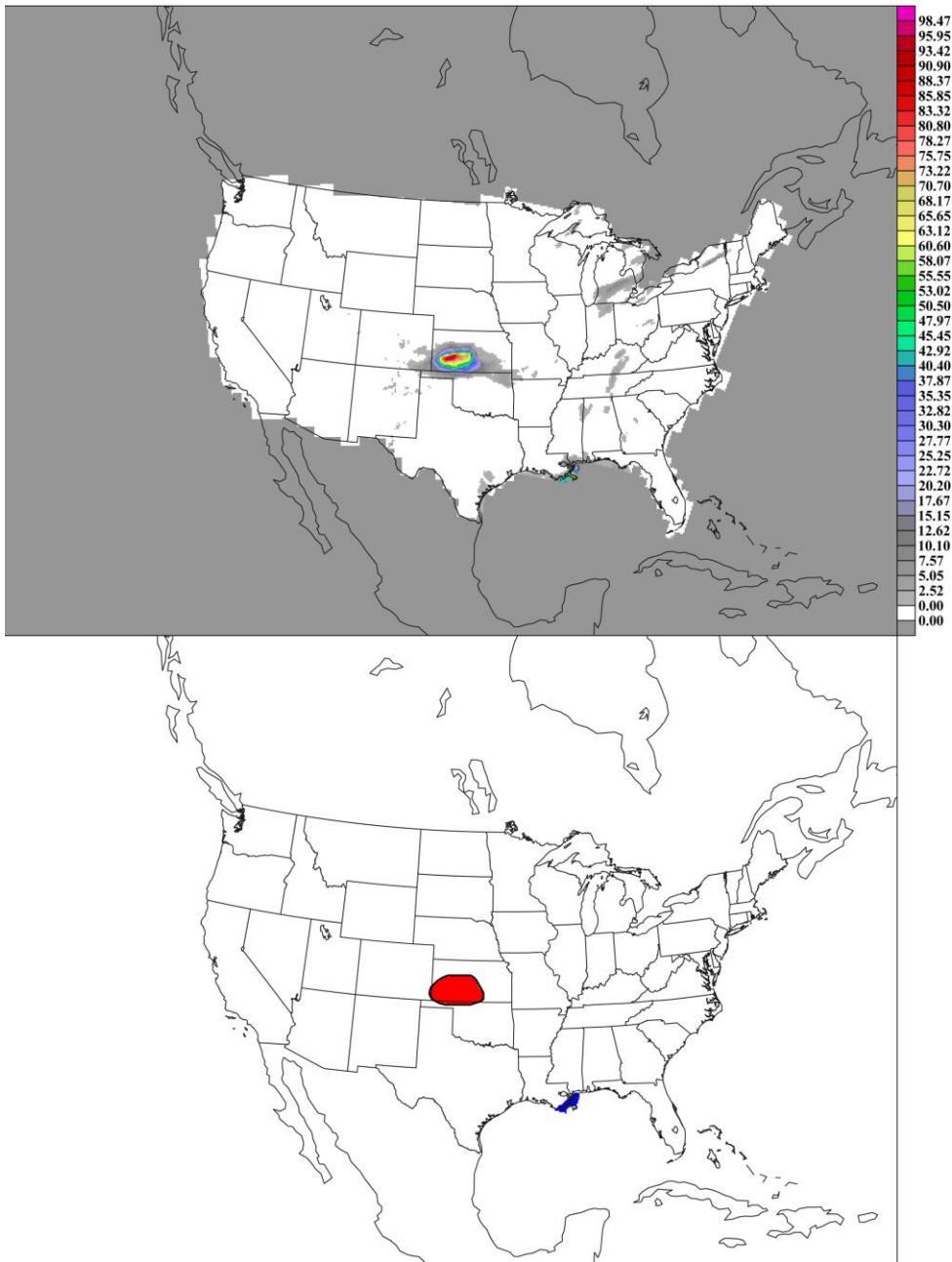


Figure 3.5: Example of the final objects produced by the MODE tool for 18 Aug. 2009.

The GFS and ECM models were both regridded to the 212 grids, which is a regional Lambert Conformal grid with a 40-km grid increment, while the NAM and NSSL-WRF models stayed at their same grid. The Stage IV data was regridded to match the corresponding model's new or same grid. Figure 3.5 shows an example of the final objects oriented by the MODE tool.

Table 3.2: MODE tool settings used to define objects in both the observed and forecasted precipitation fields for each model.

Model	Radius (grid points)	Threshold (mm)
GFS	4	≥ 7.5
NAM	6	≥ 10
ECM	4	≥ 7.5
NSSL-WRF	12	≥ 12.7

3.6 Selection of Matching Forecasts and Calculation of Displacement Error

In order to objectively analyze MCS location, the centroid value from the MODE tool was used as the “center of mass” of each of the resolved objects. However, some subjectivity is involved in the matching of a forecast MCS to the observed MCS. Not every forecast produced an MCS or could have for the wrong reasons in a different part of the country. For this reason, each observed object was manually matched to a forecasted object at the discretion of the author. Although offering some subjectivity in the objective analysis, the author erred on the side of caution and three forecast types were not included in the MODE tool analysis if the forecast:

- (1) did not forecast any precipitation in the immediate or surrounding areas.
- (2) produced either an MCS or some precipitation in the area but was not enough for the MODE tool to resolve an object.

(3) forecasted an MCS a substantially farther distance, rendering it unclear if the rain event corresponds to the observed or if a different MCS was forecasted for different reasons

Of the reasons for not including a forecast, number three presents the most work for determining if a forecast actually corresponded to the observed. For this reason, they were not included and possible future work on this matter is necessary. The category “Missed” in the following tables for each model is the number for forecasts that weren’t included in the MODE tool analysis.

The latitude and longitude of the observed object was subtracted from the forecasted object’s latitude and longitude using the haversine formula (Formula 3.1), which produces a distance in km:

$$\text{haversin}\left(\frac{d}{r}\right) = \text{haversin}(\phi_2 - \phi_1) + \cos(\phi_1) \cos(\phi_2) \text{haversin}(\lambda_2 - \lambda_1) \quad (3.1)$$

where *haversin* is the *haversine* function:

$$\text{haversin}(\theta) = \sin^2\left(\frac{\theta}{2}\right) = \frac{1 - \cos(\theta)}{2}$$

and d is the distance between the two points, r is the radius of the sphere, ϕ_1, ϕ_2 is the latitude of point 1 and latitude of point 2, and λ_1, λ_2 is the longitude of point 1 and longitude of point 2. This distance is effectively the distance of the forecasted object’s centroid from the observed object’s centroid, which can then be plotted on a Cartesian plane with every observed object normalized to the origin and forecasted objects reduced to points in the plane. Other statistics on the observed and forecasted objects can be evaluated based on this distance.

In order to assess that the results are significant, a bootstrapping technique is used (Wilks 1995). A random resampling with repeating points was conducted a thousand times with the

lowest and highest 5% not included. The intersection of each error bar also shows the median x and median y placement.

3.7 Manual Verification

In order to confirm that the objective process for identifying forecasted MCSs relative to the observed using the MODE tool resulted in an accurate representation of what a human would locate, a manual analysis was also conducted. The manual analysis located the center of mass of each precipitation bulls eye in both fields, overlaid Cartesian X-Y axes, and noted where the forecasted MCS location was relative to the observed location, as seen in Figure 3.7. Because this was a rudimentary graphing, the units are quasi-unitless with one unit roughly equal to 3 degrees latitude and longitude. Although these overlays were done by hand, the manual analysis is an easy and humanistic way to display the displacements just for verifying the MODE Tool results.

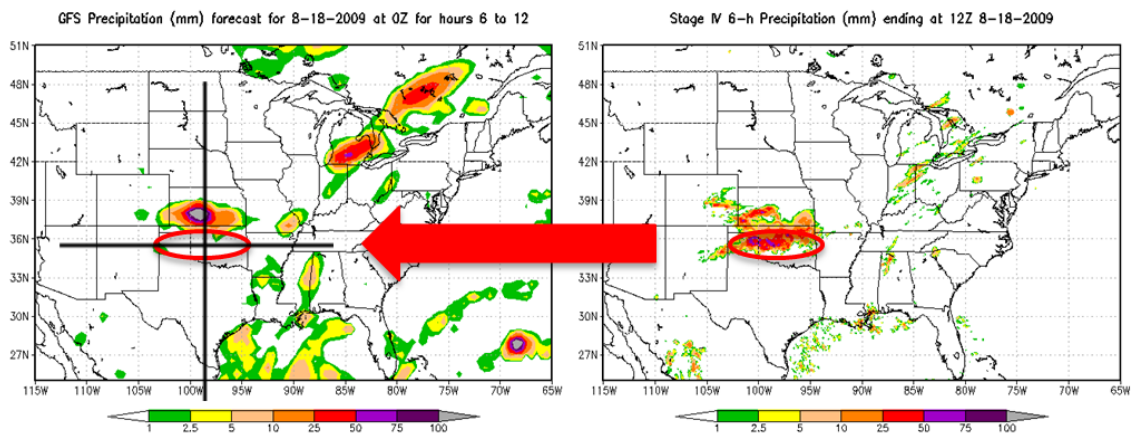


Figure 3.7: Manual analysis example showing the location of the observed MCS and the overlay onto the forecasted field.

CHAPTER 4

FORECAST LOCATION RESULTS

4.1 North American Mesoscale Model

Among the four models studied here, the NAM model had the second most displacement errors with 68% of the cases forecasted too far to the north, or too far on the cool side of the boundary, as shown in Figure 4.1.1. The median x and y displacements of the forecasted objects were well to the north at a location of 63 km to the north and 25 km to the west. A perfectly unbiased forecast set would have the median x and y displacements at the origin. Looking at just

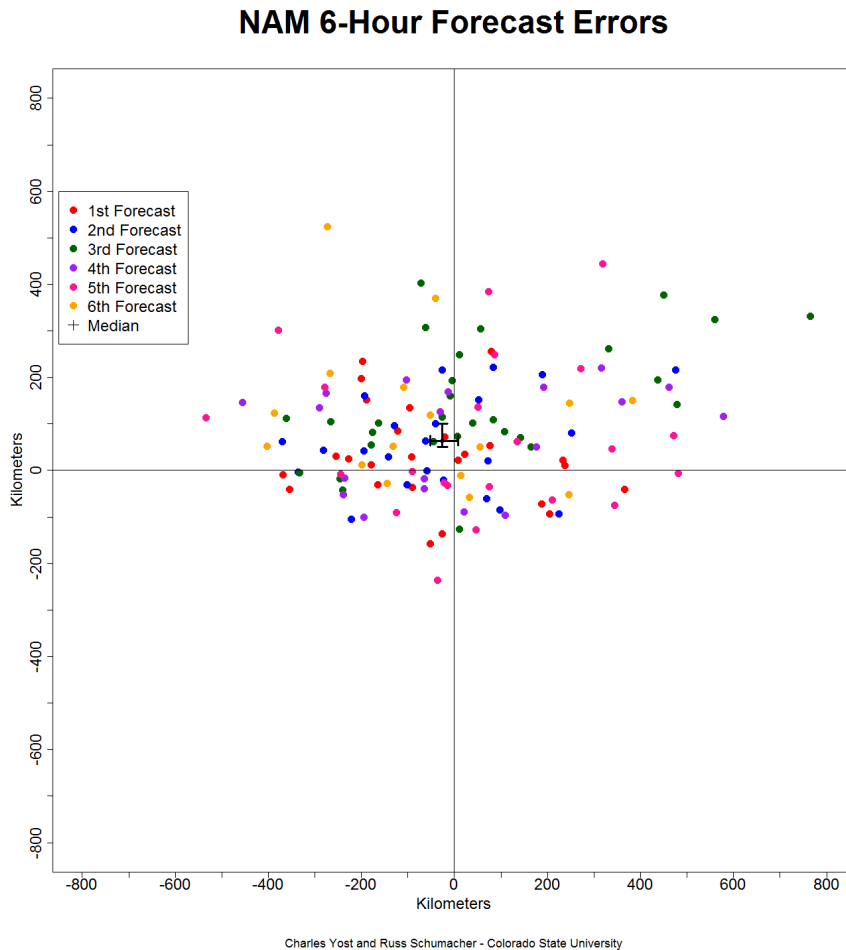


Figure 4.1.1: NAM MCS forecast locations relative to the observed MCS locations using the MODE tool for all forecast times for all years of the study period.

the first 3 forecasts, as shown in Figure 4.1.2, the forecasted MCSs were again located to the north, with 73% located to the north, the median x displacement increasing to 26.4 km west of the origin and the y displacement remaining the same. These forecasts are between a six hour forecast and a day and a half forecast, with this being what a forecaster would look to for short-term guidance. There is a slight hint of a Western bias, with median x displacement west of the $x=0$ line. This is indicative of the forecasted system moving too slowly or the convection initiating too far to the west. Looking at the day and a half forecast to the three day forecast

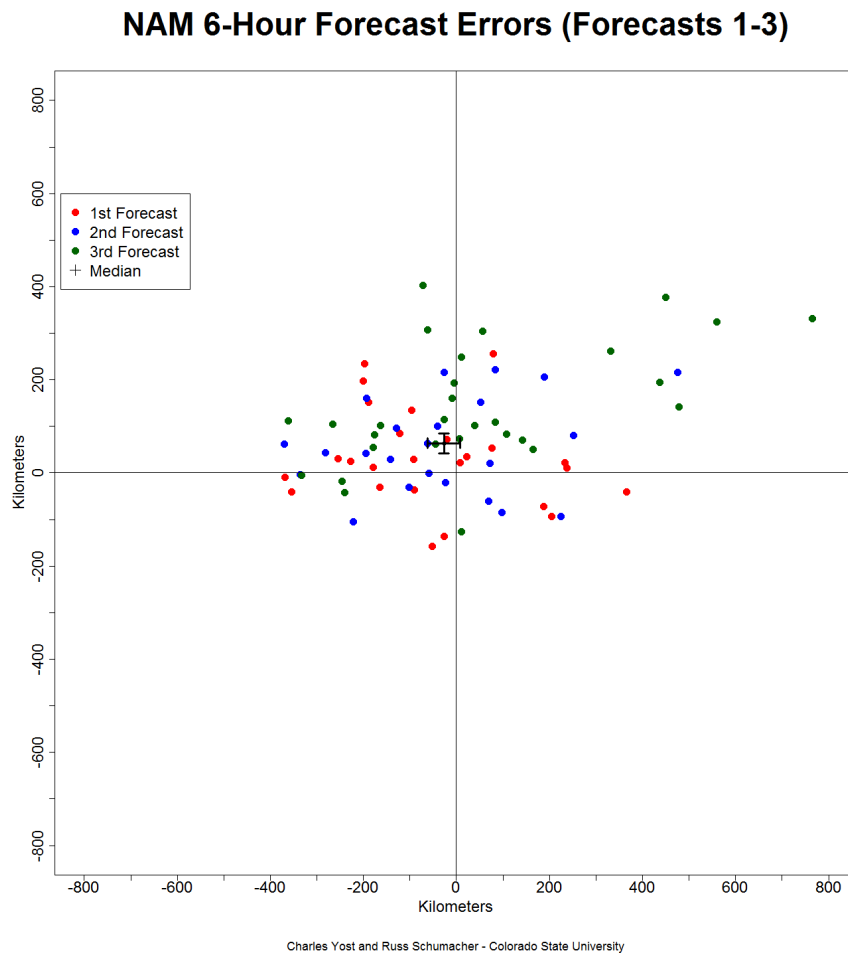


Figure 4.1.2: NAM MCS forecast locations relative to the observed MCS locations using the MODE tool for forecast 1-3 for all years of the study period. the median y displacement as shifted slightly north to 68.7 km and the median x displacement

subset (forecasts 4-6), has shifted slightly neutral to 18.9 km. The same northern bias persists in the later forecasts with still 63% of the cases forecasted too far on the cool side of the boundary. It is curious to note that although the overall percentage of cases to the north is lower, the spread of the northern cases is more in all directions. This decrease in percentage of forecasts too far to the north hints at some value associated with these forecasts with respect to MCS location, yet is nearly cancelled by the decrease in precision of these northern cases.

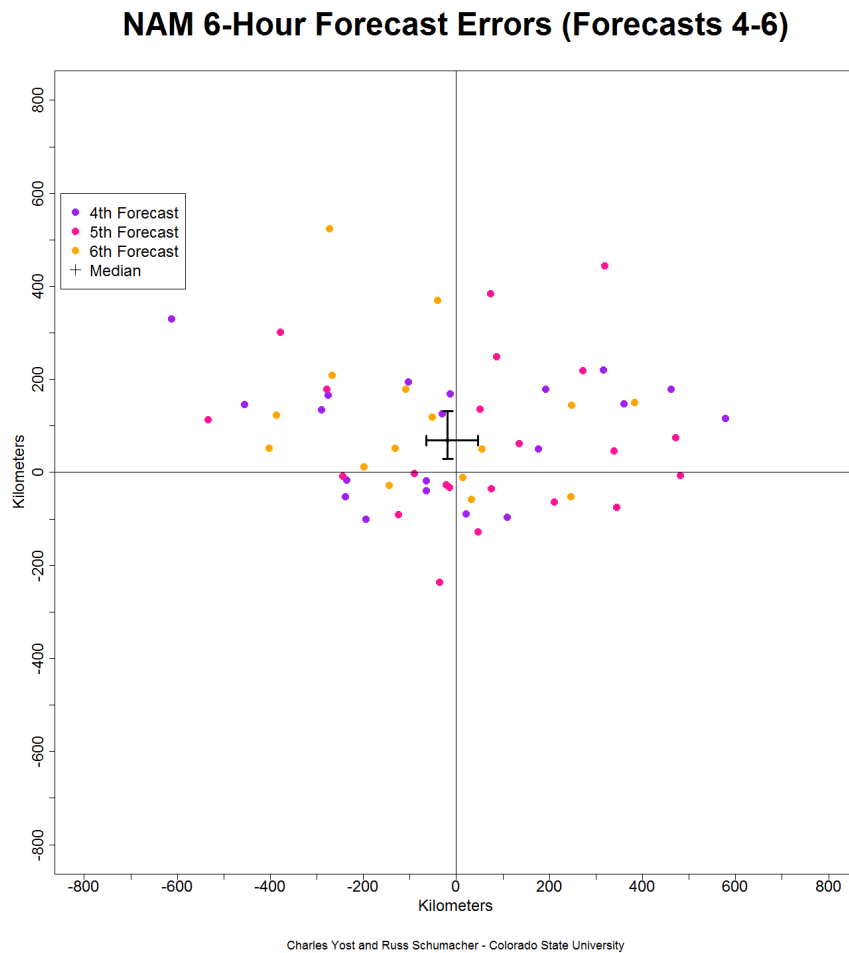


Figure 4.1.3: NAM MCS forecast locations relative to the observed MCS locations using the MODE tool for the last three forecast times for all years of the study period.

The average distance from the observed object to the forecasted object broken down by quadrant in Table 4.1.1 and echoes the same interpretation noted earlier. The forecasts in the northern quadrants have a larger mean displacement error than those to the south. This is likely a combination of the inaccuracy associated with the entire forecasted object set offset to the north and the imprecision of the later northern forecasts. The mean, median and standard

Table 4.1.1: NAM model’s MCS forecast location statistics over all forecast times for the entire study period broken down by quadrant with the average displacement from the observed object.

Quadrant	Number of Points	Percentage	Mean (km)
1 (NE)	43	32%	301.9
2 (NW)	49	36%	261.5
3 (SW)	26	19%	180
4 (SE)	17	13%	190

deviation of 2 subsets and each forecast paints an expected picture in Table 4.1.2. An increase in mean forecast displacement of all points from forecasts 1-3 and forecasts 4-6 is due to this imprecision in the later forecast times and is expected with greater lead times. A general increase of mean displacement from early lead times to later lead times is shown with each increasing forecast, except in forecasts 5 and 6. This leveling off in the last two forecasts is due to the model’s inability to forecast anything resembling the observed precipitation, with a 33% decrease in number of forecasted objects from forecasts 1 and 2 to forecast 5 and 6. The objects the model does forecast in the later time period are likely due to a clear solution that is present in the cases too far to the south. The same model degradation in increasing lead times can be seen in the increasing median and standard deviation of the forecast displacement. The NAM model had 38% of all forecasts not included, with more forecasts included in the earlier forecasts. The average distance was lower in the earlier forecasts that had lower percentage of misses, but it is

impossible to determine if it is due to the shorter lead times, or the increase in predictability of events. Further work is needed to help delineate this difference.

Table 4.1.2: NAM model’s MCS forecast location statistics of all forecast times for the entire study period of the average, median, and standard deviation of the distance from the observed object.

	Mean (km)	Median (km)	Stand. Dev. (km)	Missed
Forecasts 1-6	249.7	228.9	154.3	38%
Forecasts 1-3	231.8	202.1	145.4	30%
Forecasts 4-6	273.5	244.2	163.6	46%
Forecast 1	198.7	201.1	97.4	32%
Forecast 2	200.5	198.8	115.7	37%
Forecast 3	285.1	244.1	184.3	24%
Forecast 4	286.0	240.3	174.1	45%
Forecast 5	276.9	254.1	164.1	40%
Forecast 6	252.9	230.1	158.1	54%

4.2 Global Forecast System Model

The GFS model, with the coarsest model resolution, had the largest northern bias with 74% of the forecasted MCSs located on the cool side of the boundary. The median y displacement for all points over all forecasts is 83 km to the north. There also is an eastern bias with the GFS model’s MCS forecasts, with 65% of the forecasted objects to the east and a median x displacement of 79 km. The forecasted objects to the east are also less precise compared to the objects to the west, with a greater range of values (from visual inspection). Also by examining Figure 4.2.1, there is a greater extent of objects laterally in the east and west direction than north and south. Objects basically extend from 200 km to the south of an observed object to 400 km to the north of an observed object. However, objects did exist that were nearly 500 km to the west and over 600 km to the east of an observed object. This orientation of

GFS 6-Hour Forecast Errors

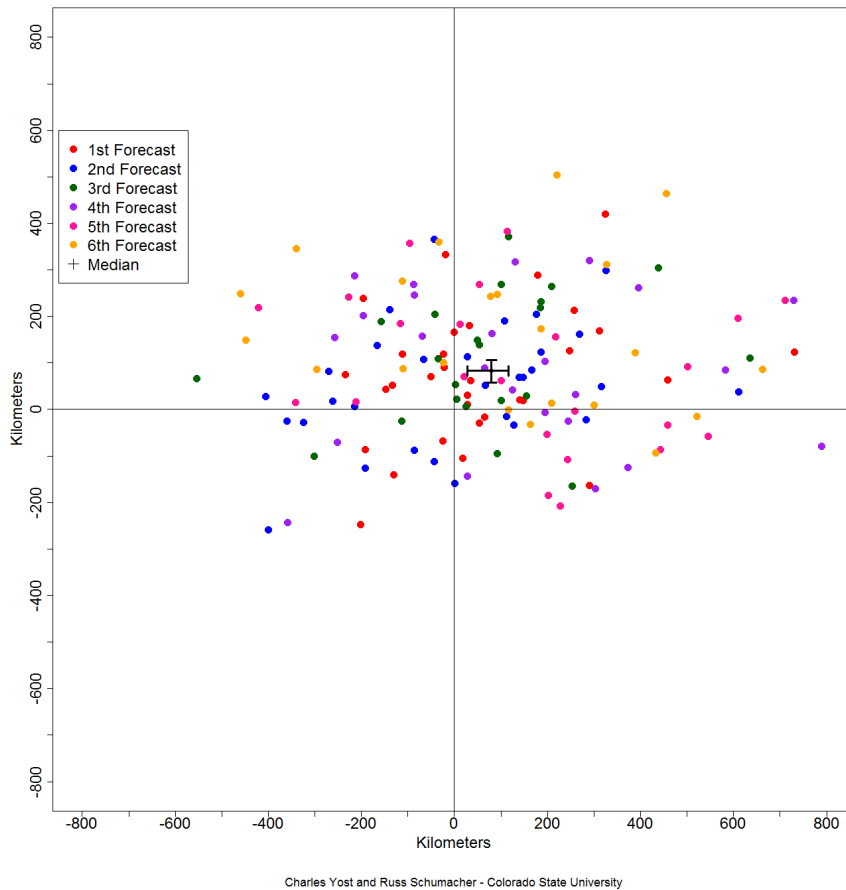


Figure 4.2.1: GFS MCS forecast locations relative to the observed MCS locations using the MODE tool for all forecast times for all years of the study period.

The displacement error is expected because of the setup of these extreme rain events. The north/south location of these events are governed by the location of a boundary. This arrangement leaves a smaller lateral north/south extent to be incorrect. The east/west imprecision is a lot more complicated and may include timing of the event, speed of the event, and even more complicated storm-scale dynamics with the locations of the start of the training cells.

Sub-setting just the first 3 forecasts, 47% of the cases were in just the northeast quadrant, signifying a clear northward and eastward bias is present even in the closer 6-hour to a day and a half range of forecasts (Fig. 4.2.2). While the number of cases was greater (60%) in the eastern

quadrants, the median x displacement is closer to neutral with a value of 28 km and is just barely statistically different from zero. While the GFS model favors forecasting more numerous MCSs to the northeast, it produces a smaller amount to the northwest but with the same variance in forecast location. These more numerous forecasted events to the northeast are closer towards neutral, causing the median x displacement to shift towards neutral, but not changing the percentage of points in that quadrant. The median y displacement decreases by 20 km in this subset, signaling a forecast bias closer to neutral.

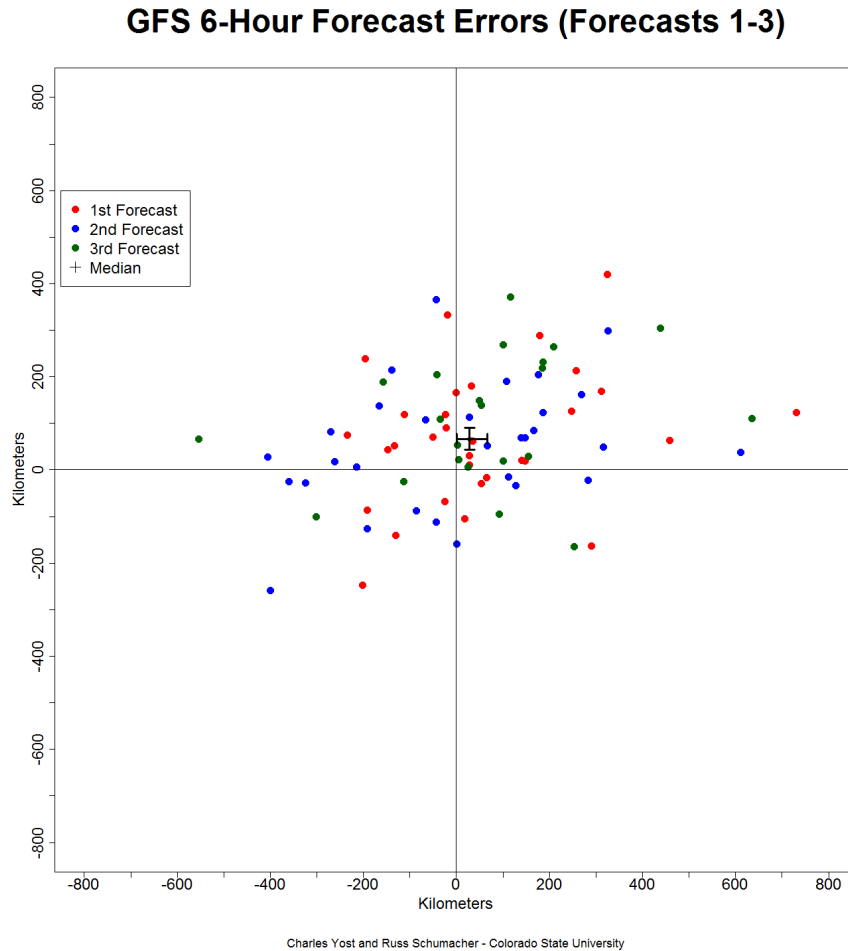


Figure 4.2.2: GFS MCS forecast locations relative to the observed MCS locations using the MODE tool for the first three forecast times for all years of the study period.

The longer 3 forecasts showed the greater variance of displacement errors with 70% of the cases too far to the north and over half (54%) of the objects in the northeastward quadrant alone (Fig. 4.2.3). The same eastward bias is present in the later forecast times with the exact number of points to the east of the observed as to the north. The latest 2 forecasts (5 and 6) had zero objects forecasted to the southwest of the observed.

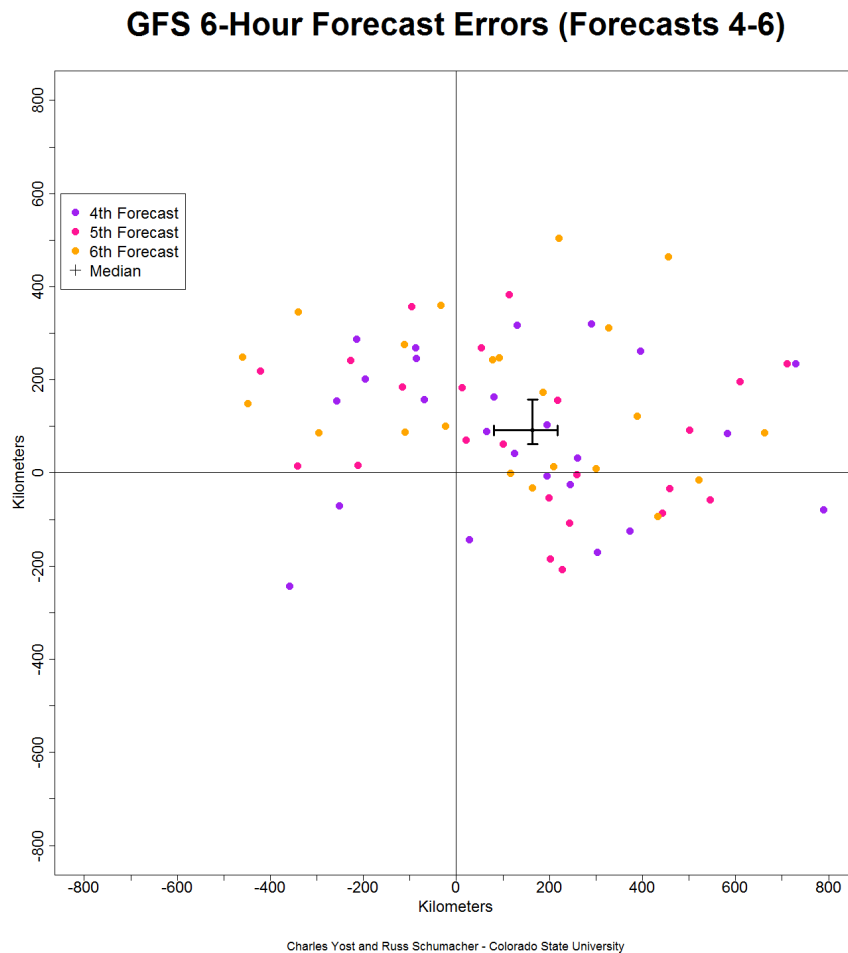


Figure 4.2.3: GFS MCS forecast locations relative to the observed MCS locations using the MODE tool for the last three forecast times for all years of the study period.

As shown in Table 4.2.1 and mentioned previously, the GFS model forecasted the MCS locations in the 1st and 4th quadrants at a greater distance away from the observed with a mean displacement of 307.9 km and 329.9 km, respectively. In respect to average displacement

distance, the mean performed considerably better in the first three forecasts compared to the final three with an average distance error increase of 126 km, resulting in a total mean displacement of 297.1 km (Table 4.2.2). This drastic difference between the two sets is shown vividly in the forecast breakdown, with the first three having mean displacement errors of 220.5, 252.1, 247.1, respectively, while the latter three were more than 100 km each than any of the first two. This large discrepancy is echoed in the median with a 165 km increase between the first forecast and sixth forecast. The standard deviation of displacement error remained relatively constant throughout all time periods with an anomalous jump in the fourth forecast. The GFS model had similar numbers of missed forecasts compared to the NAM model, with a clear bifurcation of missed forecasts between the early forecasts and later forecasts at 33% and 42%, respectively.

Table 4.2.1: GFS model’s MCS forecast location statistics over all forecast times for the entire study period broken down by quadrant with the average displacement from the observed object.

Quadrant	Number of Points	Percentage	Mean (km)
1 (NE)	68	44%	307.9
2 (NW)	42	30%	270.7
3 (SW)	14	9%	254.1
4 (SE)	30	21%	329.8

Table 4.2.2: GFS model’s MCS forecast location statistics of all forecast times for the entire study period of the average, median, and standard deviation of the displacement from the observed object.

	Mean (km)	Median (km)	Stand. Dev. (km)	Missed
Forecasts 1-6	297.1	267.1	186.4	37%
Forecasts 1-3	239.0	214.5	149.9	33%
Forecasts 4-6	365.1	307.8	202.4	42%
Forecast 1	220.5	166.5	160.0	24%
Forecast 2	252.1	226.7	124.1	26%
Forecast 3	247.1	227.7	170.7	46%
Forecast 4	386.5	290.9	257.4	36%
Forecast 5	344.9	308.3	165.1	43%
Forecast 6	361.1	334.4	167.4	46%

4.3 European Centre for Medium Range Weather Forecasts Model

In terms of displacement Biases, the ECM model performed the best out of the operational models with 64% of the forecasted objects located too far to the north, and with a median y displacement of 32.8 km, the model was both accurate and precise. With a median x displacement of 3.3 km and an equal splitting of cases east and west, the ECM model was statistically neutral with respect to an east/west bias, as shown in Figure 4.3.1.

Looking at just the first three forecasts (Fig. 4.3.1) shows even less of a bias. Only 61% of the forecasted objects were located too far to the north, with a statistically significant northward bias but a median y-displacement of only 18.5 km. Also, by visually removing the outliers, the model’s forecasted MCS locations look both accurate and precise. One curious item to note about the 1st forecast is that a majority of the forecasted precipitation objects are extremely close to the observed objects except located directly to the south of the observed objects, as shown in Figure 4.3.2. For just the 1st forecast, the model had slight southern bias with 58% of the cases

located to the south of the observed. Also, taking a median of just these southern cases in the 1st forecast also shows this slight westward congregation with a median y displacement of 35 km to the west.

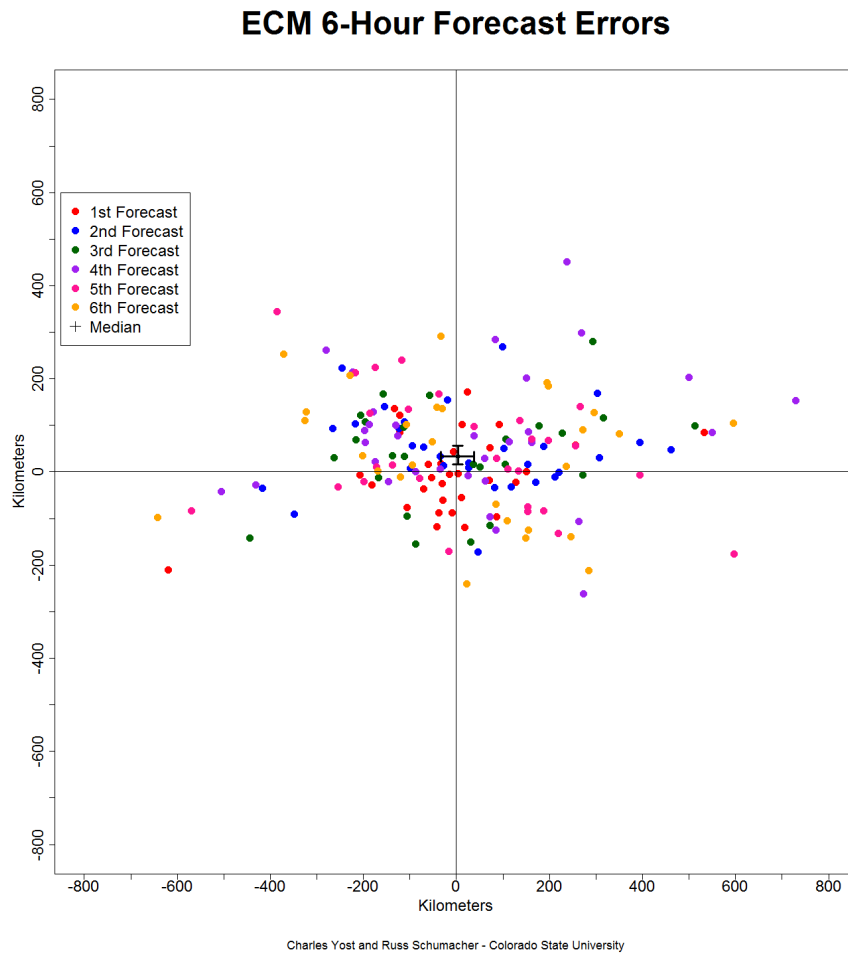


Figure 4.3.1: ECM model's MCS forecast locations relative to the observed MCS locations using the MODE tool for the first three forecast times for all years of the study period.

Examining just forecasts 4-6 shows the cause for the high mean values to the north. Like the GFS model's imprecise northern, later forecasts, the forecasted objects to the north display a large spread northward compared to the Southern objects at that time. Taking the standard deviation of just those northern objects' x displacement clearly shows this spread with a value of

213 km. A standard deviation of 151 km for the total displacement error for just forecasts 4-6 helps to increase the standard deviation for all forecast times from 128 km for the first three forecasts to 144 km for all forecasts.

Looking at the ECM model's MCS forecast location statistics in tables 4.3.1 and 4.3.2, shows the expected model's forecast degradation with lead times. The high means in the first and third quadrant are likely due to a string of outliers located extremely far out from the observed MCSs in a nearly identical but opposite locations. The mean displacement errors increases with

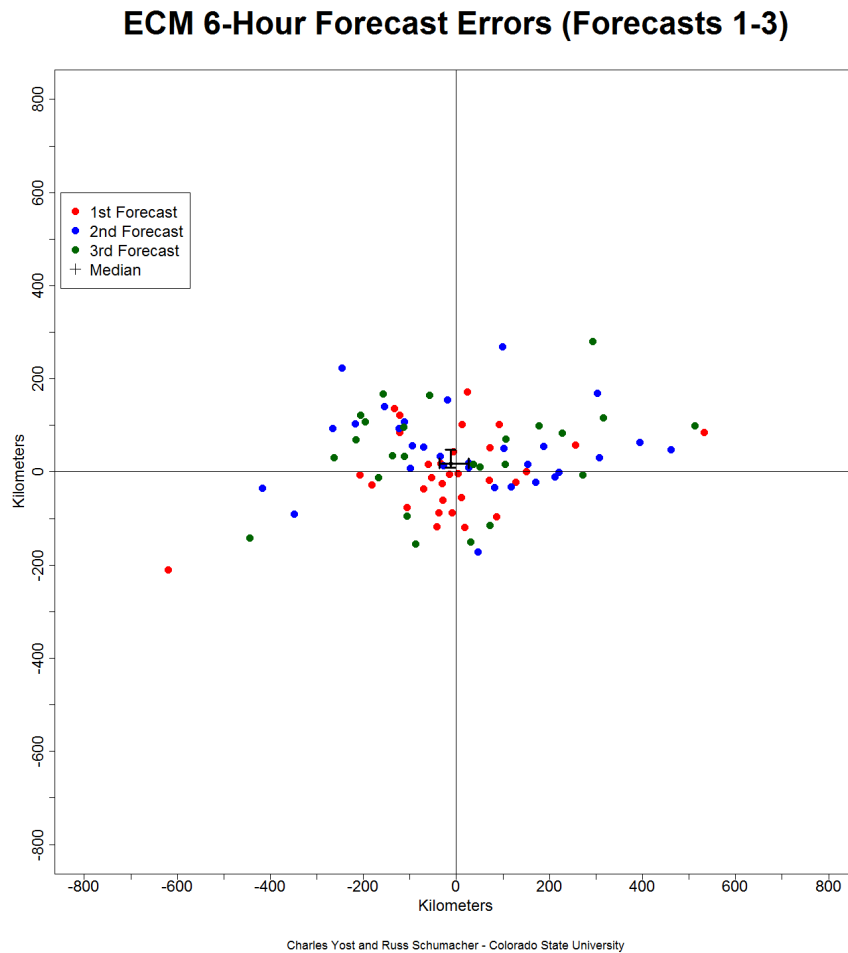


Figure 4.3.2: ECM model's MCS forecast locations relative to the observed MCS locations using the MODE tool for the first three forecast times for all years of the study period.

forecast lead times, as does the median forecast location. The standard deviation of forecast displacement errors remains relatively the same for all forecast times, except the 4th forecast, which can be noted on Figure 4.3.3. The ECM model performed the best with respect to missed forecasts, only missing 29% of all forecasts. The ECM model also had a consistently low miss rate of forecasts throughout all lead times, likely owing to the ECM model's forecasting at least something in the general area that the MODE tool can pick up.

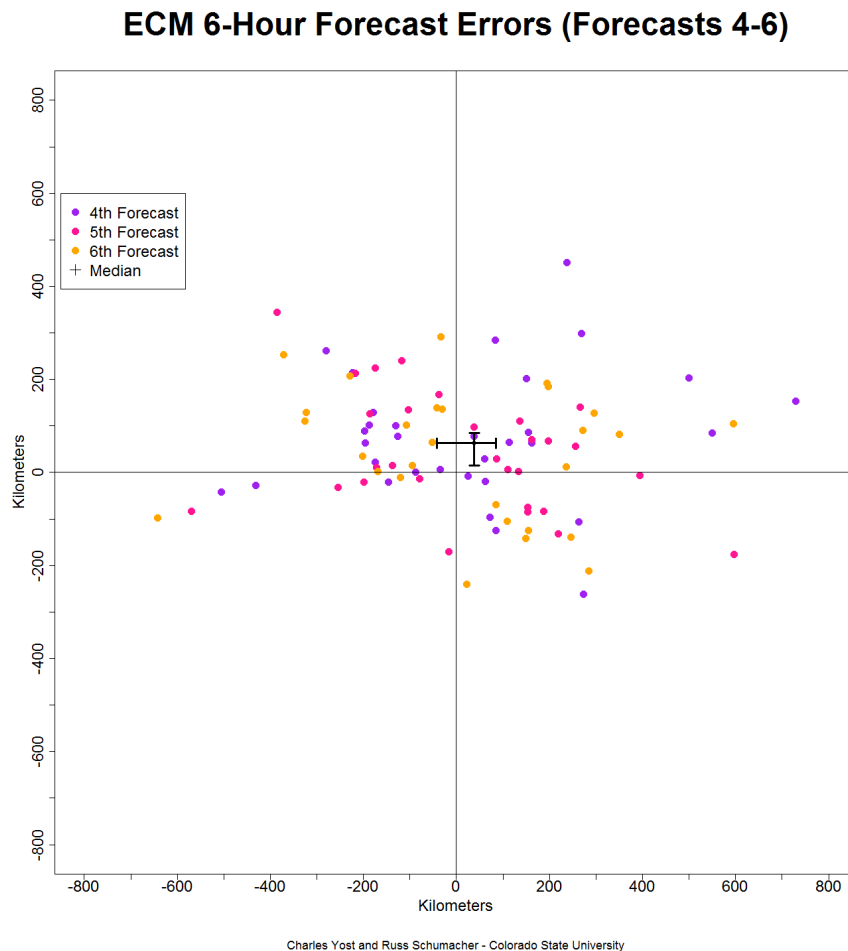


Figure 4.3.3: ECM model's MCS forecast locations relative to the observed MCS locations using the MODE tool for the last three forecast times for all years of the study period.

Table 4.3.1: ECM model’s MCS forecast location statistics over all forecast times for the entire study period broken down by quadrant with the average displacement from the observed object.

Quadrant	Number of Points	Percentage	Mean (km)
1 (NE)	54	31%	253.1
2 (NW)	59	34%	194.5
3 (SW)	28	16%	236.2
4 (SE)	34	19%	189.9

Table 4.3.2: ECM model’s MCS forecast location statistics of all forecast times for the entire study period of the average, median, and standard deviation of the displacement from the observed object.

	Mean (km)	Median (km)	Stand. Dev. (km)	Missed
Forecasts 1-6	218.3	176.0	144.3	29%
Forecasts 1-3	182.4	154.2	128.4	30%
Forecasts 4-6	253.1	209.1	151.0	28%
Forecasts 1	140.7	120.2	136.1	24%
Forecasts 2	200.3	175.4	121.1	27%
Forecasts 3	212.6	177.3	117.6	39%
Forecasts 4	256.6	209.5	176.0	21%
Forecasts 5	238.5	200.0	135.8	29%
Forecasts 6	264.1	255.7	138.7	32%

4.4 National Severe Storms Laboratory Weather Research and Forecasting Model

Although the NSSL-WRF was only run once a day and out to only 36 hours, it has a near neutral forecast displacement of its MCS locations with 47.2% of forecasted objects located too far to the north, leaving a slight southern bias (Table 4.4.1). The median x displacement is slightly Western at 13 km with a southern median x displacement of 24 km that was not statistically significant (Fig. 4.4.1). Although it is a small sample size, the mean of displacement

4-km NSSL 6-Hour Forecast Errors

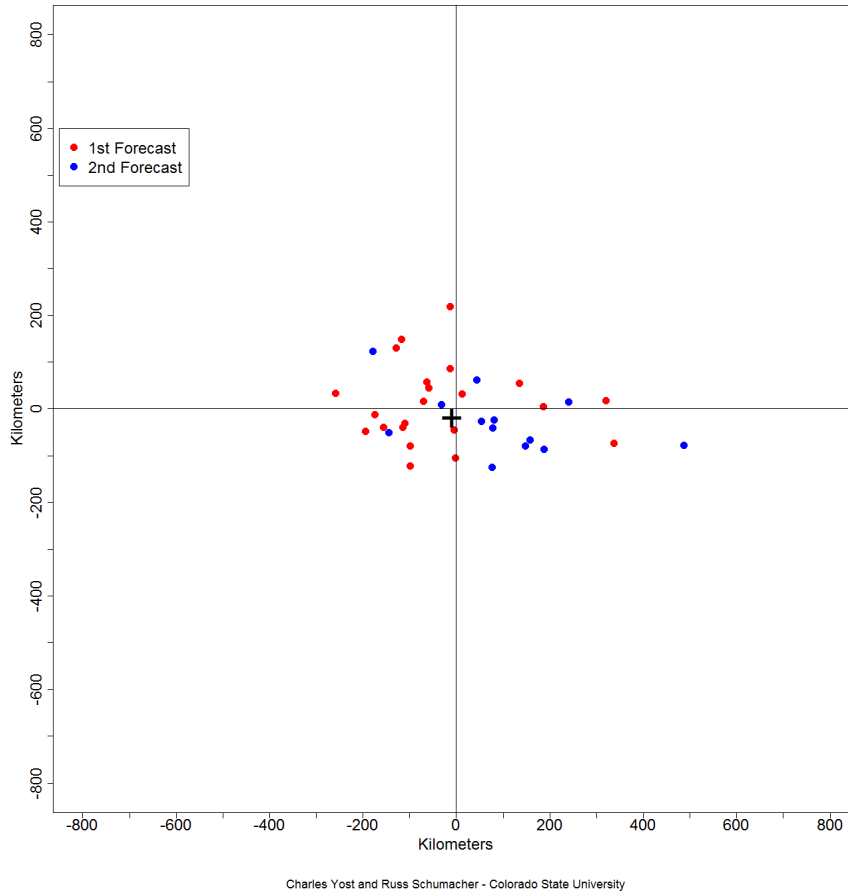


Figure 4.4.1: NSSL-WRF model’s MCS forecast locations relative to the observed MCS locations using the MODE tool for the first two forecast times for 2009 and 2010 of the study period.

errors for all quadrants were relatively the same with a larger value in the 4th quadrant, mainly due to a few 2nd forecasts. The mean, median and standard deviation all increased with the increasing forecast lead time. The same day forecast performed exceptionally well with a mean displacement error of 155 km. There is a hint of a Westward bias associated with the first or most recent forecast with 77% of the forecasted objects to the west of the observed. These results

are in agreement with the Marsh et al. (2012) results which found a northeastward bias of the observed relative to the forecasts (opposite notation used here) (Fig. 2.7.1).

There are a few items to note about this data set. Due to data availability, only the years 2009 and 2010 are included. Also, as previously noted, the model is only initialized and run once a day at 0000 UTC and out to only 36 hours. Another item to note is the NSSL-WRF model is initialized from the NAM model. This lack of a bias in the NSSL-WRF, that is present in the NAM model, rules out the importance of initial conditions for the NSSL-WRF. The two previously mentioned factors and this important initial conditions problem make it important, when comparing the other models, to only look at this subset of cases, which will be done in the next section. Finally, every forecast was included in the MODE tool analysis (i.e., there were no “missed” forecasts).

Table 4.4.1: NSSL-WRF model’s MCS forecast location statistics over all forecast times for the entire study period broken down by quadrant with the average displacement from the observed object.

Quadrant	Number of Points	Percentage	Mean (km)
1 (NE)	7	19.4%	167.0
2 (NW)	10	27.8%	142.4
3 (SW)	10	27.8%	135.8
4 (SE)	9	25%	195.8

Table 4.4.2: NSSL-WRF model’s MCS forecast location statistics of all forecast times for the entire study period of the average, median, and standard deviation of the displacement from the observed object.

	Mean (km)	Median (km)	Stand. Dev. (km)
Forecasts 1-2	158.5	153.6	95.2
Forecast 1	155	150.9	81.6
Forecast 2	164.4	153.5	118.0

4.5 NSSL-WRF Subset

In order to judge how the NSSL-WRF did compared to the other models, the operational models’ objects are reduced to just the subset of cases for which the NSSL-WRF forecasts were available with no forecasts “missed”. This is an important step to verify the validity of the NSSL-WRF model’s results, owing to such a small sample size and the unlikely possibility that the cases for which NSSL-WRF forecasts were available had especially high predictability. In terms of the percentage of objects displaced to the north, the GFS performed reasonably well with only 57% of the objects too far to the north, although the same eastern bias is hinted at in the first quadrant with an average displacement of 328 km. The ECM model performed closer to its complete set with 67% of its forecasts too far to the north. The NAM model’s subset actually performed technically the best with 52% of its cases too far to the north. Despite the NAM model’s anomalously even split in forecast, the NSSL-WRF model’s unbiased results seem justified with the GFS and ECM models having the same, if not worst, bias over the smaller subset.

Table 4.5.1: NAM model’s MCS forecast location statistics over just the NSSL-WRF model’s subset of the average, median, and standard deviation of the displacement from the observed object.

	Mean (km)	Median (km)	Stand. Dev. (km)
Forecasts 1-2	190.5	151.3	112.3
Forecast 1	189.9	174.0	95.9
Forecast 2	191.4	151.3	138.5

Table 4.5.2: NAM model’s MCS forecast location statistics over just the NSSL-WRF model’s subset broken down by quadrant with the average displacement from the observed object.

Quadrant	Number of Points	Percentage	Mean (km)
1 (NE)	3	13%	234
2 (NW)	9	39%	158.2
3 (SW)	6	26%	118.6
4 (SE)	5	22%	216.2

Table 4.5.3: GFS model’s MCS forecast location statistics over just the NSSL-WRF model’s subset of the average, median, and standard deviation of the displacement from the observed object.

	Mean (km)	Median (km)	Stand. Dev. (km)
Forecasts 1-2	268.9	217.4	191.9
Forecast 1	199.4	186.1	112
Forecast 2	370.8	261.6	239.2

Table 4.5.4: GFS model’s MCS forecast location statistics over just the NSSL-WRF model’s subset broken down by quadrant with the average displacement from the observed object.

Quadrant	Number of Points	Percentage	Mean (km)
1 (NE)	10	36%	328
2 (NW)	8	29%	218.8
3 (SW)	4	14%	201.9
4 (SE)	6	21%	292.1

Table 4.5.5: ECM model’s MCS forecast location statistics over just the NSSL-WRF model’s subset of the average, median, and standard deviation of the displacement from the observed object.

	Mean (km)	Median (km)	Stand. Dev. (km)
Forecasts 1-2	153.9	154.5	91.8
Forecast 1	132.5	124.9	85.1
Forecast 2	194.7	167.3	94.7

Table 4.5.6: ECM model’s MCS forecast location statistics over just the NSSL-WRF model’s subset broken down by quadrant with the average displacement from the observed object.

Quadrant	Number of Points	Percentage	Mean (km)
1 (NE)	8	30%	228.7
2 (NW)	10	37%	137.7
3 (SW)	5	18%	109.8
4 (SE)	4	15%	102.4

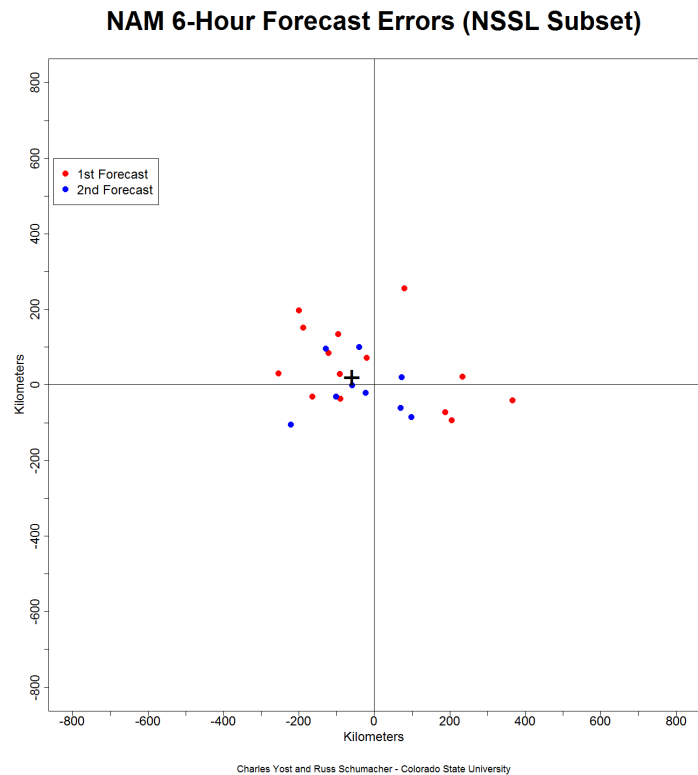
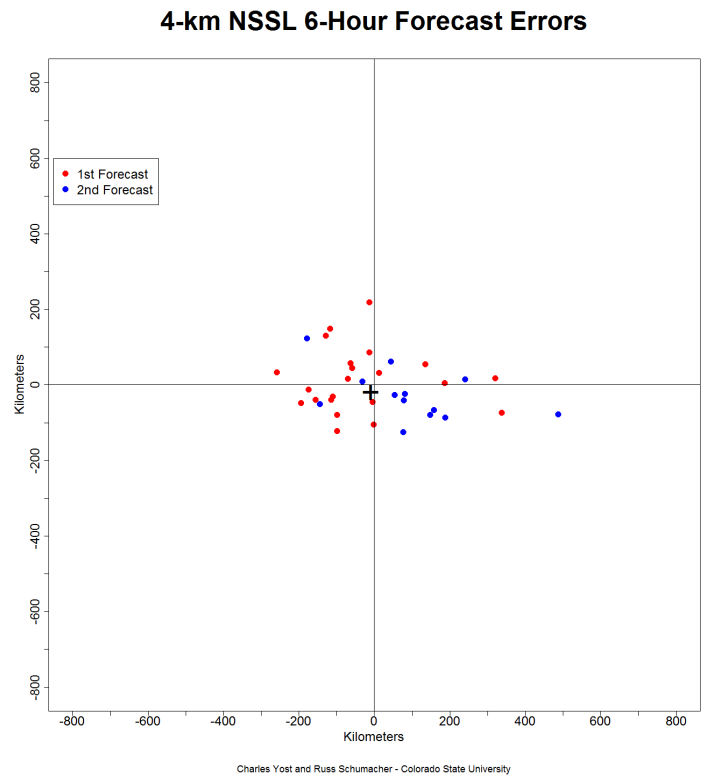


Figure 4.5.1: NSSL-WRF model's MCS forecast locations compared to the NAM model's MCS forecast locations relative to the observed MCS locations using the MODE tool for the same subset.

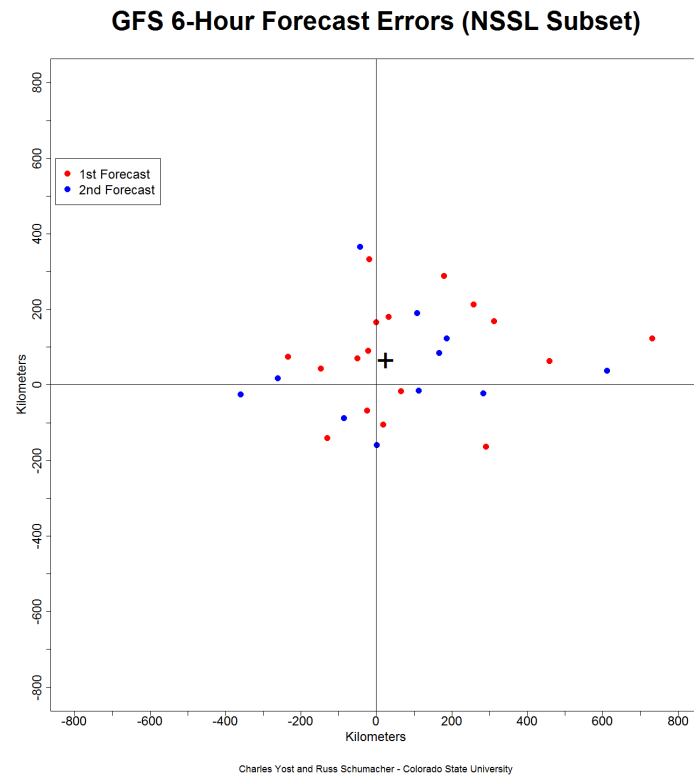
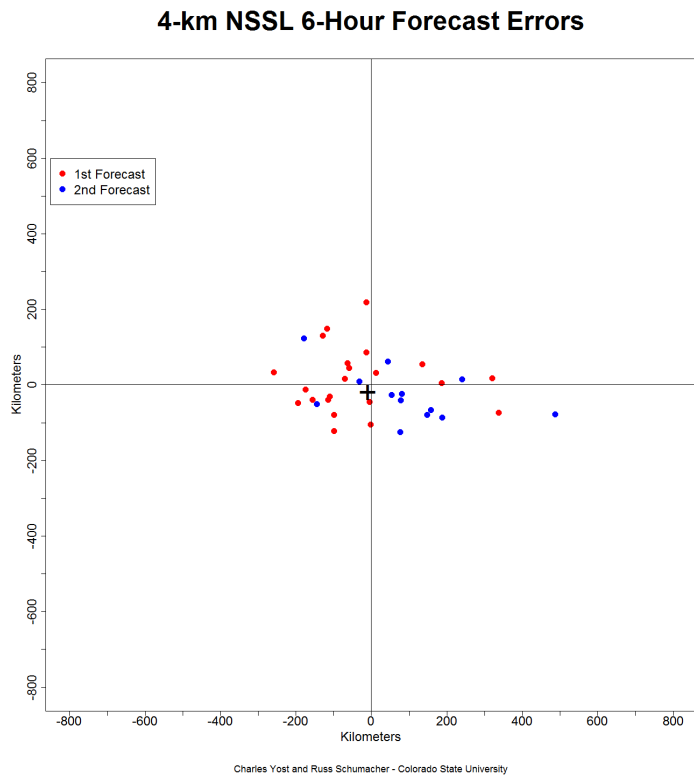


Figure 4.5.2: NSSL-WRF model's MCS forecast locations compared to the GFS model's MCS forecast locations relative to the observed MCS locations using the MODE tool for the same subset.

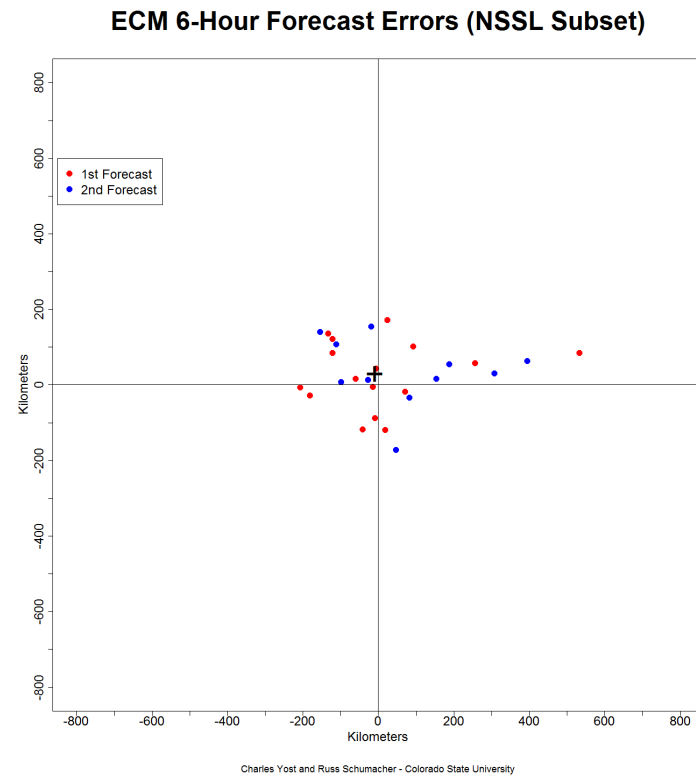
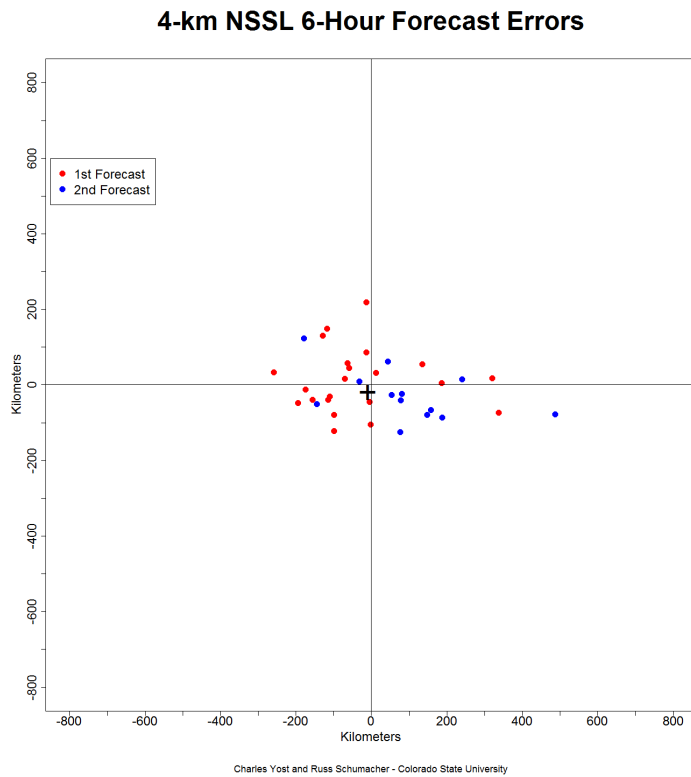


Figure 4.5.3: NSSL-WRF model's MCS forecast locations compared to the ECM model's MCS forecast locations relative to the observed MCS locations using the MODE tool for the same subset.

4.6 Regional Forecast Locations

In order to investigate whether a regional bias exists in the operational models in association with their northern bias, the following figures (4.6.1-4.6.3) are presented. The circles are plotted at each observed object's location that had a northern forecast. The size of the circle is the forecasted object's distance from that observed object. Although not a lot can be gleaned from these maps with so few points, a few interesting things are noted, with the expectation to investigate further in the future. There appear to be 2 regions that favor larger displacement errors in the GFS model's regional bias analysis shown in Figure 4.6.1. The first region is possibly hinted at from southeast Nebraska into central and eastern Iowa with numerous large circles, denoting larger forecast displacement. The other region in southern Arkansas and northern Louisiana has a multitude of MCS forecast displacement errors that are more numerous and larger than forecasted northern objects in southern Missouri and northern Arkansas. No real results can be interpreted from the NAM and ECM models' regional bias analysis, except the overall low displacement errors in the ECM model across the entire nation (Fig. 4.6.2 and Fig. 4.6.3).

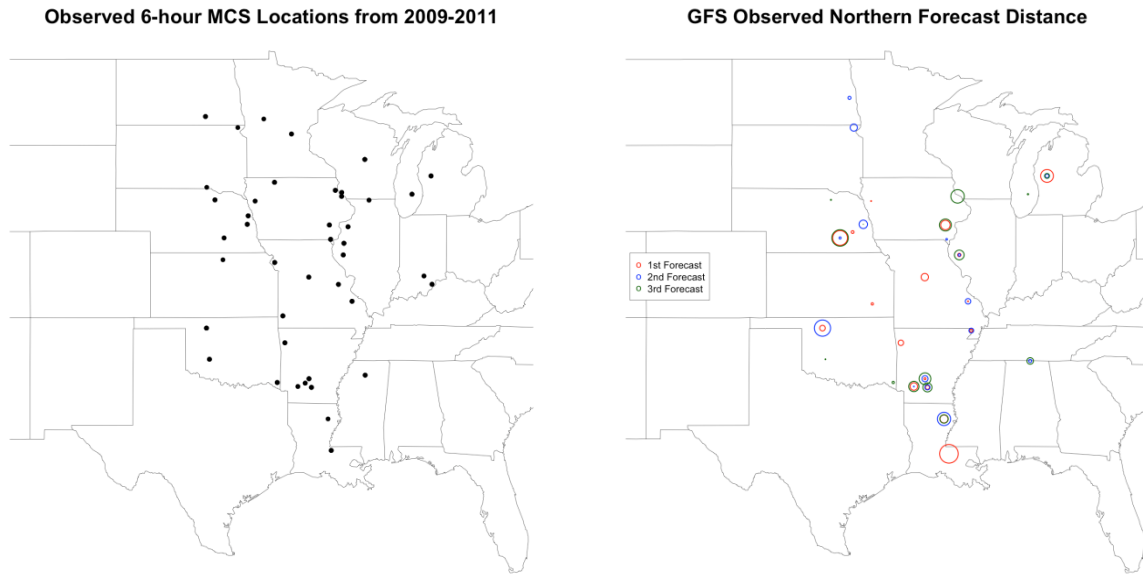


Figure 4.6.1: GFS model’s regional bias analysis showing the observed object locations that had a northern forecast and the size of the circle indicating the distance (northward) to the forecasted object.

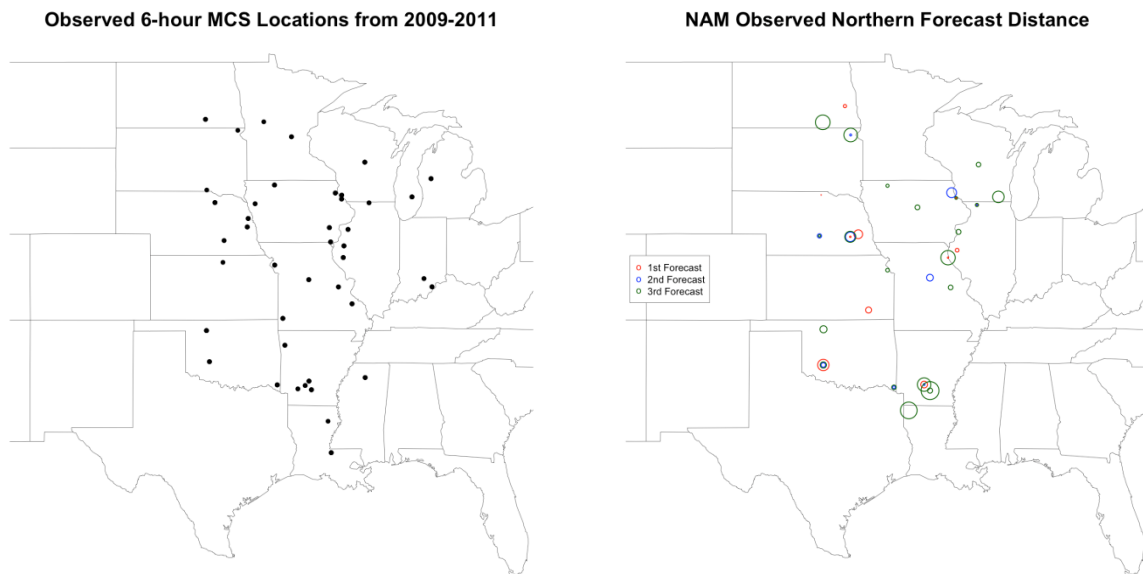


Figure 4.6.2: NAM model’s regional bias analysis showing the observed object locations that had a northern forecast and the size of the circle indicating the distance (northward) to the forecasted object.

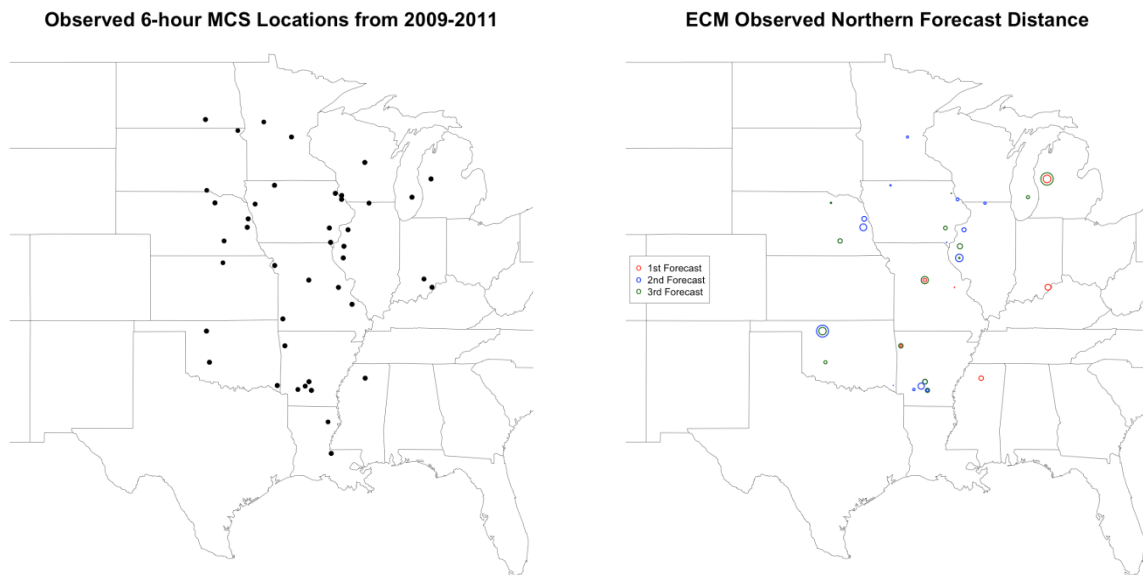
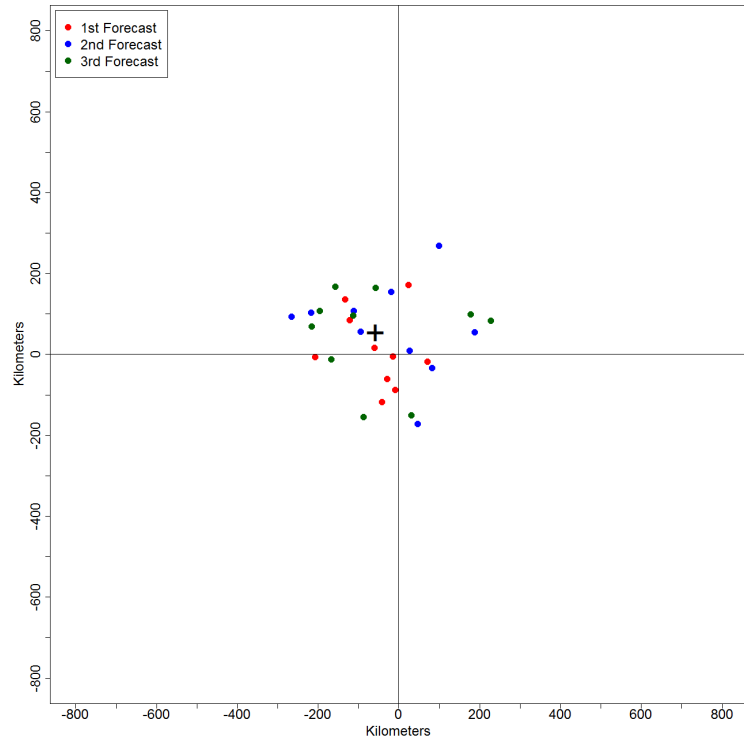


Figure 4.6.2: ECM model's regional bias analysis showing the observed object locations that had a northern forecast and the size of the circle indicating the distance (northward) to the forecasted object.

4.7 Model Upgrades

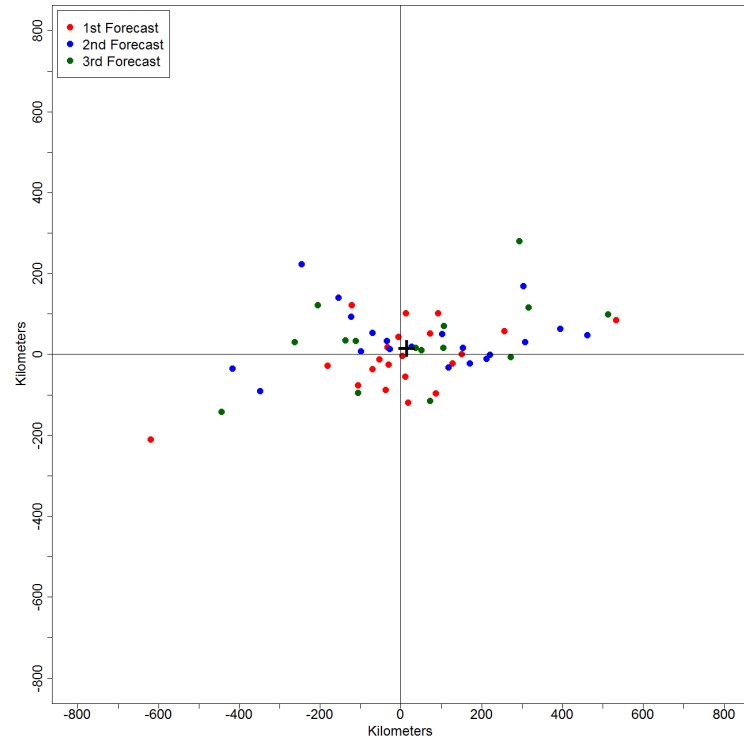
The ECM and the GFS models went through two major upgrades during the study period on 26 January 2010 and 27 July 2010, respectively. The following figures compare their displacement errors before and after each model upgrade. The ECM model noticed a considerable elongation east/west of forecast locations after the upgrade, with a slight decrease poleward of forecast locations. The GFS model's upgrade was over halfway through the warm season in 2010, yielding a small number of points to evaluate after the model upgrade. The lack of a northern bias is noticeable, yet subtleties of a western bias is noted, although, again, involves a very small sample size.

ECM 6-Hour Forecast Errors (Forecasts 1-3 Before Upgrade)



Charles Yost and Russ Schumacher - Colorado State University

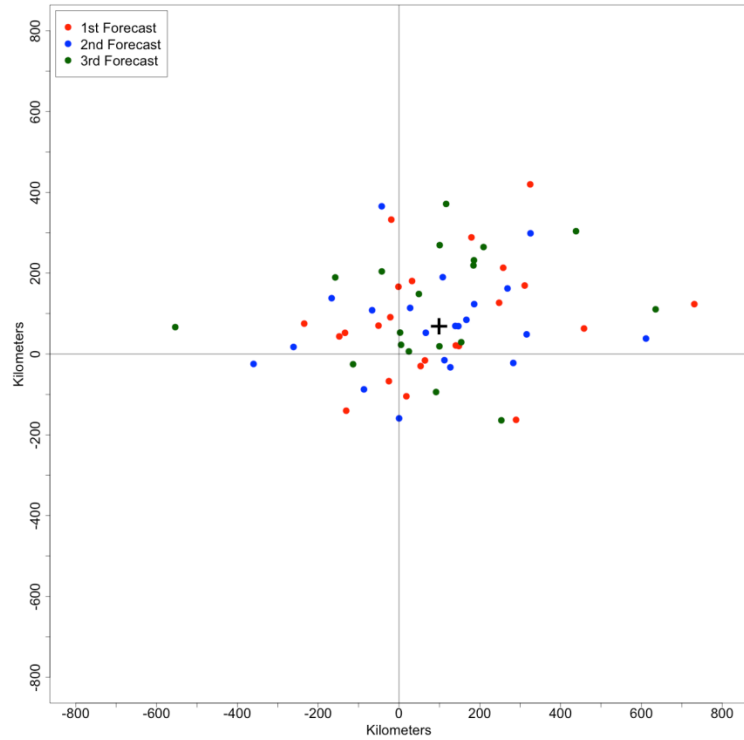
ECM 6-Hour Forecast Errors (Forecasts 1-3 After Upgrade)



Charles Yost and Russ Schumacher - Colorado State University

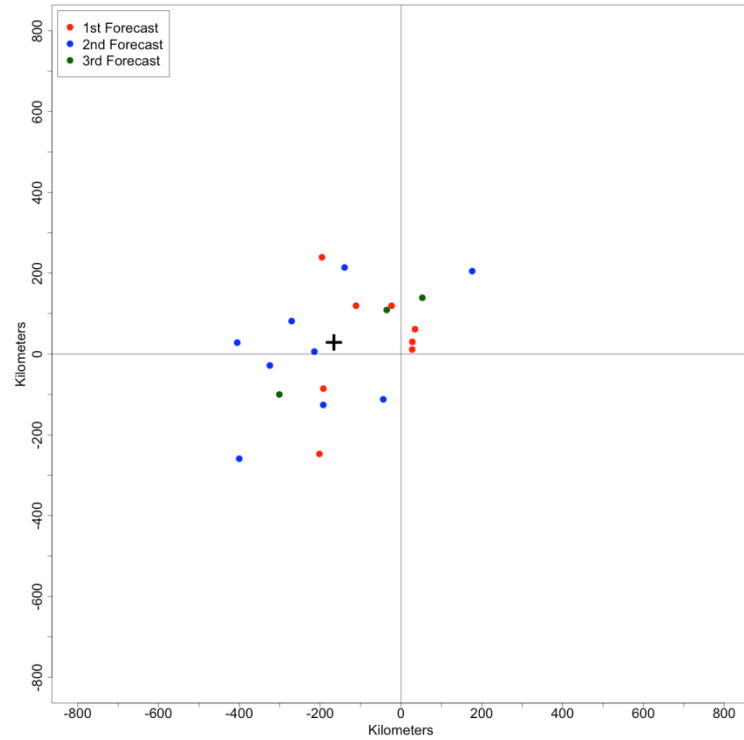
Figure 4.7.1: ECM model's displacement errors before and after the major model upgrade on 26 January 2010.

GFS 6-Hour Forecast Errors (Forecasts 1-3 Before Upgrade)



Charles Yost and Russ Schumacher - Colorado State University

GFS 6-Hour Forecast Errors (Forecasts 1-3 After Upgrade)



Charles Yost and Russ Schumacher - Colorado State University

Figure 4.7.2: GFS model's displacement errors before and after the major model upgrade on 27 July 2010.

4.8 Manual Verification Results

As shown in Fig. 4.8.1, the GFS forecasts from the manual analysis were generally located too far to the north of the observed objects, as well as too far to the east. These results and overall shape are consistent with what the MODE tool discovered in its objective analysis. In Fig. 4.8.2, the NAM forecasts are predominantly located to the north of the observed objects, but with no temporal bias as an east or west trend, again matching with the MODE tool analysis.

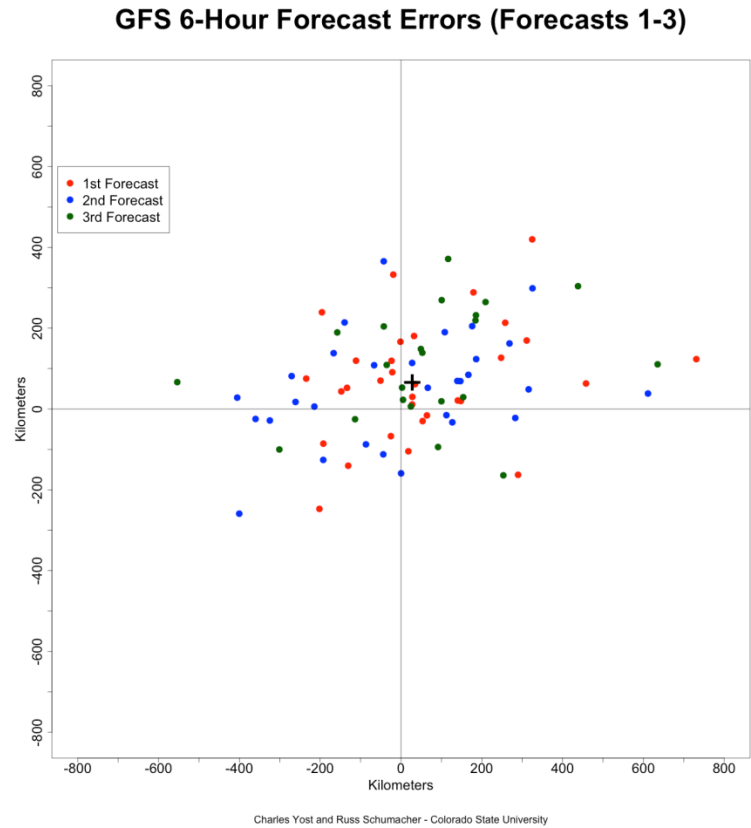
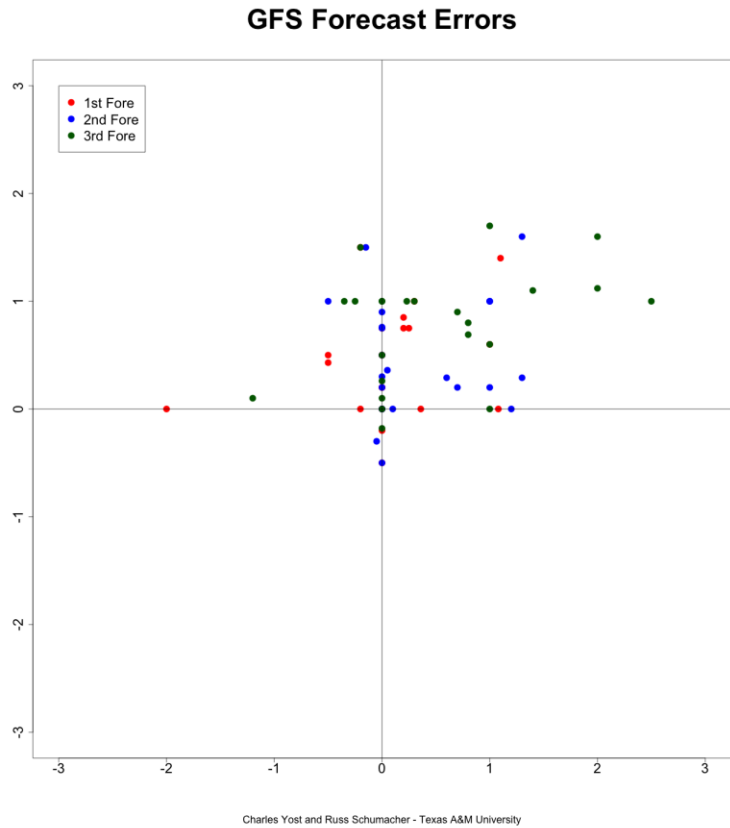


Figure 4.8.1: GFS model's displacement errors from the manual analysis (left figure) compared to the MODE tool analysis (right figure).

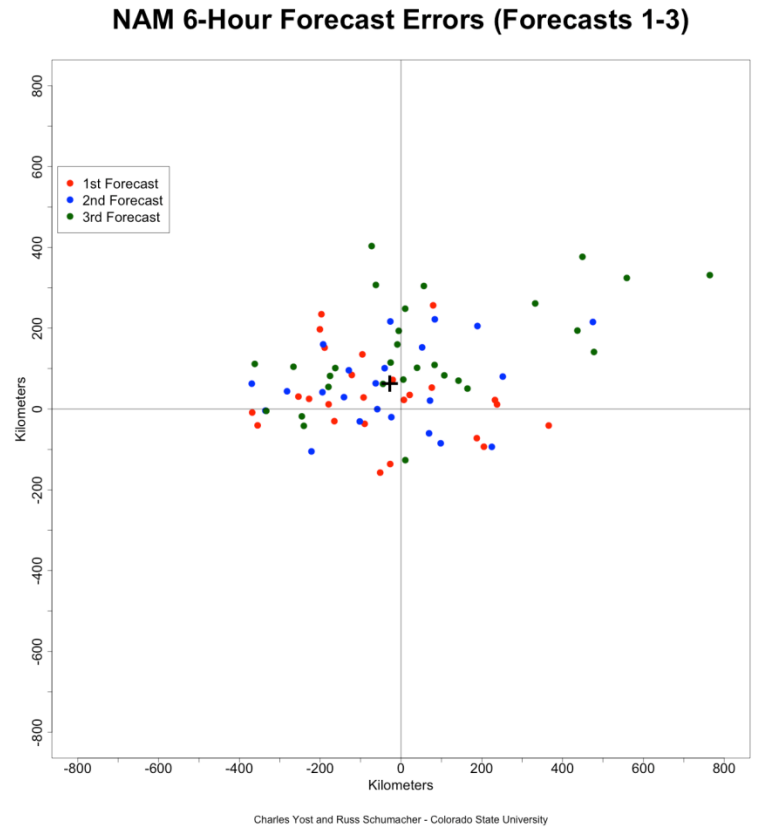
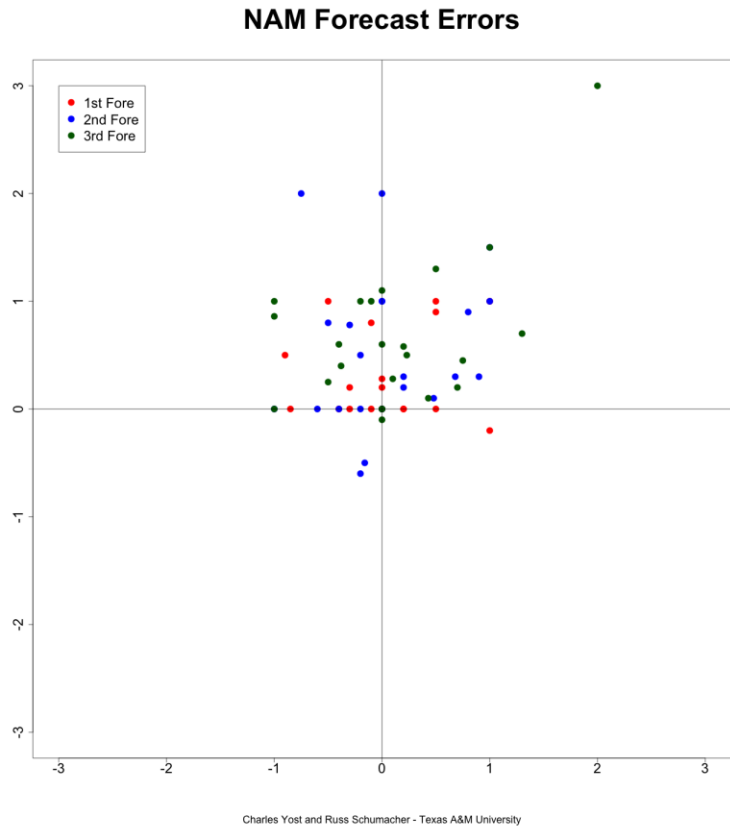


Figure 4.8.2: NAM model's displacement errors from the manual analysis (left figure) compared to the MODE tool analysis (right figure).

CHAPTER 5

CASE STUDY OF THE 27-28 JULY 2011 MESOSCALE CONVECTIVE SYSTEM

5.1 Background

The Dubuque, IA Mesoscale Convective System (MCS) produced heavy rainfall over a small contiguous area on 27-28 July 2011, shattering several records for most rainfall in Dubuque: on July 27, on July 28, for a single day in July, for a 24-hour period, for July, and for a single month (NWS 2011). Over 50 people had to be rescued by boat from mobile home parks around the area, and the area's Mississippi River floodgates had to be closed because of the excessive rain. Rain was caused by an MCS that produced over 304 mm, or 12 inches, of rain over a 24-hour period (Fig. 5.1.1). Over a 24 hour period ending at 1400 UTC, the Dubuque airport recorded 261 mm (10.31 in.) and a cooperative observer in Galena, IL measured 341 mm (13.45 in.). A hydrograph of the Mississippi River in Dubuque, IA which displays the flood stage and the flow rate, shows a 4 foot rise in river height in a 12 hours (Fig. 5.1.2).

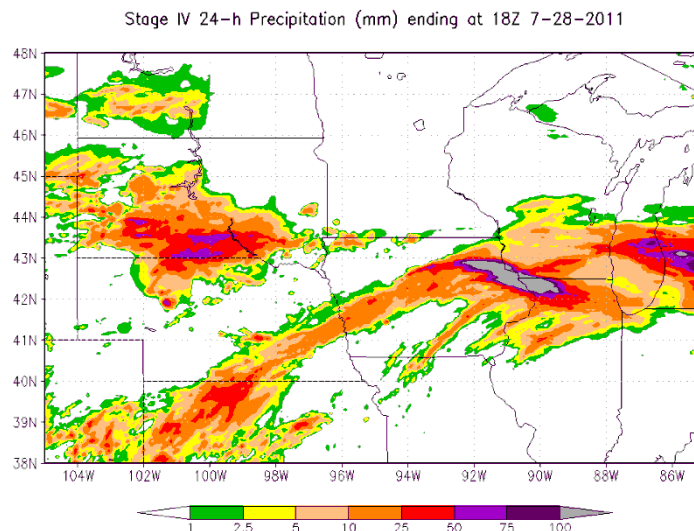


Figure 5.1.1: Stage IV 24-hour precipitation ending on 1800 UTC 28 July 2011.

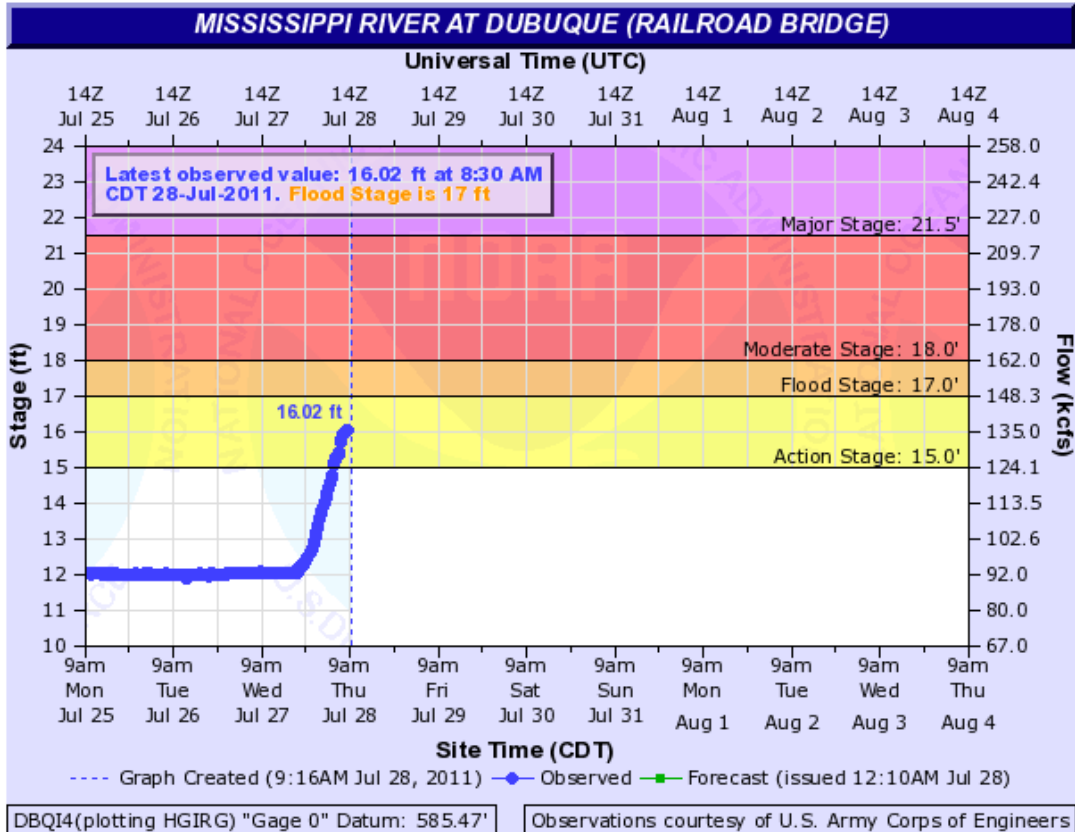


Figure 5.1.2: Hydrograph of the Mississippi River at Dubuque, IA (Online at http://www.crh.noaa.gov/dvn/?n=event_072711_dubuqueflashflood).

5.2 Pre-Event Environmental Setup

The origin of this devastating MCS begins on the 26th of July with a line of convection draped from the Dakotas' joint border southward into northeast Colorado with strong individual convective cells located throughout the line (Fig. 5.2.1). The convection in the north outruns the line in the early morning hours, while an MCV spins up in the southern portion of the line, and begins to track northeastward through Nebraska. A pressure trough extends from the surface low in Kansas and is indicated on the HPC surface analysis in Figure 5.2.2, with the boundary draped from a surface low in North Dakota down into southern Kansas. This outflow boundary will be key in the initiation of convection for this MCS. Around 1200 UTC, the MCV matures and

continues to push northeastward, as convection associated with a warm front in the Minnesota/Wisconsin region begins to orient itself into a brief leading stratiform linear MCS (Fig. 5.2.3). A strong low-level jet at 850hPa intersects this warm front and brings in warm air (Fig. 5.2.4 and 5.2.5). An upper-air sounding from Topeka, KS shows this low-level jet advecting warm air with moderate moisture (Fig. 5.2.6). The linear MCS starts to dissipate shortly after this and moves out of the area by 1700 UTC, leaving the area devoid of convection until the start of the primary rain event. Starting at 1800 UTC, the warm front from the Minnesota/Wisconsin region pushes south and orients the entire line into a southeast to northwest pattern intersecting the stationary front right at the Iowa-Wisconsin-Illinois border (Fig. 5.2.7). At 1800 UTC, the low-level jet is oriented parallel to the outflow boundary that is positioned from mid-Iowa southwestward into Kansas, with the northern edge of the wind-speed maximum placed right at the intersection of the outflow boundary and stationary front (Fig. 5.2.9). Right before convection initiates at 0000 UTC, the Davenport, IA upper-air sounding, which is located about 115 km to the south of Dubuque, shows a warm and moist lower level, and a favorable environmental temperature profile, allowing for a large amount (4100 J kg^{-1}) of convective available potential energy (CAPE) (Fig. 5.2.11). Very warm air is being advected into the region by the low-level jet, with the main axis of strong wind perpendicular to the intersection of the two boundaries (Fig. 5.2.10). This intersection of the stationary front and outflow boundary, which will soon be analyzed as a stationary front (Fig. 5.2.8), will be the axis for the heaviest precipitation during the event. How the models resolve this warm front and subsequent stationary front will prove pivotal in the location of the MCS.

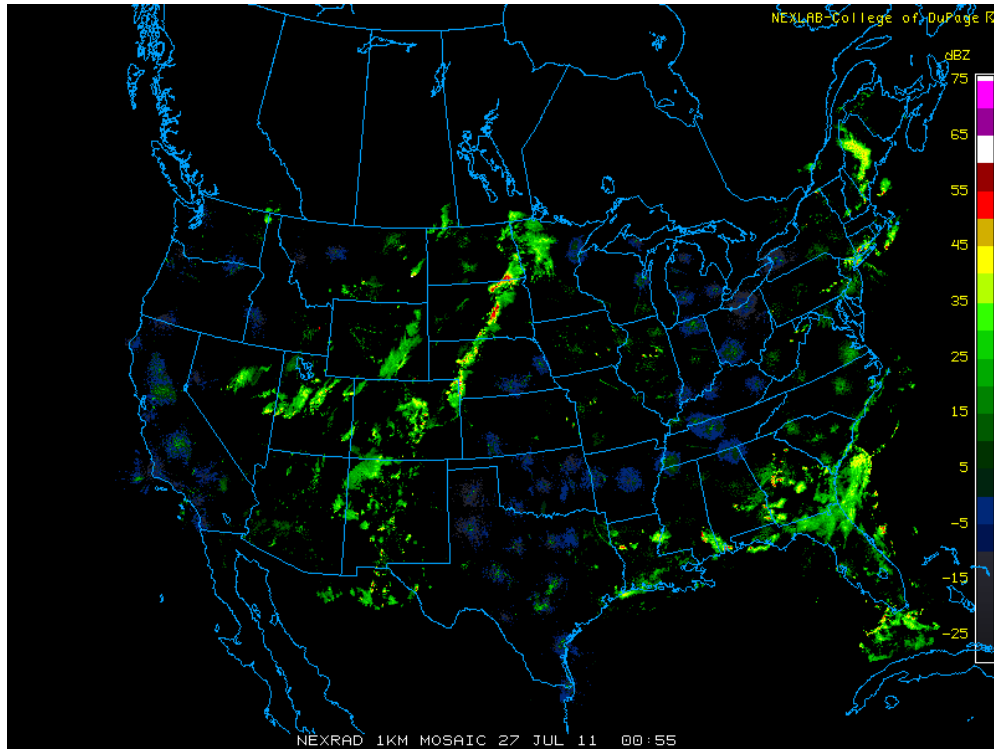


Figure 5.2.1: NEXRAD 1 KM Mosaic for 0100 UTC 27 July 2011.

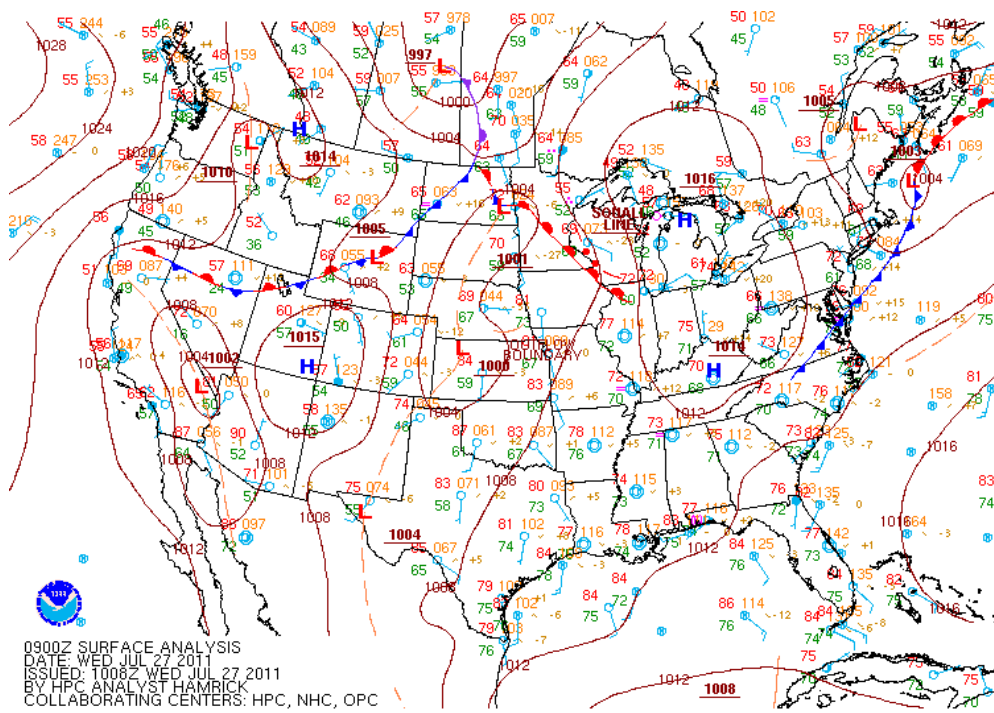


Figure 5.2.2: HPC surface analysis for 0900 UTC 27 July 2011.

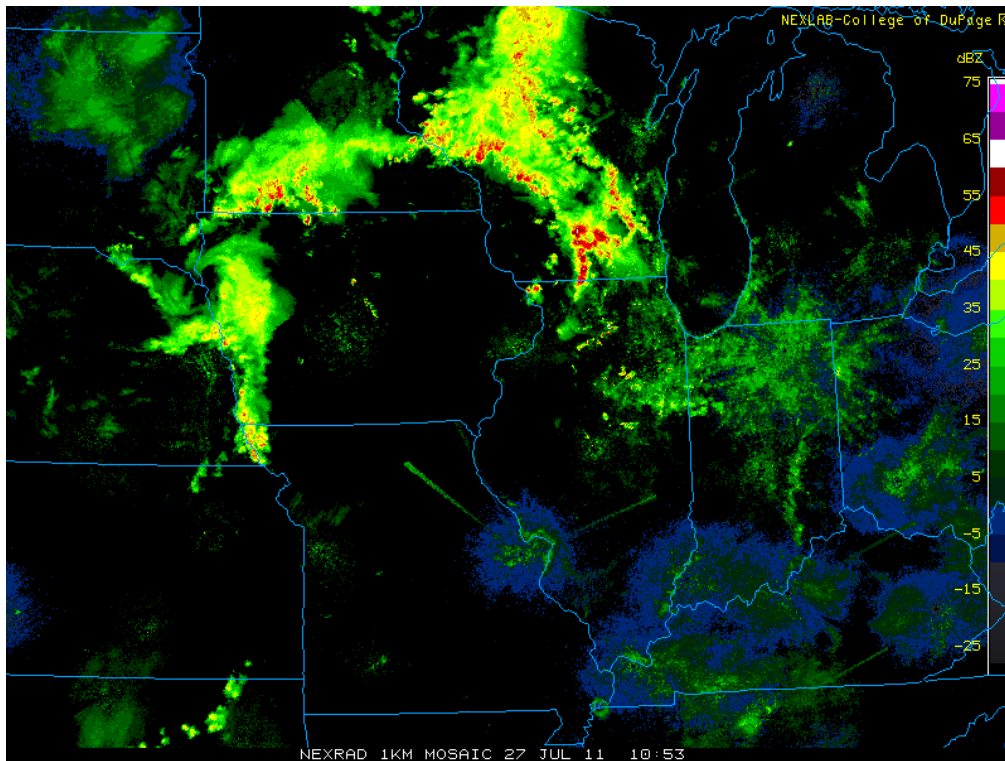


Figure 5.2.3: NEXRAD 1 KM Mosaic for 27 July 2011 at 11 UTC.

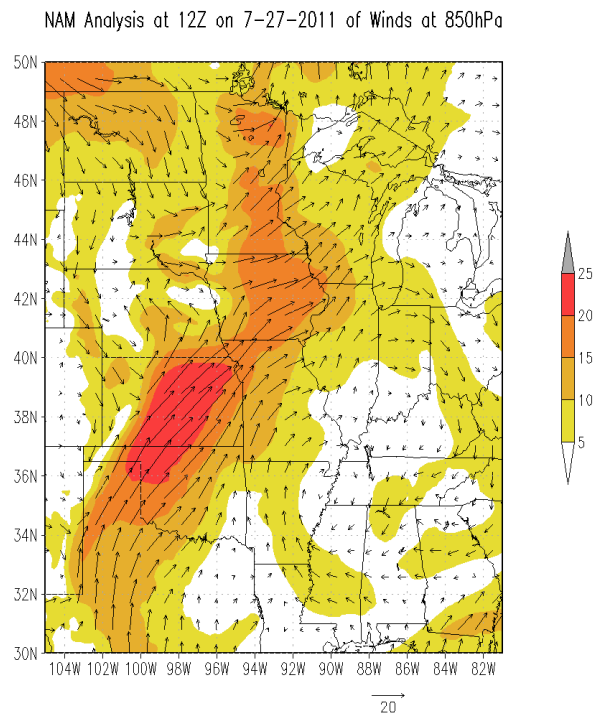


Figure 5.2.4: NAM analysis at 1200 UTC on 27 July 2011 of winds in knots at 850 hPa with the magnitude of the winds shaded.

NAM Analysis at 12Z on 7-27-2011 of Theta and Winds at 850hPa

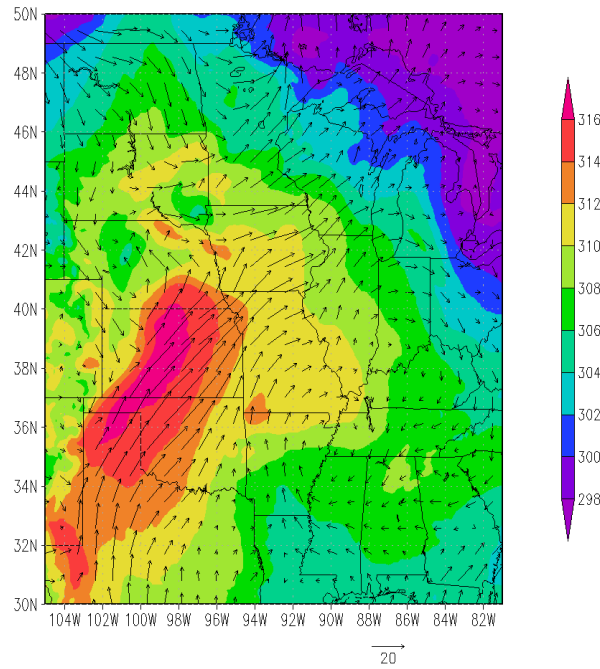
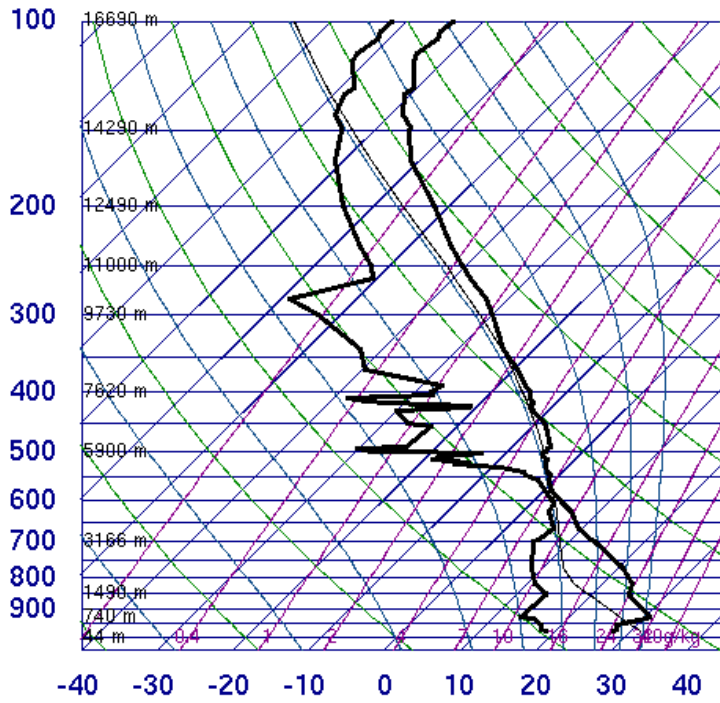


Figure 5.2.5: NAM analysis at 1200 UTC on 27 July 2011 of potential temperature (Kelvin) and winds in knots at 850 hPa.

72456 TOP Topeka



SLAT	39.07
SLON	-95.62
SELV	270.0
SHOW	-1.38
LIFT	0.21
LFTV	-0.48
SWET	258.6
KINX	35.50
CTOT	18.70
VTOT	29.70
TOTL	48.40
CAPE	6.33
CAPV	21.30
CINS	-606.
CINV	-572.
EQLV	501.6
EQTV	421.8
LFCT	582.6
LFCV	584.1
BRCH	0.15
BRCV	0.50
LCLT	286.8
LCLP	794.0
MLTH	306.4
MLMR	12.61
THCK	5856.
PWAT	44.70

12Z 27 Jul 2011

University of Wyoming

Figure 5.2.6: Upper-air sounding from Topeka, KS at 1200 UTC on 27 July 2011.

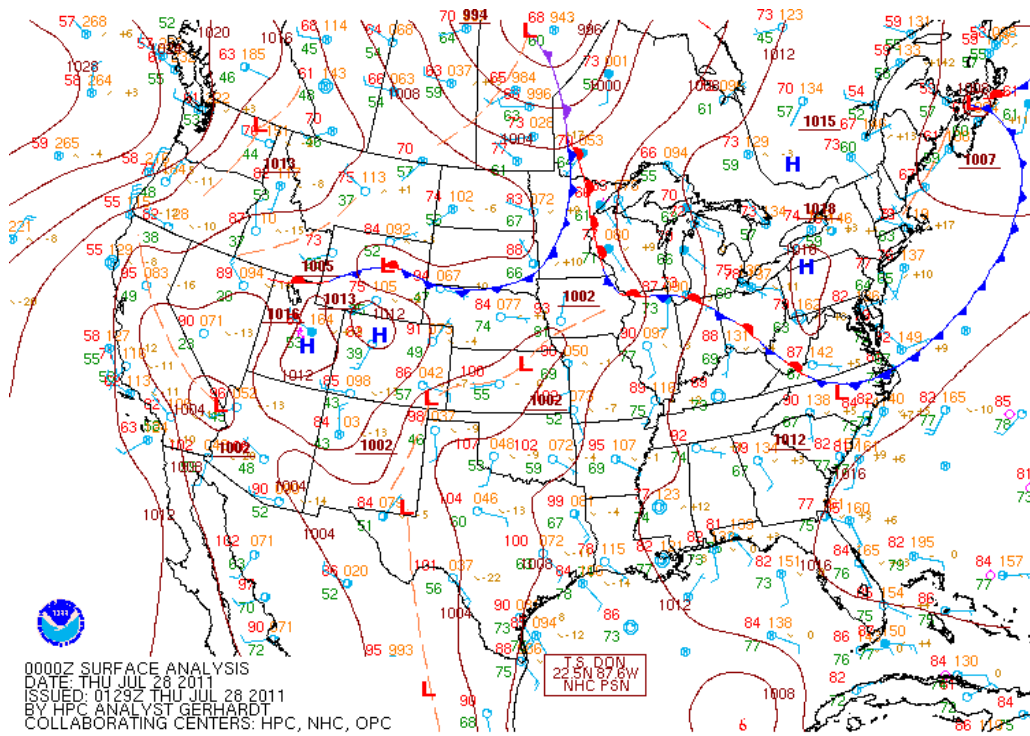


Figure 5.2.7: HPC surface analysis for 00 UTC on 28 July 2011.

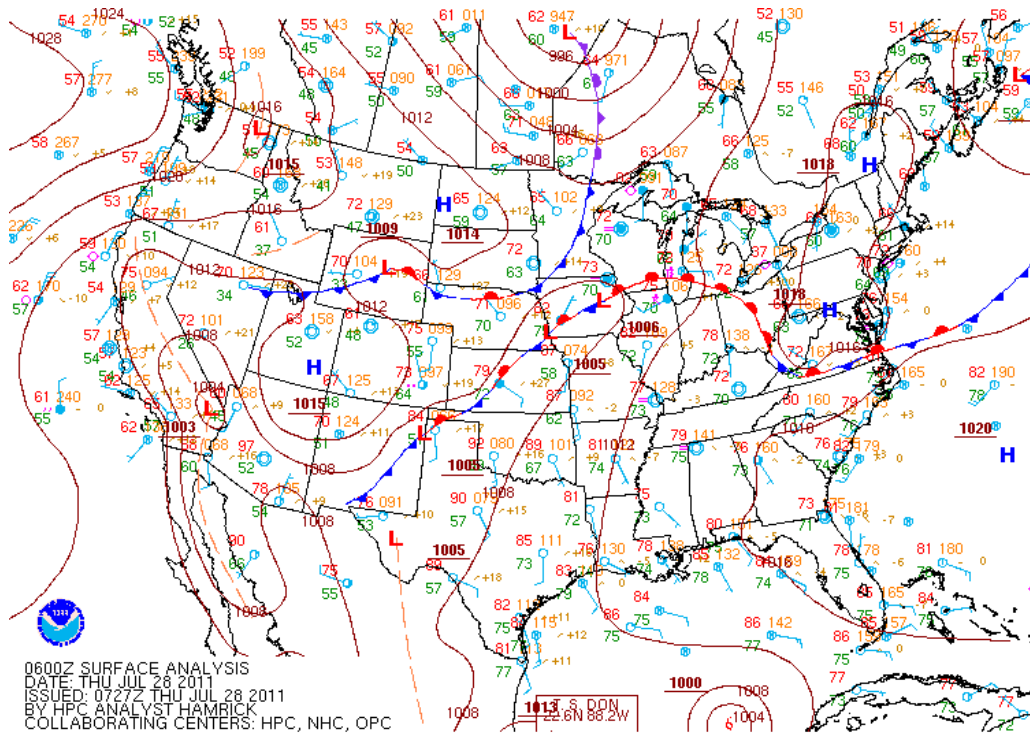


Figure 5.2.8: HPC surface analysis for 6 UTC on 28 July 2011.

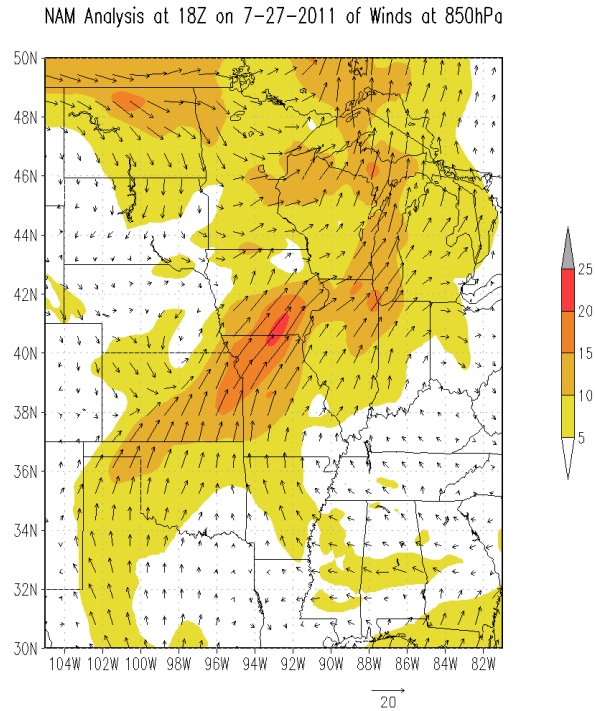


Figure 5.2.9: NAM analysis at 1800 UTC on 27 July 2011 of winds in knots at 850 hPa with the magnitude of the winds shaded.

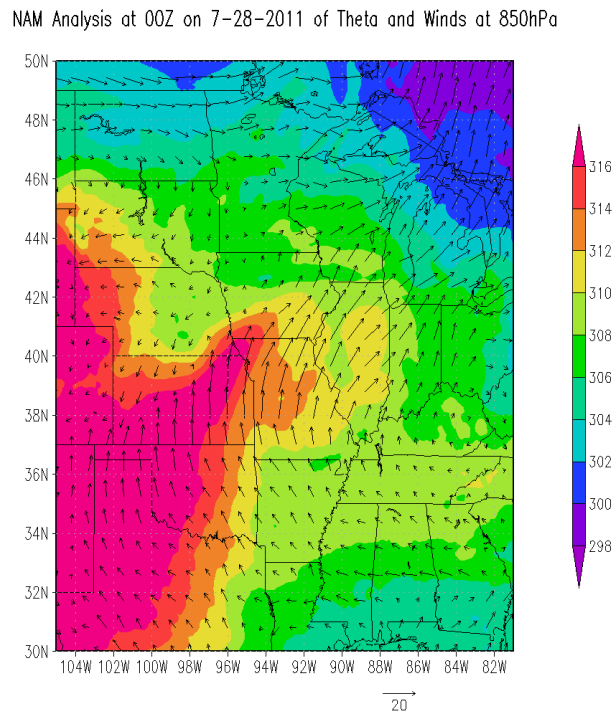


Figure 5.2.10: NAM analysis at 0000 UTC on 28 July 2011 of potential temperature (Kelvin) and winds (knots) at 850 hPa.

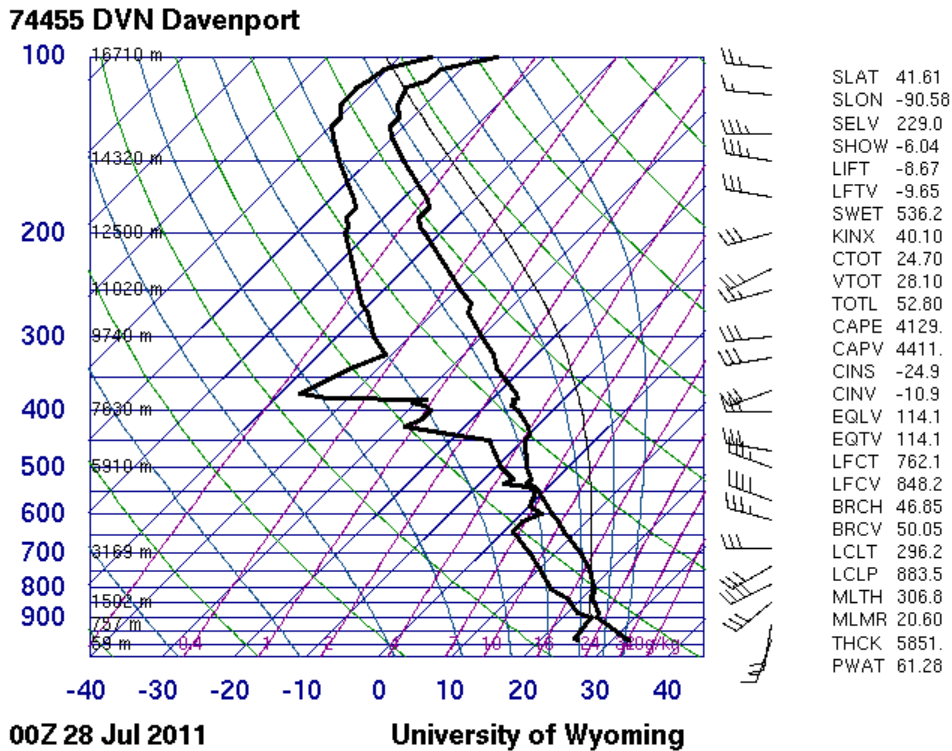


Figure 5.2.11: Upper-air sounding from Davenport, IA at 0000 UTC on 28 July 2011.

5.3 Primary Rain Event

The main convection of the event initiates at 2300 UTC on July 27 around the Iowa-Illinois-Wisconsin border. Convection rapidly intensifies and attains linear organization along the Wisconsin-Illinois border over the next 2.5 hours, and a cold pool associated with this convection begins to push south (Fig. 5.3.1). This initial convection forms on the north side of the stationary front previously noted. Around 0400 UTC, this line of initial convection in Illinois moves south with the cold pool, as new cells form upstream in Iowa and continue to train over the tri-state area (Fig. 5.3.2). The cold pool outruns the southern convection in Illinois and is swept away to the east. New convective cells continue to form upstream into Iowa and train over the Wisconsin-Illinois border. An area of stratiform precipitation begins to form to the northeast of the line at 0900 UTC, as the whole system persists in the same location (Fig. 5.3.3). The main

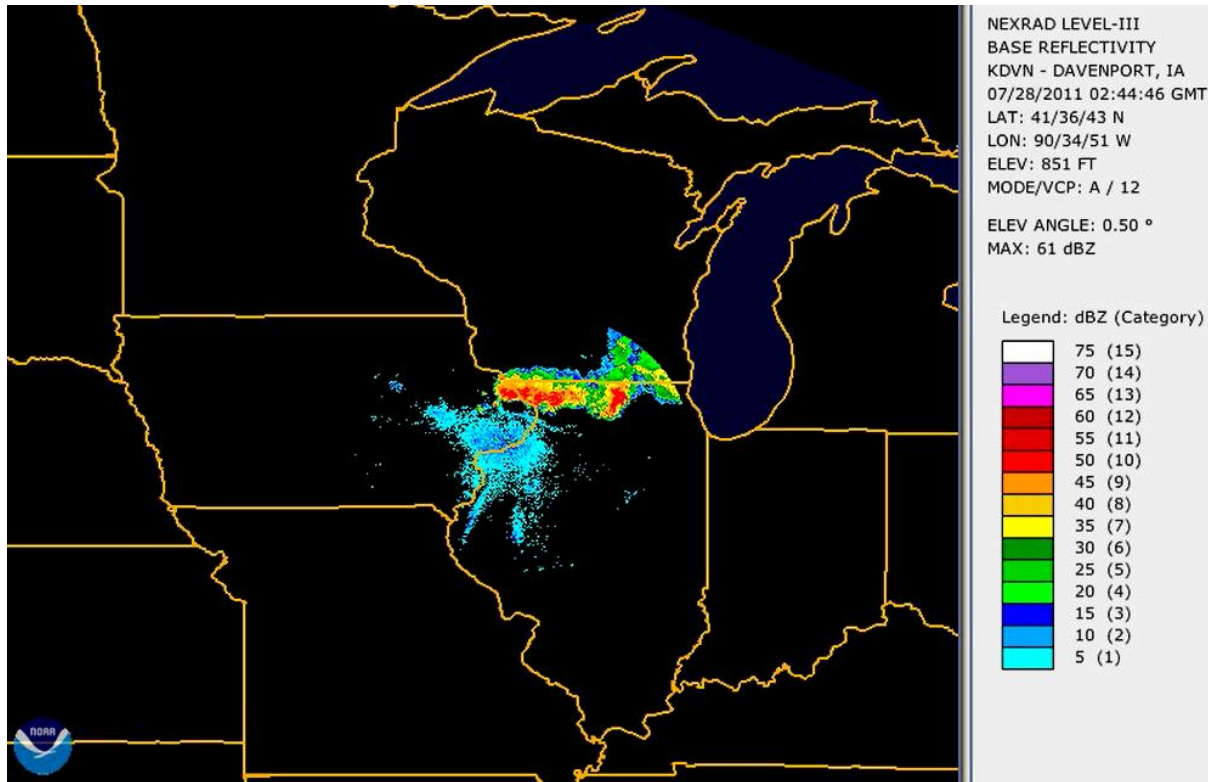


Figure 5.3.1: Radar from Davenport, IA at 0244 UTC on 28 July 2011.

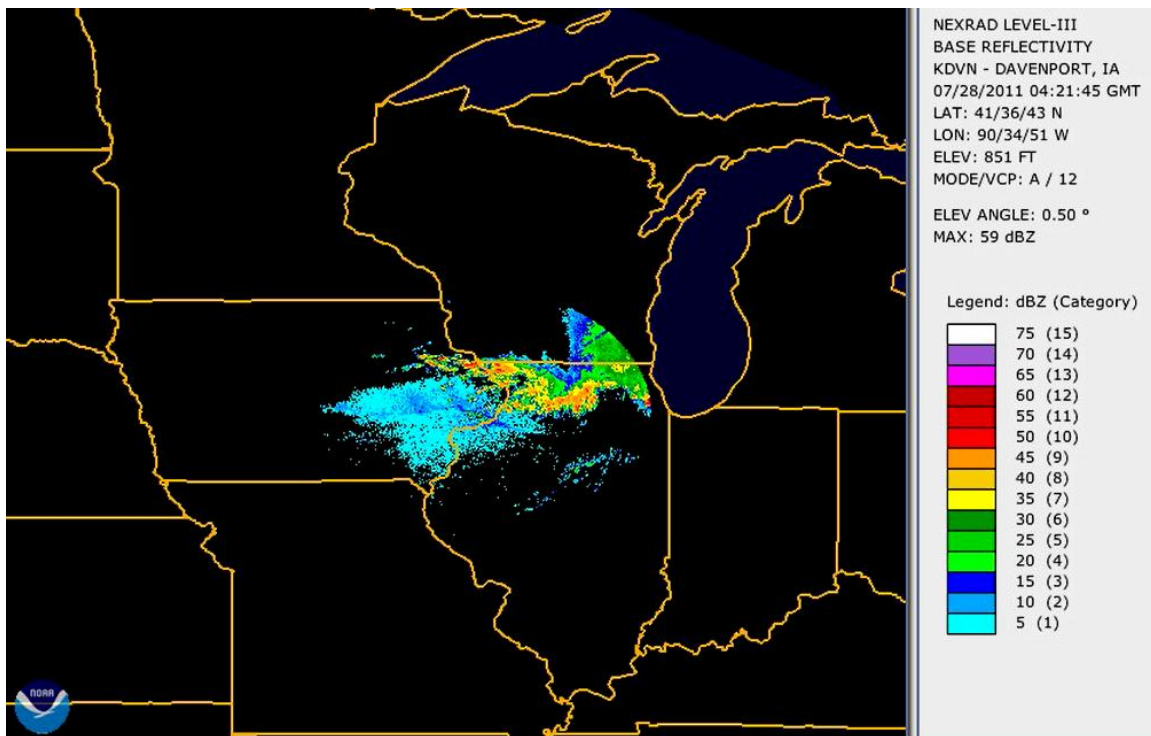


Figure 5.3.2: Radar from Davenport, IA at 0421 UTC on 28 July 2011.

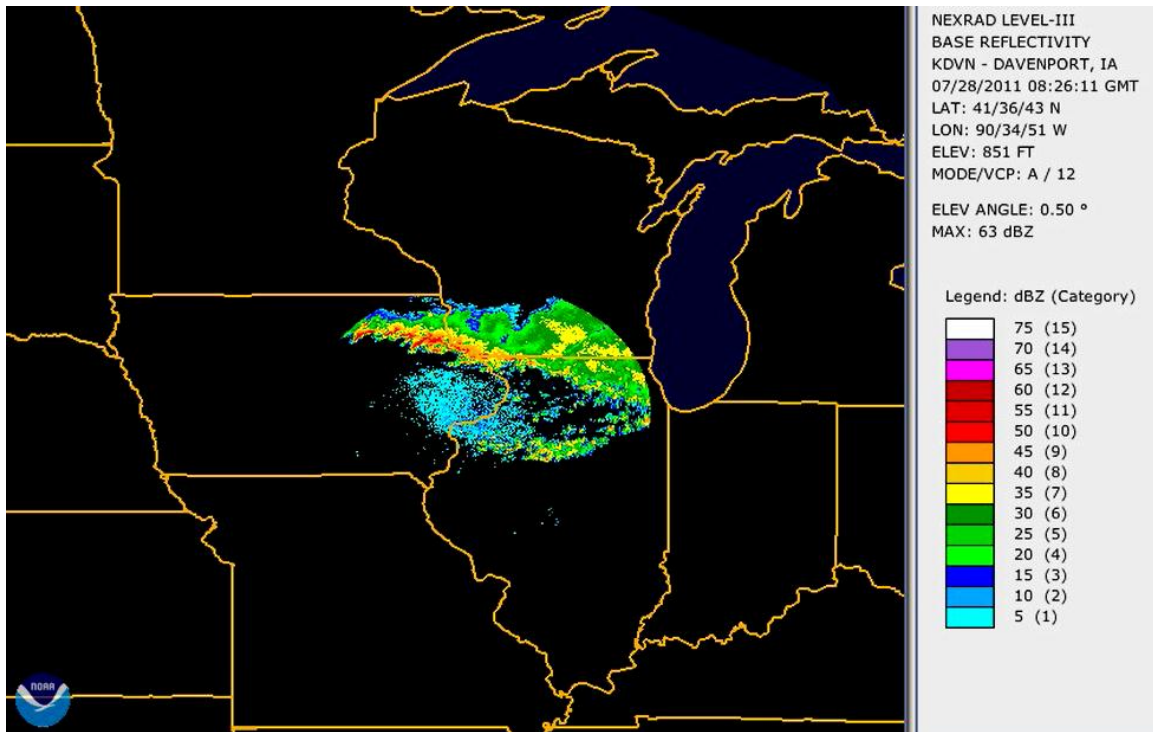


Figure 5.3.3: Radar from Davenport, IA at 0826 UTC on 28 July 2011.

5.4 Evaluation of the Models' Forecasts

In order to judge how each model's forecast did for this case, the models' forecasted precipitation from 0600 UTC to 1200 UTC on 28 July 2011 is plotted in figures 5.4.1 and 5.4.2. The locations of the resolved objects from the MODE tool for both 6 hour periods of the rain event is plotted in figure 5.4.3 as well.

Starting 3 days out, the NAM model correctly forecasted a (drier) precipitation maximum over the tri-state area, but continued to dry it out further with the 5th forecasts (Fig. 5.4.1 and 5.4.2). The fourth forecast places the precipitation maximum farther south and east of the observed maximum. The 2nd and 3rd forecasts generally saw a placement north and east, respectively, from the observed. The most recent forecasts correctly predicted the location of the MCS for these time periods with an incorrect axis angle. Curious to note about the NAM model's forecasts for this case, as indicated on Fig. 5.4.3, is the overall better performance of the

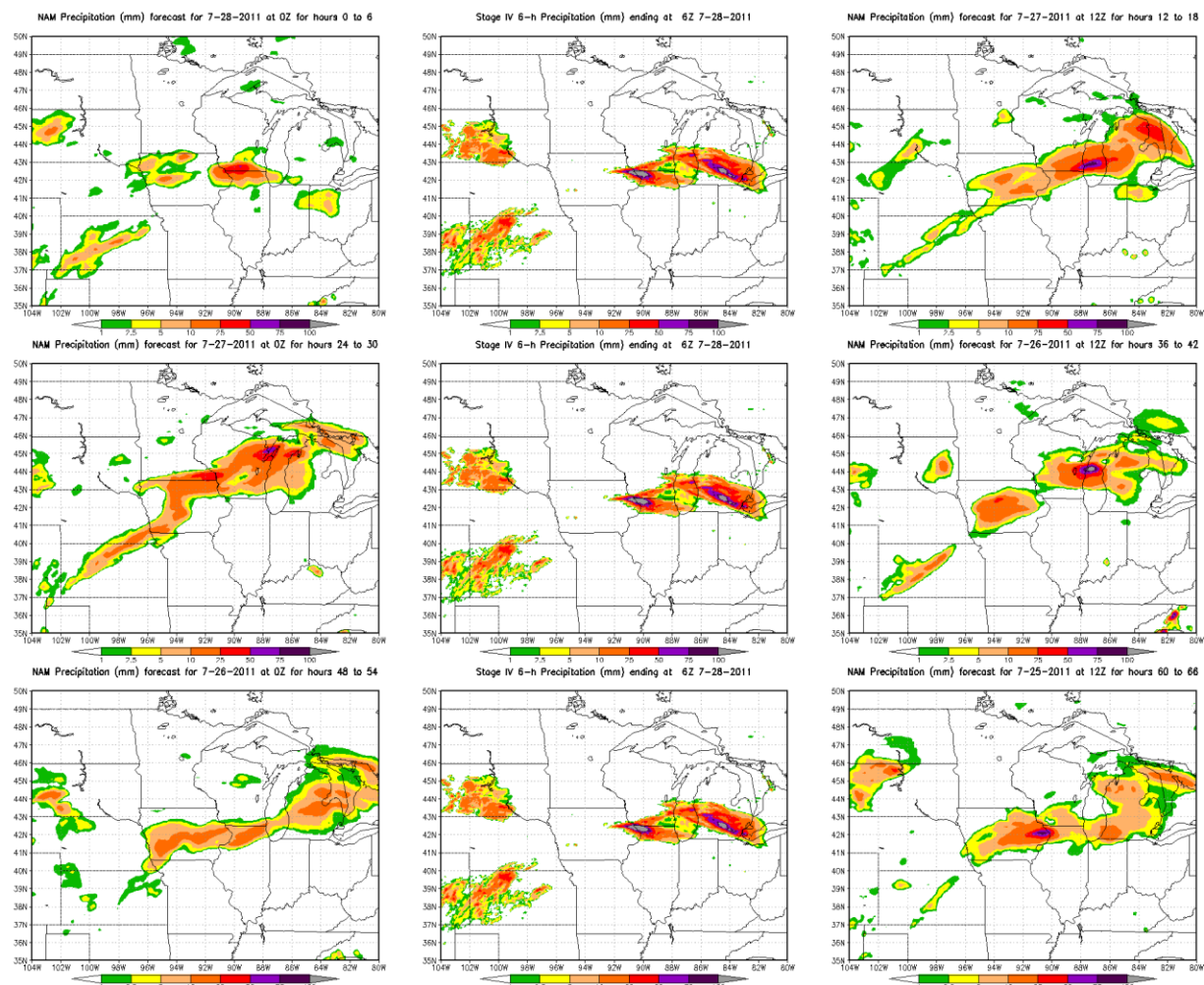


Figure 5.4.1: The NAM model’s 6 forecasts and corresponding Stage IV precipitation valid for 28 July 2011 0000 to 0600 UTC. The Stage IV observed precipitation valid for the same time is plotted in the center column, with the 1st forecast in the upper right map, 2nd in the upper left, 3rd in the middle left, etc.

location at the later forecast times. While intensity was not correctly forecasted, the longer lead times forecasts did consistently forecast the precipitation maximum very close to the observed location. As mentioned previously, the forecasts to the north had a larger spread and were generally more inaccurate than the later forecasts. The third forecast will be examined closer in the next section to isolate possible causes of that northern forecast and its applicability to the northern bias in other cases.

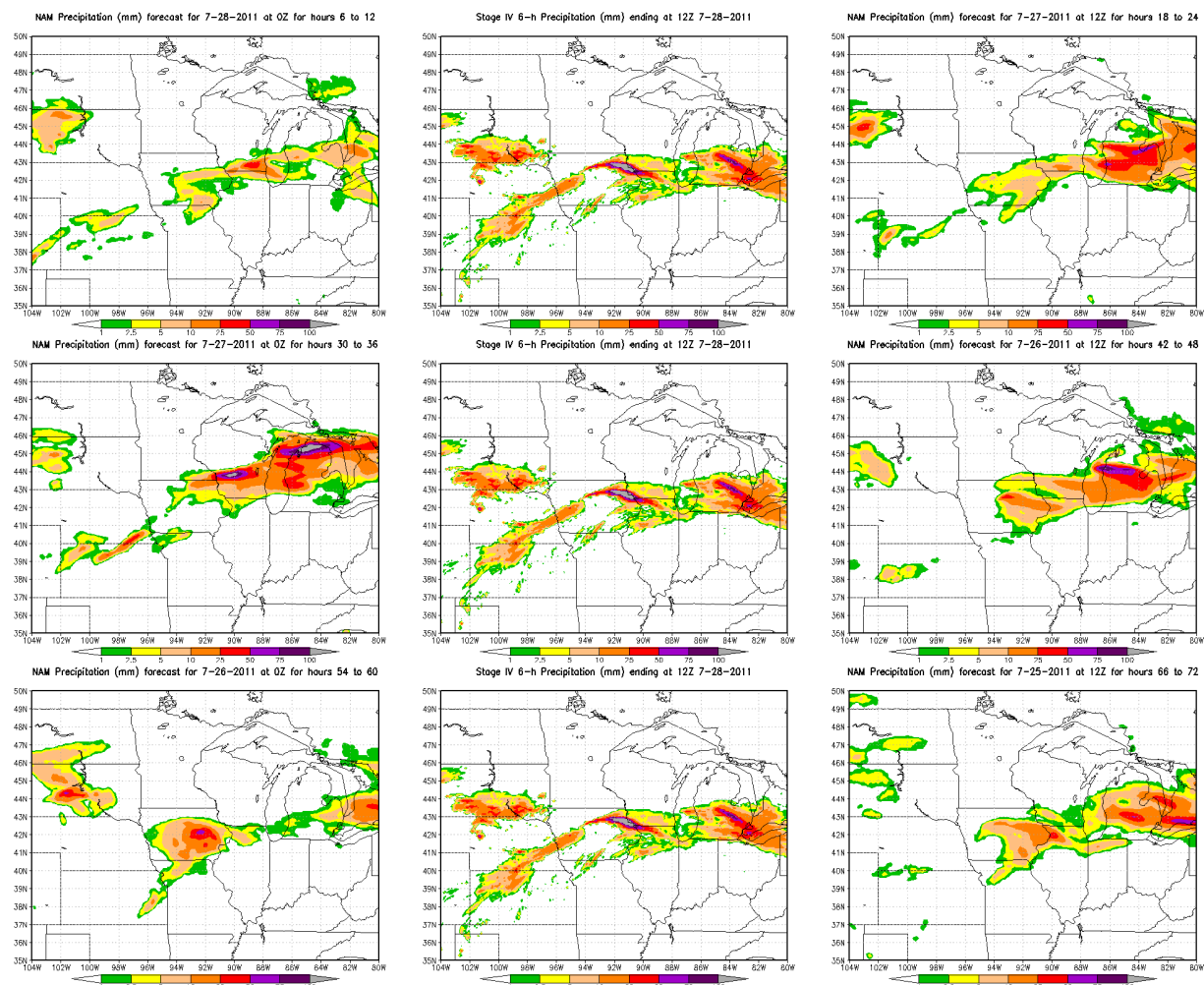


Figure 5.4.2: The NAM model’s 6 forecasts and corresponding Stage IV precipitation valid for 28 July 2011 0600 to 1200 UTC.

For 0000 UTC to 0600 UTC time period, the GFS model forecasts precipitation associated with an MCS around the tri-state area for all lead times except the 4th forecast that has a maximum to the northeast (Fig. 5.4.4). The next six hour interval is generally less accurate with correct forecasts of the MCS in the wrong locations. The few forecasts that do have precipitation in the correct location, fail to place a maximum (Fig. 5.4.5). The MODE tool notes an overall northern bias for this case, with the median y displacement well to the north of the observed location (Fig. 5.4.5).

The ECM model correctly forecasts the location of the event 72 hours out with a broad swath of moderate precipitation slightly to the north of the observed maximum over both 6-hour time intervals (Fig. 5.4.7 and 5.4.7). The next 5 forecasts for both time periods remain in generally the same place with just decreasing lateral spread north and south with each more recent forecast. The MODE tool analysis reflects this finding with almost all of the forecasted objects within 150 kilometers north or south. The greatest variability occurred in forecasting the precipitation maximums east/west extent. The median x displacement shows an overall shift and inaccuracy to the west. The precipitation amounts predicted by the ECM are consistently too low, however.

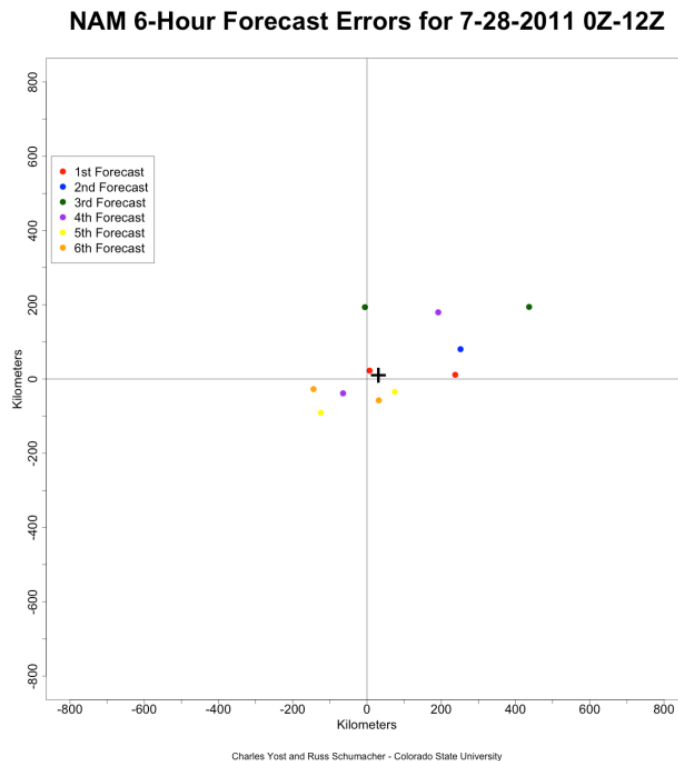


Figure 5.4.3: NAM model’s MCS forecast locations relative to the observed MCS locations using the MODE tool for the two 6 hour periods on 28 July 2011 from 0000 to 1200 UTC.

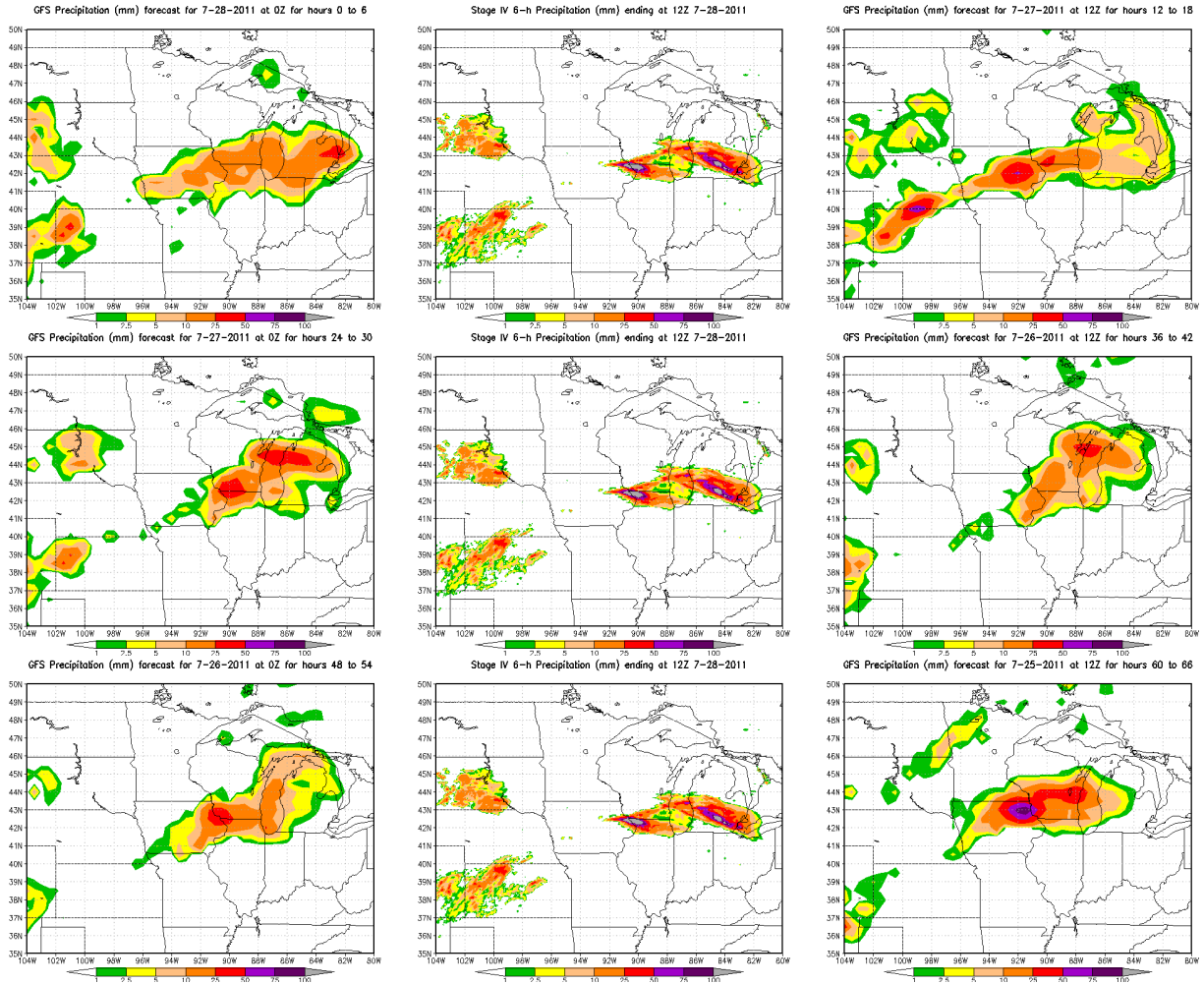


Figure 5.4.4: The GFS model's 6 forecasts and corresponding Stage IV precipitation valid for 28 July 2011 0000 to 0600 UTC.

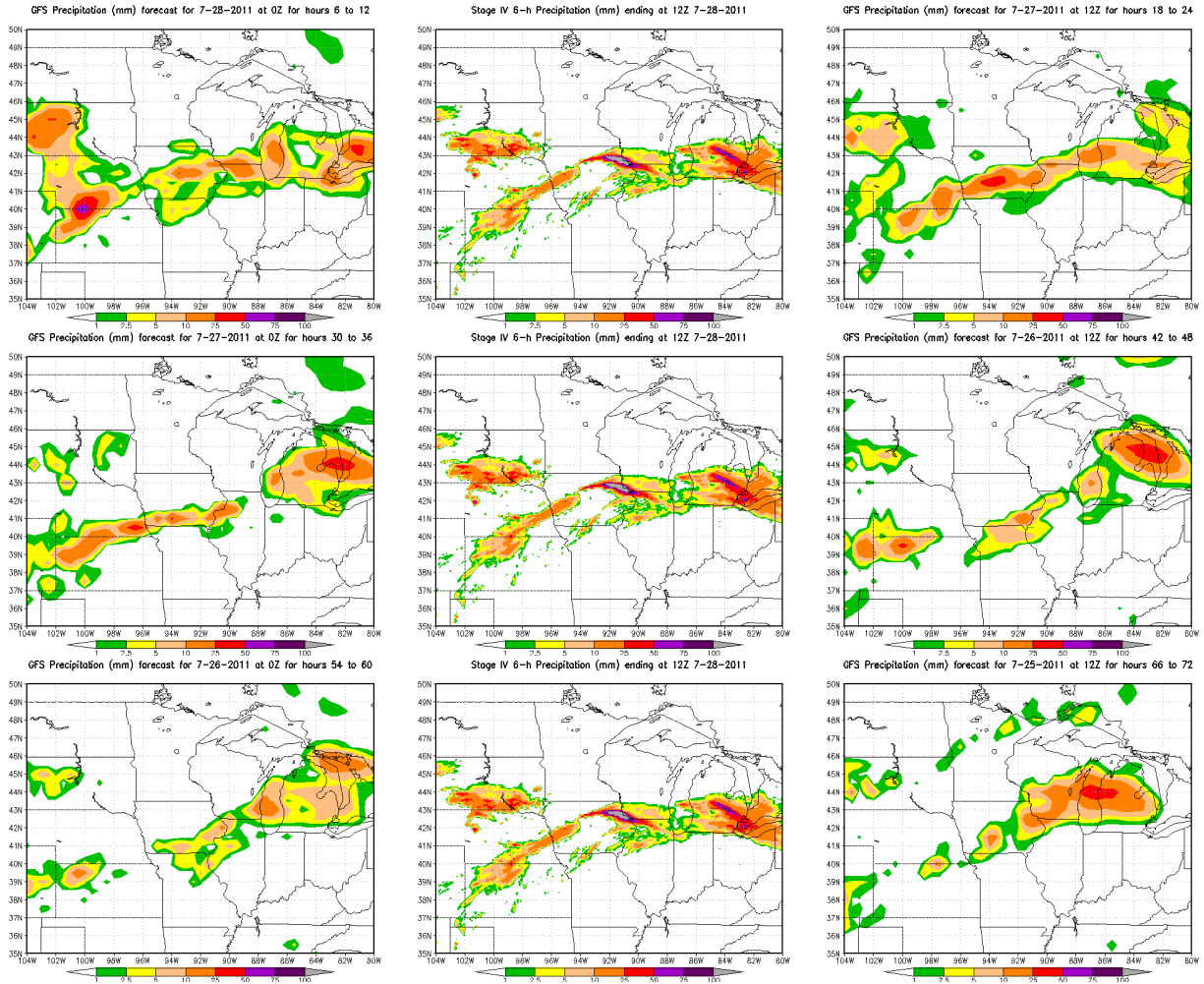
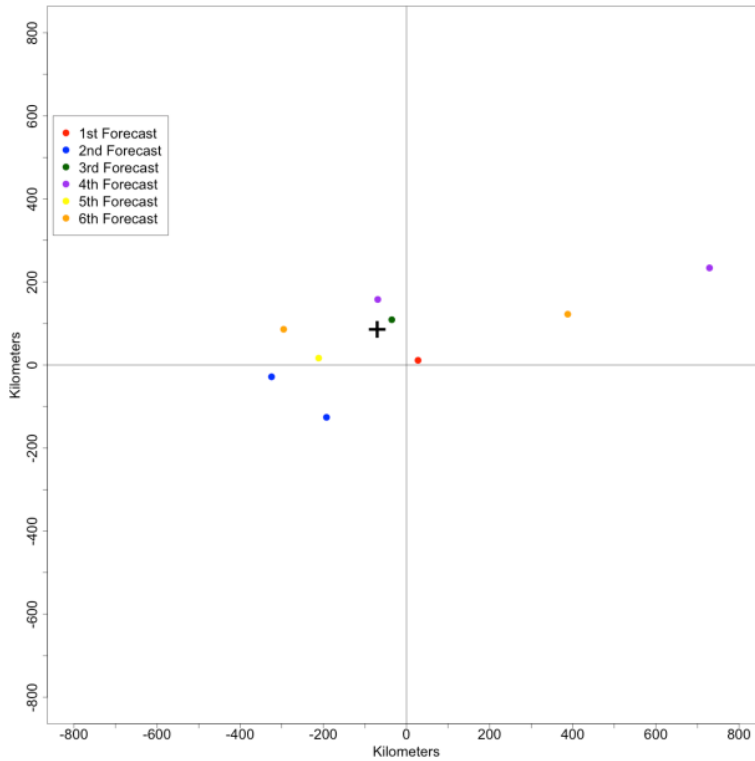


Figure 5.4.5: The GFS model's 6 forecasts and corresponding Stage IV precipitation valid for 28 July 2011 0000 to 0600 UTC.

GFS 6-Hour Forecast Errors for 7-28-2011 0Z-12Z



Charles Yost and Russ Schumacher - Colorado State University

Figure 5.4.6: GFS model's MCS forecast locations relative to the observed MCS locations using the MODE tool for the two 6 hour periods on 28 July 2011 from 0000 to 1200 UTC.

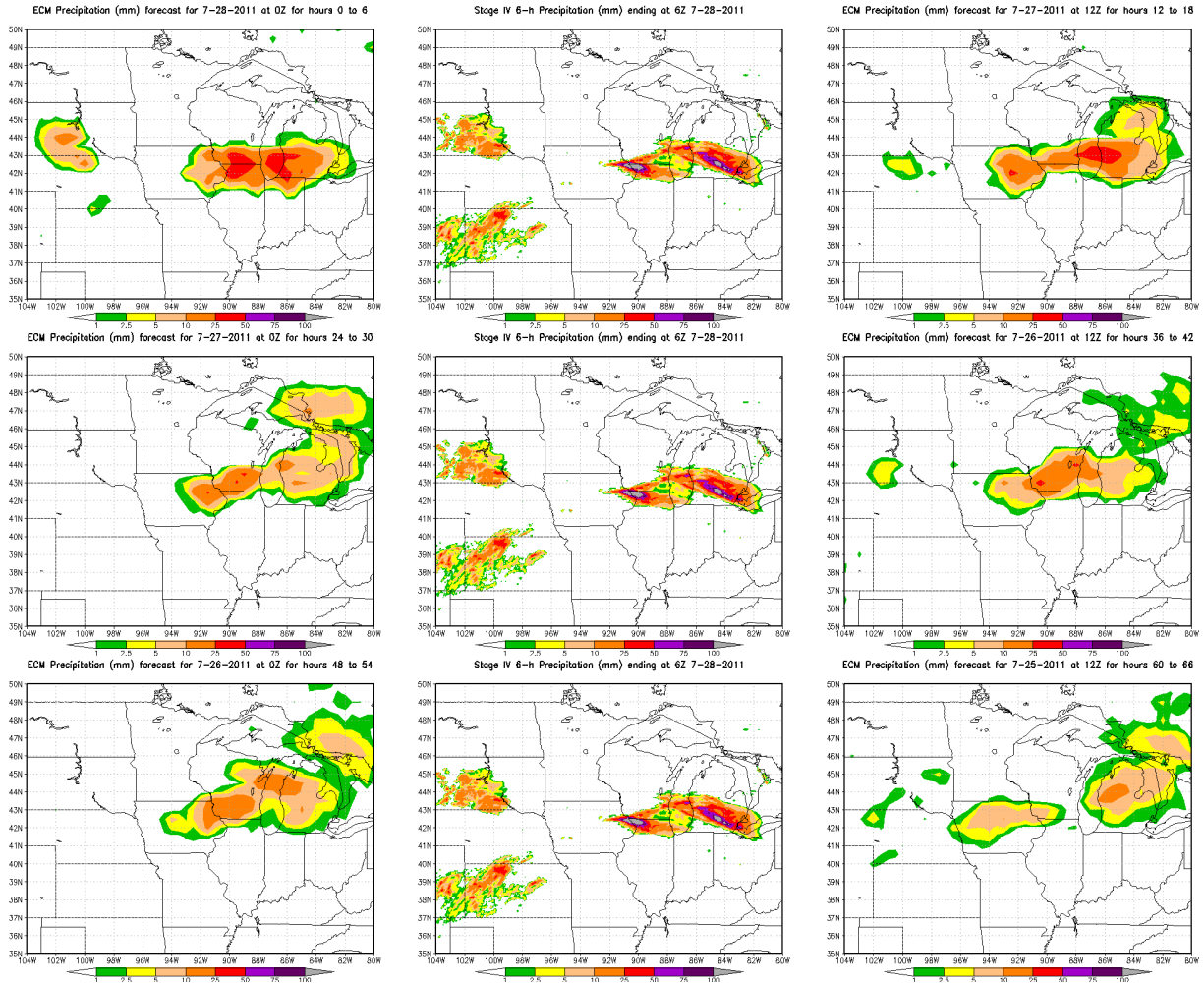


Figure 5.4.7: The ECM model's 6 forecasts and corresponding Stage IV precipitation valid for 28 July 2011 0000 to 0600 UTC.

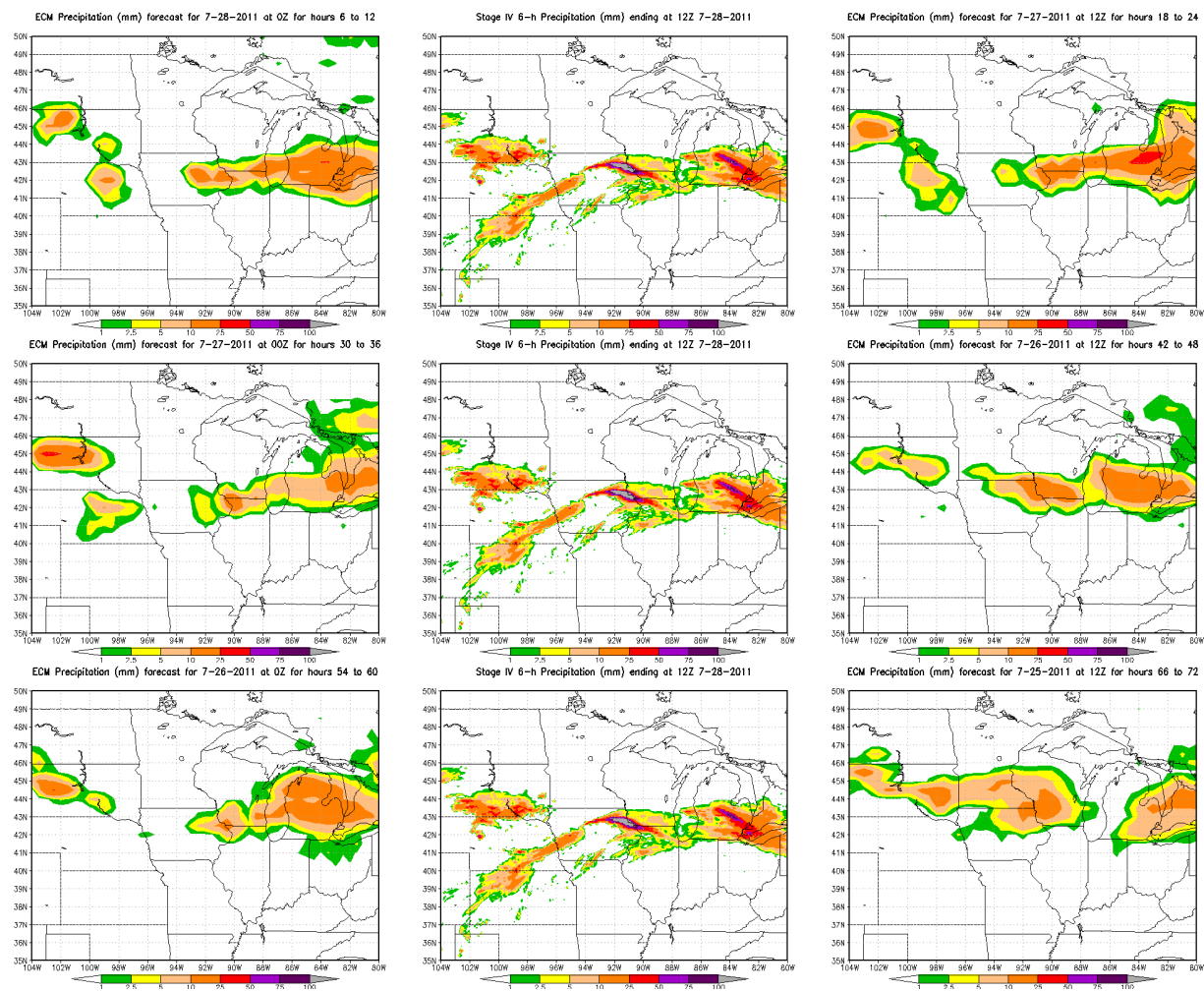
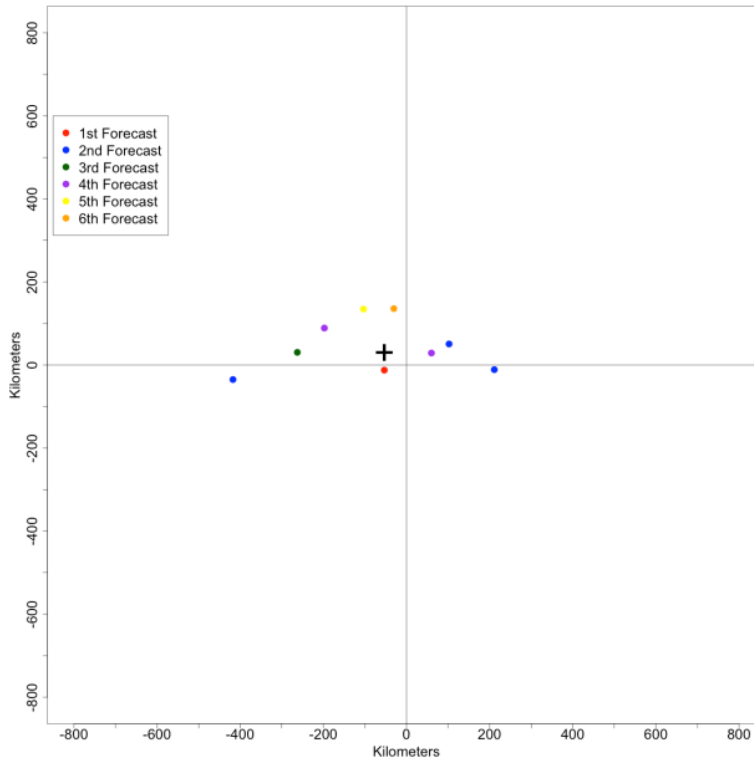


Figure 5.4.8: The ECM model's 6 forecasts and corresponding Stage IV precipitation valid for 28 July 2011 0000 to 0600 UTC.

ECM 6-Hour Forecast Errors for 7-28-2011 0Z-12Z



Charles Yost and Russ Schumacher - Colorado State University

Figure 5.4.9: ECM model’s MCS forecast locations relative to the observed MCS locations using the MODE tool for the two 6 hour periods on 28 July 2011 from 0 to 12 UTC.

5.5 Frontal Placement

The location of the boundary responsible for initiating convection in the forecasts is one hypothesized reason for the northern bias and will be investigated here. Since by definition, some boundary or baroclinic zone is needed to serve as the primary lifting mechanism for new convective cells forming upstream, the location of this front will naturally be pivotal. For example, Schumacher et al. (2011) noted that the displacement of the baroclinic zone was likely the cause of a northward displacement of an MCS in the case they studied, whereas Wang et al. (2010) found that the NAM is generally accurate in its predictions of frontal position.

Renard and Clarke (1965) developed a formula to objectively analyze fronts. The calculated the directional derivative of the gradient of potential temperature along its gradient, as noted with

$$GG\theta = - \frac{\nabla |\nabla\theta| \cdot \nabla\theta}{|\nabla\theta|} \equiv - \nabla |\nabla\theta| \cdot n_\theta$$

This objective analysis was applied to all forecasts and verified against the NAM model's analysis for the corresponding valid time.

Two NAM model runs were chosen to further investigate this northern bias by choosing two runs that produced a northern forecast and a neutral forecast. The NAM model's 0000 UTC run on 27 July 2011 (3rd forecast) had an exclusively northern forecast and the 0000 UTC run on 28 July 2011 (1st forecast) had an no north/south displacement. The NAM analysis was used as the "observations" for this investigation. Figure 5.5.1 shows the objectively analyzed NAM analysis at the surface (1000 hPa) for 0600 UTC, which compares favorably to the HPC manual analysis (Fig. 5.2.8), suggesting that the NAM analysis provides a reasonable gridded representation of the "truth" in this case.

Delving into the northern forecast, Figure 5.5.2 shows the objectively analyzed NAM analysis front along with the 30-hour forecast from the 0000 UTC 27 July 2011 run. The six hour increment after the valid time was plotted to show how the current frontal solution (observed and forecasted) affected precipitation. The NAM model's forecasted front is located too far to the north, with the western half of the stationary front over Kansas, Nebraska, and Iowa shifted to the northwest. The section of the stationary front closest to the observed precipitation maximum

NAM Analysis of Frontal Location
7-28-2011 at 6Z

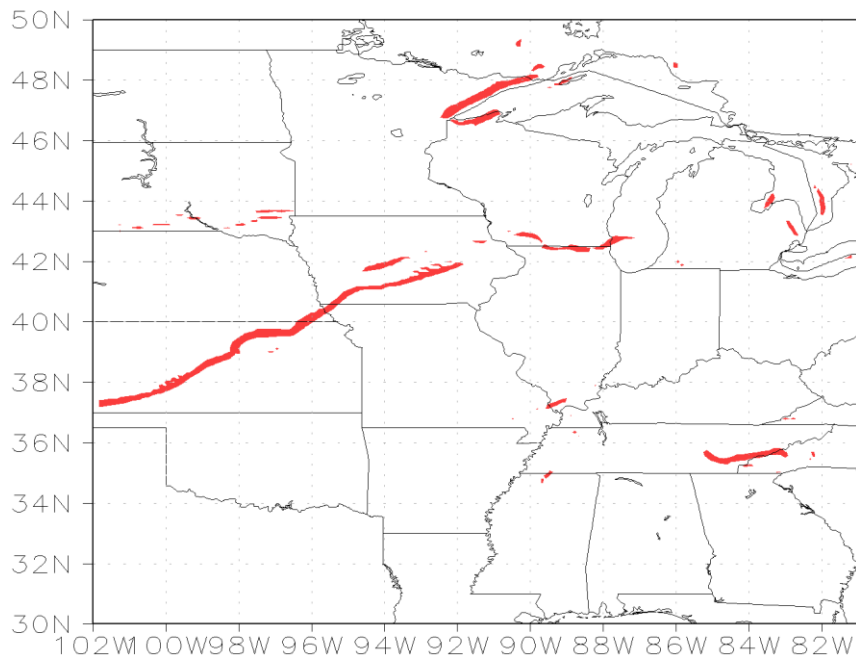


Figure 5.5.1 The objectively analyzed NAM analysis frontal locations at the surface.

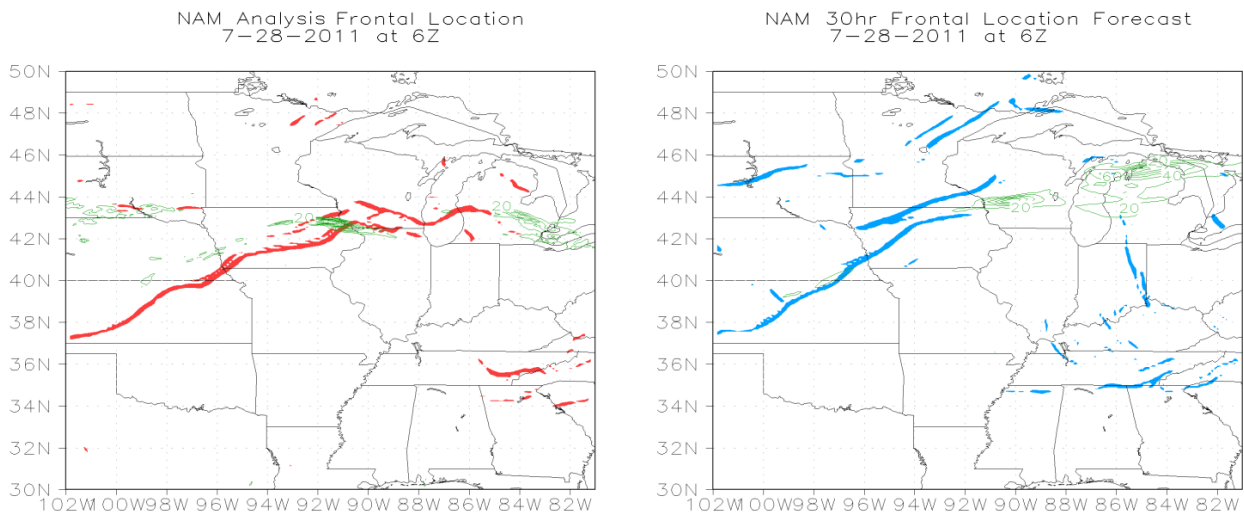


Figure 5.5.2 (a) The objectively analyzed NAM analysis frontal location at 825 hPa with observed precipitation and (b) the NAM model's 30 hour frontal location forecast with forecasted precipitation (green contours every 20 mm)

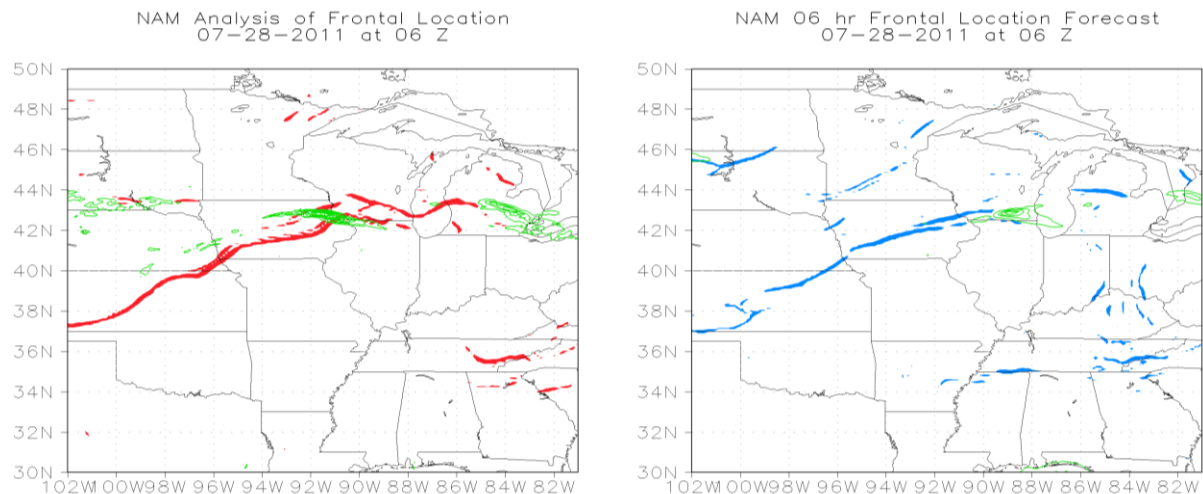


Figure 5.5.3 (a) The objectively analyzed NAM analysis frontal location at 825 hPa with observed precipitation and (b) the NAM model's 6 hour frontal location forecast with forecasted precipitation (both with 20 mm precipitation contours).

is shifted directly north. The forecasted precipitation over the next six hours is then subsequently forecasted directly north.

Looking at the neutral case in Figure 5.5.3, the stationary front forecasted in this model run has a placement identical to the analysis and HPC frontal analysis. The portion of the forecasted front where the observed precipitation maximum occurs is directly over the tri-state area. Although the precipitation is located slightly to the east at this time, the previous 6-hour period was extremely accurate and the focus of the difference between the two model runs should be on the y displacement error.

If a misplacement in the frontal location did exist, the difference in potential temperature fields between the analysis and forecast should show this. Looking at the northern case, Figure 5.5.4 is the potential temperature difference (shaded) and the wind difference (wind barbs) between the forecast and the analysis (forecast-analysis), with the 36 hour precipitation forecast contoured in green. A large maximum of potential temperature is located just to the west of the observed MCS, indicating that the front was forecasted to the north of this region, leaving

observed lower potential temperature values over the maximum to be subtracted from the higher potential temperature values in the forecasted field. Also, a large wind shift and wind speed difference occurs in this region, indicating the misplacement of the front in the area with the wind barbs pointing north to the forecasted precipitation. Since the observed winds in this area were close to zero, this wind difference is all from the forecasted winds. Figure 5.5.5 shows the identical fields except for the neutral case, with the corresponding 6-hour forecasted precipitation. The neutral case had at most a 4 K difference in the area closest to the observed maximum precipitation. This lack of a potential temperature and wind difference shows that the front was resolved in the correct location for the neutral case.

Looking at the difference in the magnitude between the LLJ in the 30 hour forecast and the analysis in Figure 5.5.2 shows a strong difference ahead of the forecasted front. This large magnitude difference is due to these forecasted winds not being present in the NAM analysis with the actual front located farther south. One other thing to note is the absence of a stronger LLJ over the whole Mississippi Valley in the 30 hour forecast. One possible explanation for the northern forecasted front is a stronger LLJ that was advecting warm air, and as a result, the front itself, farther north. This LLJ magnitude difference just shows the extending of the LLJ tongue until it reaches the forecasted front in northern Iowa. The neutral case is devoid of any non-trivial low-level jet magnitude difference around the rain event area.

Theta Forecast Difference 7-28-2011 at 6Z 30hr at 925hPa

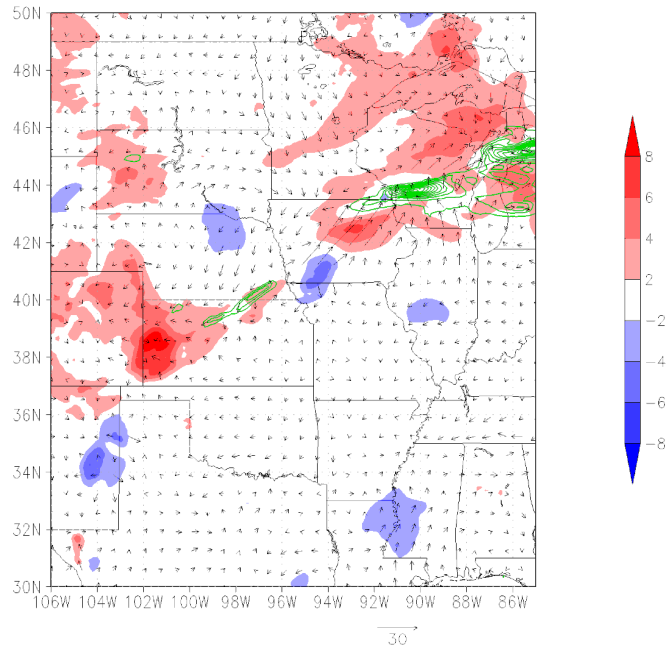


Figure 5.5.4 The potential temperature (Kelvin) and wind difference (knots) between the analysis and 30 hour forecast (forecast minus analysis) with the 30 hour precipitation forecast contoured in green every 10 mm for the northern case.

Theta Forecast Difference 07-28-2011 at 06Z 08hr at 925hPa

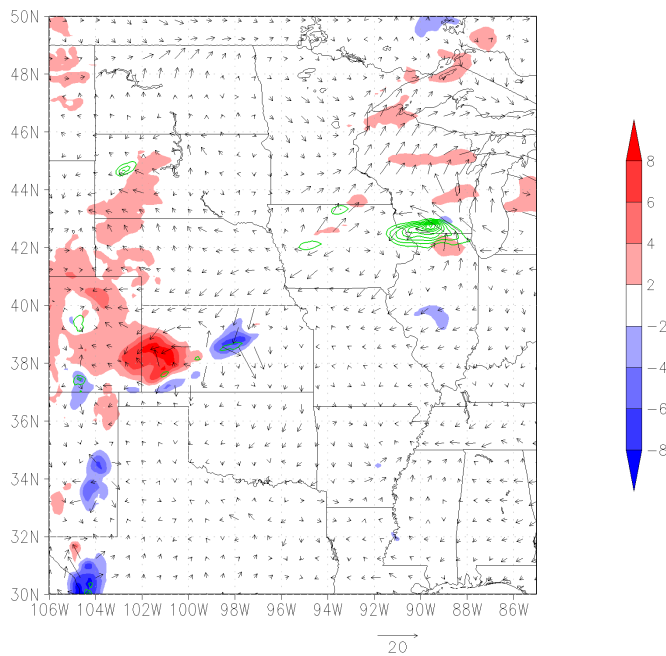


Figure 5.5.5 The potential temperature (Kelvin) and wind difference (knots) between the analysis and 30 hour forecast (forecast minus analysis) with the 30 hour precipitation forecast contoured in green every 10 mm for the neutral case.

LLJ (850mb) Magnitude Forecast Difference 7-28-2011 at 6Z 30hr

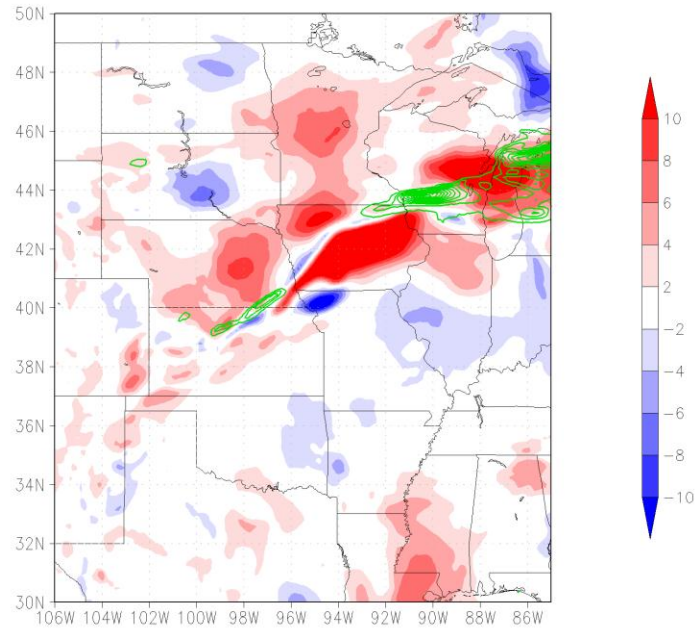


Figure 5.5.6 The magnitude of the wind difference (knots) between the analysis and 30 hour forecast (forecast minus analysis) with the 30 hour precipitation forecast contoured in green every 10 mm.

LLJ (850mb) Magnitude Forecast Difference 07-28-2011 at 06Z 06hr

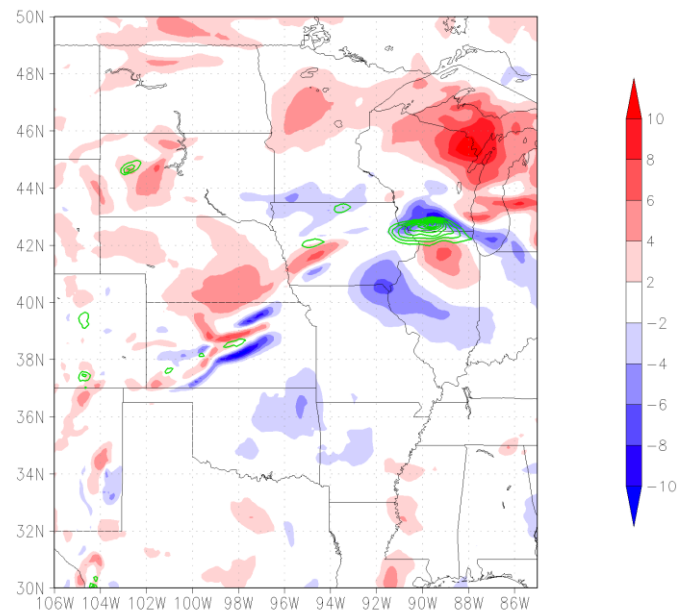


Figure 5.5.7 The magnitude of the wind difference (knots) between the analysis and 6 hour forecast (forecast minus analysis) with the 6 hour precipitation forecast contoured in green every 10 mm.

CHAPTER 6

CONCLUSIONS AND FUTURE WORK

6.1 Conclusions

This study verifies the use of the MODE tool to investigate forecast displacement biases of MCSs. Manual analysis confirmed what the MODE tool objectively found, validating the use of it for future locational verification applications.

The GFS model performed the worst with 74% of the cases forecasted too far to the north and an average displacement error of 297 km. The GFS model also hinted at an eastern bias, which can be extrapolated to be a temporal bias with 65% of the cases to the east. The average displacement error for the first three and last three forecasts were 239 km and 365 km, respectively, with the higher displacement errors correlating to more missed forecasts at 33% and 42%, respectively. A general increase in the mean forecast displacement errors correlates to an increase in forecast number. The GFS model went through a model upgrade on 27 July 2010 with the upgrade possibly causing a shift westward.

The NAM model had the second highest displacement bias with 68% of the total forecasts predicted too far to the north, or too far into the cool sector of the frontal boundary, with a median y displacement of 63 km. The earlier lead time forecasts actually performed worst with 73% located to the north, while missing fewer forecasts compared to the later at 30% and 46% of the cases, respectively. Although the bias was stronger, the earlier lead times performed better with respect to average distance from the observed (231 km compared to 273 km).

The ECM model performed the best out of all the models with parameterized convection with respect to a northern bias and mean displacement errors for all forecasts (64% and 182 km) and the first three (61% and 253 km). The ECM model also missed the fewest

number of forecasted objects for all forecast times (29%). One model upgrade occurred through the course of the study period on 26 January 2010, with no real impact on the northern bias, but possibly on the east/west spatial extent.

The convection-allowing NSSL-WRF model had a slight southern bias associated with its forecasted MCS locations (52.8%). Due to data limitations, only the 2009 and 2010 warm seasons were evaluated, which yielded the lowest average displacement errors for the first two forecasts (158.5 km). In order to fairly evaluate how the NSSL model did compared to the operational models, the NSSL model subset of the operational models performed similar to the full set, except curiously for the NAM model subset. The NAM model's NSSL subset did not have a northern bias (52% north), which could possibly be tied to the NSSL model being initialized from the NAM model. However, this subset is small and the results are not statistically significant. Further work is need in this area.

Finally, a case study of the Dubuque, IA MCS, that set several rainfall records in Iowa, was analyzed to investigate the cause of this northern bias. The destructive MCS was a classic TL/AS MCS type that initiated on the cool side of a stationary front that originated from a previous day's MCS. The event was well forecasted by the operational models, with most forecasts neutral or near-neutral. Two NAM forecasts (one neutral and one northern) were evaluated and found that the location of the stationary front proved pivotal in the location of the eventual MCS. In comparison with the NAM analysis, the forecast potential temperature and wind field have areas of higher potential temperature and stronger winds located just to the south of the forecasted precipitation maximum, which is indicative of an incorrect frontal placement. The neutral forecast did not have this difference in either field.

6.2 Future Work

Suggestions for future work include expanding the number of years of the primary case study to include the 2012 warm season, and including the high resolution NSSL-WRF model in the bias study and the Dubuque, IA MCS case study. Additional work needs to be done to investigate regional biases of MCS locations and the impact on their forecasts. Exact causes of the northern forecast of the stationary front in the Dubuque, IA MCS still need to be investigated with an emphasis on soil moisture's impact on mesoscale circulations that could impact the front's location. A neutral forecast for the event had the previous day's MCS further south (in the correct location) compared to the northern forecast. This discrepancy in the previous day's MCS forecast could manifest itself by impacting the low-level circulation from the soil moisture or the location of two different outflow boundaries.

REFERENCES

- Brier GW. 1950. Verification of forecasts expressed in terms of probability. *Monthly Weather Review*, **78**: 1–3.
- Brooks, H. E., M. S. Tracton, D. J. Stensrud, G. J. DiMego, and Z. Toth, 1995: Short-range ensemble forecasting: Report from a workshop, 25–27 July 1994. *Bull. Amer. Meteor. Soc.*, **76**, 1617–1624.
- Casati, B., and Coauthors, 2008: Forecast verification: Current status and future directions. *Meteor. Appl.*, **15**, 3–18.
- Chappell, C. F., 1986: Quasi-stationary convective events. *Mesoscale Meteorology and Forecasting*, P. S. Ray, Ed. *Amer. Meteor. Soc.*, 289–309.
- Davis, C., B. Brown, and R. Bullock, 2006a: Object-based verification of precipitation forecasts. Part I: Methodology and application to mesoscale rain areas. *Mon. Wea. Rev.*, **134**, 1772–1784.
- , ———, and ———, 2006b: Object-based verification of precipitation forecasts. Part II: Application to convective rain systems. *Mon. Wea. Rev.*, **134**, 1785–1795.
- Davenport Area Forecast Discussion. [Available online at <http://mesonet.agron.iastate.edu/wx/afos/p.php?dir=prev&pil=AFDDVN&e=201107271829>]
- Doswell, C. A., H. E. Brooks, and R. A. Maddox, 1996: Flash flood forecasting: An ingredients-based methodology. *Wea. Forecasting*, **11**, 560–581.
- , R. Davies-Jones, and D. L. Keller, 1990: On summary measures of skill in rare event forecasting based on contingency tables. *Wea. Forecasting*, **5**, 576–585.

ECMWF Horizontal Resolution Increase, 2012 [Available online at

http://www.ecmwf.int/products/changes/horizontal_resolution_2009/]

Fritsch, J. M., R. J. Kane, and C. R. Chelius, 1986: The contribution of mesoscale convective weather systems to the warm-season precipitation in the United States. *J. Appl. Meteor.*, **25**, 1333-1345.

Fulton, R. A., J. P. Breidenbach, D.-J. Seo, D. A. Miller, and T. O'Bannon, 1998: The WSR-88D rainfall algorithm. *Wea. Forecasting*, **13**, 377–395

Gilbert GK. 1884. Finley's tornado predictions. *American Meteorological Journal*, **1**: 166–172.

Historic Heavy Rain and Flash Flooding in Dubuque and Jo Daviess Counties 07/27-07/28/2011

[Available online at http://www.crh.noaa.gov/dvn/?n=event_072711_dubuqueflashflood]

Junker, N. W., and R. S. Schneider, 1997: Two case studies of quasi-stationary convection during the 1993 Great Midwest Flood. *Natl. Wea. Dig.*, **21**, 5-17.

_____, R. S. Schneider, and S. L. Fauver, 1999: A study of heavy rainfall events during the Great Midwest Flood of 1993. *Wea. Forecasting*, **14**, 701-712.

Lin, Y., and K. E. Mitchell, 2005: The NCEP stage II/IV hourly precipitation analyses: Development and applications. Preprints, 19th Conf. on Hydrology, San Diego, CA, Amer. Meteor. Soc., CD-ROM, 1.2.

Maddox, R. A., C. F. Chappell, and L. R. Hoxit, 1979: Synoptic and meso- α scale aspects of flash flood events. *Bull. Amer. Meteor. Soc.*, **60**, 115-123.

Marsh, P. T., J. S. Kain, A. J. Clark, V. Lakshamanan, N. M. Hitchens, and J. Hardy, 2012: A method for calibrating deterministic forecasts of rare events. *Wea. Forecasting*, in press

- Mesoscale Branch Web Page Reference List: 4. On-Line Documentation Of Mesoscale Branch Model Changes, 2012. [Available online at <http://www.emc.ncep.noaa.gov/NAM/clog.php>]
- Mesinger, F., 1996: Improvements in quantitative precipitation forecasts with the Eta regional model at the National Centers for Environmental Prediction: The 48-km upgrade. *Bull. Amer. Meteor. Soc.*, **77**, 2637–2650.
- _____, 2008: Bias adjusted precipitation threat scores. *Adv. Geosci.*, **16**, 137–142.
- Novak, D. R., D. Bright, and M. Brennan, 2008: Operational forecaster uncertainty needs and future roles. *Wea. Forecasting*, **23**, 1069–1084.
- Parker, M. D., and R. H. Johnson, 2000: Organizational modes of midlatitude Mesoscale convective systems. *Mon. Wea. Rev.*, **128**, 3413-3436.
- Previous GFS Implementations, 2012 [Available online at <http://www.emc.ncep.noaa.gov/GFS/impl.php>]
- Rogers, E., T. L. Black, D. G. Deaven, G. J. DiMego, Q. Zhao, M. Baldwin, N. W. Junker, and Y. Lin, 1996: Changes to the operational “early” Eta analysis/forecast system at the National Centers for Environmental Prediction. *Wea. Forecasting*, **11**, 391–413.
- Renard, R. J., and L. C. Clarke, 1965: Experiments in numerical objective frontal analysis. *Mon. Wea. Rev.*, **93**, 547–556.
- Schaefer JT. 1990. The critical success index as an indicator of warning skill. *Weather and Forecasting*, **5**: 570–575.
- Schumacher, R. S., and R. H. Johnson, 2005: Organization and environmental properties of extreme-rain-producing mesoscale convective systems. *Mon. Wea. Rev.*, **133**, 961–976.
- _____, and _____, 2006: Characteristics of U.S. extreme rain events during 1999-2003. *Wea.*

Forecasting, **21**, 69-85.

_____, and _____, 2009: Quasi-stationary, extreme-rain-producing convective systems associated with midlevel cyclonic circulations. *Wea. Forecasting*, **24**, 555-574.

Wang, S.-Y., and A. J. Clark, 2010: NAM model forecasts of warm season quasi-stationary frontal environments in the central U.S. Accepted for publication in *Wea. Forecasting*.

Wilks, D. S., 1995: *Statistical Methods in the Atmospheric Sciences: An Introduction*. Academic Press, 467 pp.